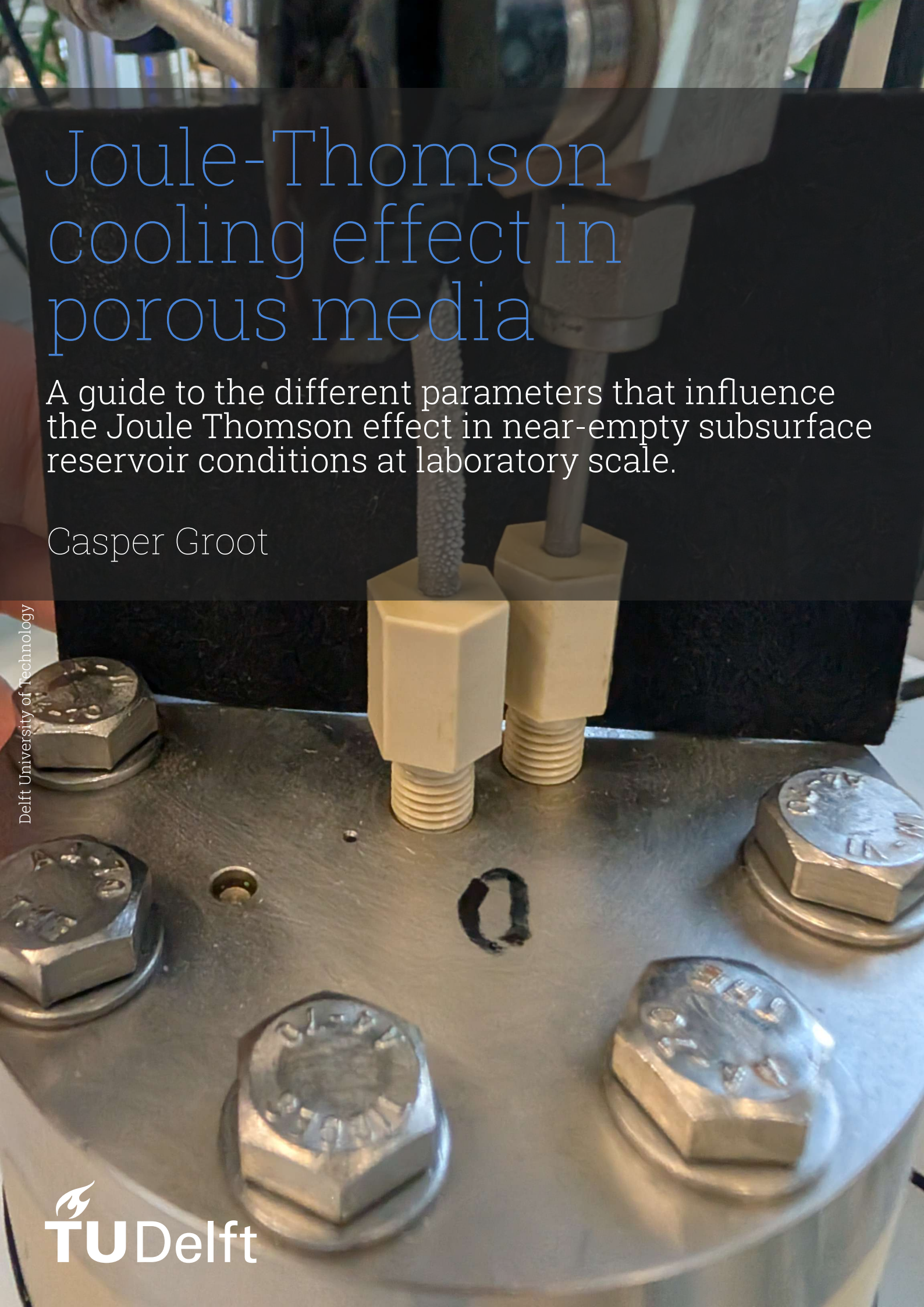

Joule-Thomson cooling effect in porous media

A guide to the different parameters that influence the Joule Thomson effect in near-empty subsurface reservoir conditions at laboratory scale.

Casper Groot

Delft University of Technology

TU Delft

Joule-Thomson cooling effect in porous media

A guide to the different parameters that influence the Joule Thomson effect in near-empty subsurface reservoir conditions at laboratory scale.

by

Casper Groot

Instructor:	Dr. D.V. (Denis) Voskov
Daily supervisor:	Dr. S.A. (Sian) Jones
Lab Technician:	M. Slob
Project Duration:	Feb, 2025 - Jun, 2025
Faculty:	Faculty of Applied Earth Sciences, Delft

TU Delft

Acknowledgements

This thesis is the result of a challenging and rewarding research project on Joule-Thomson cooling in porous media, motivated by the scientific and practical relevance for geological CO_2 storage, including projects such as Porthos. Throughout this process, I have benefited from both technical guidance and collaborative support.

I would like to thank my supervisor, Dr. D.V. (Denis) Voskov, for his consistent scientific direction and feedback. I am also grateful to my daily supervisor, Dr. S.A. (Sian) Jones for her detailed input, discussions and encouragement. The practical aspects of this research would not have been possible without the expertise of Lab Technician Michiel Slob, whose involvement in the design and operation of the experimental setups was essential.

Discussions with members of the reservoir engineering group contributed to the interpretation of my results and the overall research design. I also thank the lab staff for their willingness to assist with both technical and practical challenges in the laboratory.

On a personal note, I appreciate the support of my family and friends, who provided motivation and perspective during the more demanding periods of this project.

Casper Groot
Delft, July 2025

Abstract

This thesis presents a systematic experimental and numerical investigation into the thermal dynamics of CO_2 injection into porous media, focusing on the Joule-Thomson (JT) cooling effect under conditions relevant to Carbon Capture and Storage (CCS) in depleted reservoirs. The purpose of the study was to deconvolve the mechanisms that govern cooling and to validate numerical models against laboratory data.

Experiments were conducted on two contrasting sandstones: a low-permeability (0.37 mD) Kentucky core, analogous to tight reservoirs, and a high-permeability (1-2 D) Bentheimer core. The cores were instrumented with distributed temperature and pressure sensors to capture transient thermal fronts during CO_2 injection. In the low-permeability Kentucky core, the JT cooling was driven by the significant pressure gradient across the porous medium itself. In contrast, the high-permeability Bentheimer core required an artificial inlet pressure drop to initiate cooling; subsequent thermal transport was found to be dominated by the high cooling power of phase change (evaporation) rather than continuous isenthalpic expansion.

Across both types of rock, a systematic phase boundary offset was observed, with phase transitions occurring at pressures 2–4 bar lower (or 2-3 K higher) than predicted by bulk CO_2 thermodynamics. Rigorous analysis demonstrates that this significant offset cannot be explained by classical confinement theories such as the Gibbs-Thomson or Kelvin effects, pointing to a more complex interplay of non-equilibrium thermodynamics, capillary phenomena, and rock-fluid interactions.

Numerical simulations using the Delft Advanced Research Terra Simulator (DARTS) successfully reproduced general cooling trends but highlighted critical model requirements. High-resolution Equation of State (EOS) tables (>2000 points) were essential for precision, while the absence of a correct CO_2 gas-liquid relative permeability model limited the ability to capture the pressure build-up observed experimentally due to accumulation of the liquid phase.

The findings demonstrate that, while JT cooling is a measurable and critical process, its prediction requires models that incorporate pore-scale physics beyond bulk thermodynamics. The results provide a validated data set and a refined understanding of the coupled thermal-hydraulic processes that govern near-wellbore cooling during CCS operations.

Contents

List of Figures

List of Tables

Nomenclature

Abbreviations

Abbreviation	Definition
AES	Applied Earth Sciences
BPR	Back Pressure Regulator
BPC	Back Pressure Cartridge
CCS	Carbon Capture and Storage
CT	Computed Tomography
DARTS	Delft Advanced Research Terra Simulator
EOS	Equation of State
FESG	Fully Equivalent Subgrid Method
FKR	Fluorine Kautschuk Material
IEA	International Energy Agency
IPCC	Intergovernmental Panel on Climate Change
JT	Joule–Thomson
LBM	Lattice Boltzmann Method
MFC	Mass Flow Controller
PT	Pressure–Temperature
PVT	Pressure–Volume–Temperature
TU Delft	Delft University of Technology

Symbols

Symbol	Definition	Unit
A	Cross-sectional area	[m^2]
c_f	Heat capacity of fluid	[J/kg·K]
c_r	Heat capacity of rock matrix	[J/kg·K]
d	Diameter of core/sample	[m]
h	Enthalpy	[J/kg]
k	Permeability	[m^2] or [mD]
L	Length of core/sample	[m]
P	Pressure	[bar]
q_h	Volumetric heat source/sink	[W/m^3]
T	Temperature	[K]
t	Time	[s]
V	Volume or velocity (context-dependent)	[m^3] or [m/s]
Δ	Difference operator (e.g., ΔT = temperature difference)	[–]
$\dot{m}$	Mass flow rate	[kg/s]
∇	Gradient operator	[–]
λ_{eff}	Effective thermal conductivity	[W/m·K]
ϕ	Porosity	[–]
ρ_f	Density of fluid	[kg/m^3]
ρ_r	Density of rock matrix	[kg/m^3]
μ	Dynamic viscosity	[Pa·s]

1

Introduction

Global climate change is one of the most pressing challenges of the 21st century, driven primarily by the increase in greenhouse gas emissions, particularly carbon dioxide (CO_2). Carbon Capture and Storage (CCS) has emerged as a fast mitigation strategy, involving the capture of CO_2 from industrial sources and its subsequent injection into deep geological formations such as depleted gas reservoirs or saline aquifers for long-term containment (Bachu, 2008; Benson & Cole, 2008).

In the Netherlands, the Porthos project exemplifies this strategy by aiming to inject captured CO_2 into depleted offshore gas fields in the North Sea. These reservoirs offer several operational advantages, including well-characterized geological structures, existing infrastructure, and proven seal integrity. However, to ensure the safety and efficiency of such systems, a detailed understanding of subsurface fluid flow and thermal behavior under low pressure, near-depleted conditions is essential.

A key operational challenge in this context is the Joule-Thomson (JT) cooling effect, a thermodynamic process in which real gases, such as CO_2, cool during isenthalpic expansion. When dense phase CO_2 is injected into a low-pressure reservoir, it can undergo rapid cooling, further exacerbated by exposure to cold subsea transport lines. This temperature drop may induce the formation of CO_2 hydrates in the presence of residual brine, potentially affecting injectivity and compromising long-term operational stability (Mathias et al., 2010). Hydrate formation can reduce or block the pore space, necessitating costly remediation or even halting injection operations.

The Joule–Thomson cooling phenomenon has been studied through theoretical and numerical modeling. Oldenburg (2006, 2007) simulated JT-induced temperature drops using the TOUGH2/EOS7C simulator, showing that high injection rates and low reservoir pressures can lead to temperature reductions exceeding 20 °C. These studies highlighted associated risks, including the formation of hydrates and thermally induced fracturing. Analytical models developed by Mathias et al. (2010) provided closed-form solutions for radial geometries, improving the understanding of cooling front evolution under quasi-steady conditions.

To mitigate such risks, several strategies have been proposed, including injection rate modulation, inlet temperature control, and the application of predictive thermal models (Chesnokov et al., 2024; Mathias et al., 2010). However, these approaches often introduce operational trade-offs, such as increased energy consumption or complexity, particularly in the presence of fluid impurities (Ziabakhsh-Ganji & Kooi, 2014). Therefore, a precise characterization of JT cooling under realistic near-wellbore conditions remains essential for a robust and risk-informed injection design.

More recently, Chesnokov et al. (2024) developed an exact analytical solution that incorporates transient heat exchange with the surrounding rock matrix. Zamani et al. (2024) applied the TOUGH2-ECO2M simulator to examine the sensitivity of JT cooling to operational parameters, highlighting nonlinear dependencies on bottom hole temperature and reservoir permeability. Tweed et al. (2024) proposed similarity solutions to model early-time JT cooling behavior in gas-filled, under-pressured reservoirs, offering a reduced-order modeling approach for transient conditions.

Despite these advances, the literature still lacks experimental studies that validate these models under controlled porous media conditions. Consequently, existing models may not accurately capture complex interactions between JT cooling, multiphase flow, capillary forces, and rock heterogeneity, particularly in low-permeability formations.

This study addresses this gap by establishing a robust experimental framework for investigating JT cooling in porous media at the core scale under reservoir-relevant conditions. The work is complemented by numerical modeling using the Delft Advanced Research Terra Simulator (DARTS). The experimental data set serves to validate existing numerical models and enables systematic exploration of key parameters such as injection rate, initial saturation, and rock permeability.

By generating reproducible laboratory data under tightly controlled conditions, this thesis provides a foundational reference for future studies. It also aims to decouple JT cooling from associated phase change effects and assess their implications for the design and operation of large-scale CCS systems.

1.1. Research Questions

The central research question is:

> **Can laboratory setups accurately predict and experimentally validate Joule-Thomson cooling behavior in porous media under near-wellbore conditions representative of depleted CO_2 reservoirs?**

To support this investigation, four sub-questions are formulated:

1. How can laboratory experiments be systematically designed to isolate and quantify Joule-Thomson cooling in porous sandstone under representative reservoir conditions?
2. What is the relative influence of flow rate, permeability, and pressure regulation on the onset and propagation of thermal fronts during CO_2 injection?
3. What physical processes govern the observed temperature-pressure offsets from the bulk CO_2 phase boundary, and how do they vary with core type?
4. To what extent can numerical simulations (DARTS) reproduce the experimental thermal and pressure response, and what limitations arise from Equation Of State (EOS) resoluton, grid resolution, and missing physical models?

These questions guide the structure of the experimental design, data analysis, and modeling workflows.

1.2. Report Structure

This thesis is organized into eight chapters, each contributing to a systematic exploration of Joule-Thomson (JT) cooling in porous media under conditions relevant to CO_2 storage in depleted reservoirs:

- **Chapter 2 – Theoretical Background:** Establishes the thermodynamic and physical framework for JT cooling. Topics include real-gas behavior, CO_2 phase transitions, and heat transfer mechanisms in porous geological systems. This chapter also reviews DARTS and highlights the experimental shortcomings of JT cooling research.
- **Chapter 3 – Methodology and Experimental setup:** Describes the experimental apparatus, including core holders, temperature and pressure sensors, fluid injection systems, and data acquisition protocols. This chapter details the systematic variation of parameters such as flow rate, injection pressure, and backpressure.
- **Chapter 4 – Results: Kentucky Sandstone:** Focuses on Kentucky Sandstone experiments with low permeability. Kentucky sandstone will establish a baseline for JT cooling while exploring different injection rates to assess the impact on a low-permeability system.
- **Chapter 5 – Results: Bentheimer Sandstone:** Presents the results of experiments carried out on high-permeability Bentheimer sandstone. Observations include cooling trends, thermodynamic calculations to evaluate JT cooling directly, and the establishment of the cooling power of phase changes. Additional experiments are performed to independently assess the pressure, injection rate, and injection pressure.
- **Chapter 6 – DARTS:** Interprets experimental findings in the context of numerical modeling performed with DARTS. This chapter explores model validation, sensitivity to input parameters, and limitations of the current simulation framework.
- **Chapter 7 – Comparative Analysis:** Integrates data from both core types to evaluate how permeability and heterogeneity affect the observed thermal responses. The thermal pressure offsets relative to the CO_2 phase boundaries are examined to understand the origin of the observed offset from the phase boundary.
- **Chapter 8 – Discussion:** Discusses insights derived from experimental and numerical investigations to address the arguments for the central research question and sub-questions. It evaluates the consistency between measured and simulated results, identifies key mechanisms driving deviations from idealized JT behavior, evaporative cooling, and discusses the implications of rock type, boundary conditions, and operational parameters.
- **Chapter 9 – Conclusions and Recommendations:** Summarizes the key findings of the study, critically evaluates the research questions, and outlines the directions for future work. Suggestions include refinement of measurement protocols, incorporation of hydrate kinetics, and extensions to heterogeneous or fractured media.

Collectively, these chapters form a cohesive investigation of JT cooling in porous media, combining theory, controlled experimentation, and numerical simulation to inform the design and risk assessment of CO_2 injection systems.

2

Literature Review and Background

This chapter reviews the scientific and technical foundations underpinning this research. It begins by contextualizing the study within global climate change mitigation efforts, highlighting the important role of Carbon Capture and Storage (CCS). Then it narrows down to geological storage in depleted gas reservoirs. The emphasis is placed on the dynamic thermal behavior of carbon dioxide (CO_2) during injection into depleted reservoirs, particularly in terms of temperature shifts, phase behavior, and energy balances in porous media.

2.1. Carbon Capture and Storage (CCS)

CCS is a climate mitigation strategy that aims to reduce greenhouse gas emissions by capturing CO_2 from large point sources, such as power plants or industrial processes, and permanently storing it in deep geological formations. The Intergovernmental Panel on Climate Change (IPCC) identifies CCS as a vital component in pathways that aim to limit global warming to well below 2,° C above pre-industrial levels, highlighting its role alongside the deployment of renewable energy, energy efficiency, and behavioral change (IPCC, 2022).

The CCS chain consists of three primary stages: *capture*, *transport*, and *storage*. A visual representation of this chain can be seen in Figure 2.1. In the capture phase, CO_2 is separated from the flue gas streams using technologies such as post-combustion absorption, pre-combustion gasification, or oxyfuel combustion. The captured CO_2 is then compressed into a supercritical or dense phase state and transported, typically by pipeline or ship, to a designated geological storage site. Suitable storage formations include deep saline aquifers, unmineable coal seams, and, most notably for this study, depleted oil and gas reservoirs (Bachu, 2008; Energy Agency, 2020).

Depleted hydrocarbon reservoirs offer multiple advantages for geological CO_2 storage. These formations have proven caprock integrity, known pressure and temperature conditions, and extensive subsurface data derived from decades of hydrocarbon production. In addition, existing infrastructure such as wells and facilities can be repurposed, reducing development costs and accelerating project timelines (Benson & Cole, 2008). For these reasons, they are considered a prime target for the near-term deployment of CCS at scale.

Nevertheless, CO_2 injection into such reservoirs introduces complex thermodynamic and geomechanical challenges that must be managed to ensure long-term injectivity and storage security. These challenges arise from the interplay of fluid flow, pressure differentials, and phase behavior in the subsurface. In particular, in depleted fields, where the formation pressure is low and the injection pressures and volumes are high, the thermodynamic behavior of CO_2 becomes especially significant, where rapid cooling can cause hydrate formation, (partially) blocking further injection with potentially permanent damage. Understanding these mechanisms is essential for optimizing injection strategies and ensuring the success of storage operations.

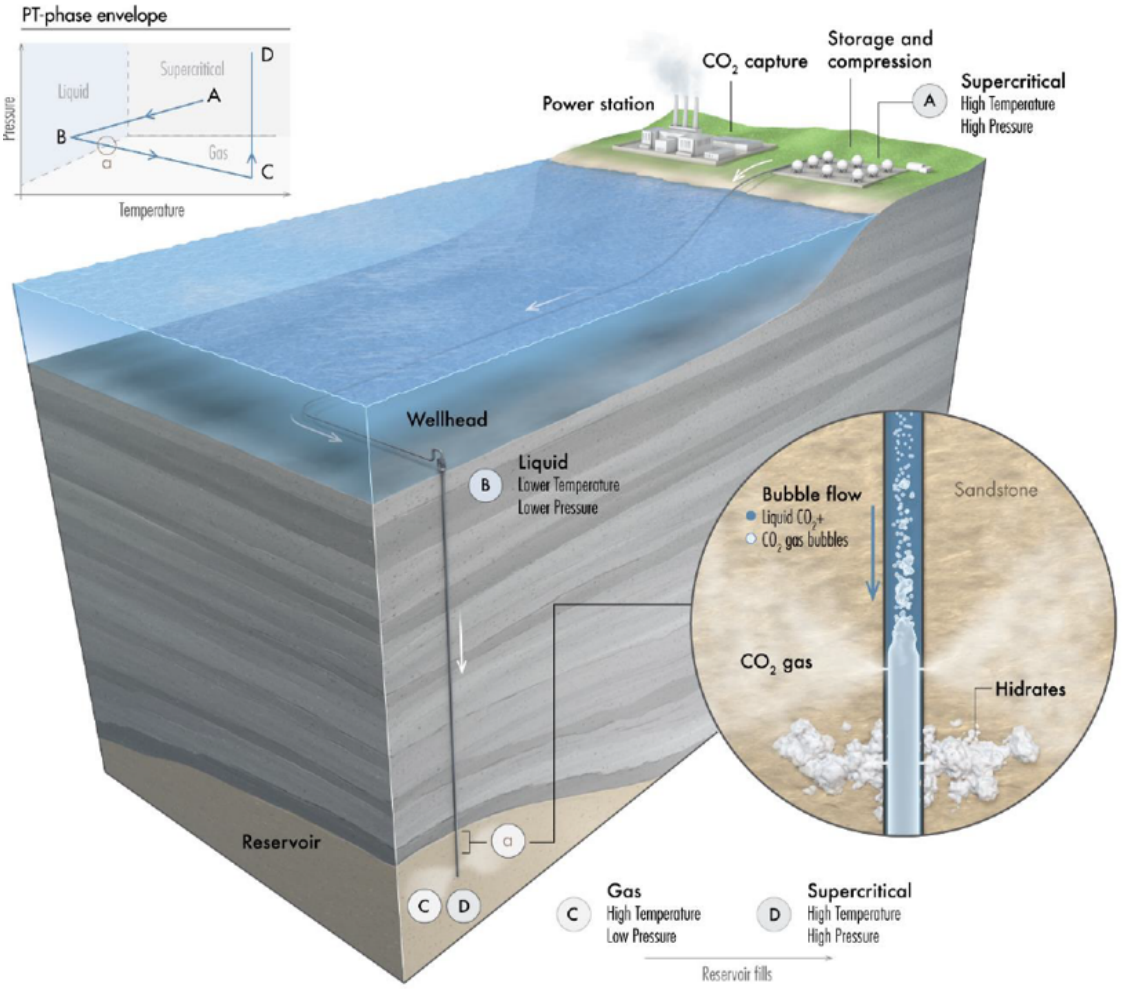

Figure 2.1: Schematic of the CO_2 injection process during offshore geological storage in a depleted gas reservoir. The figure illustrates the CCS chain from surface capture to subsurface storage, along with pressure-temperature phase transitions (top left), the progression from supercritical to liquid and gaseous CO_2 (A $\rightarrow$ D), and hydrate formation potential near the wellbore. Adapted from Hoteit et al. (2019).

2.2. Joule-Thomson Cooling and Dynamics of CO_2 Injection

2.2.1. Thermodynamic Basis of the Joule-Thomson Effect

The Joule-Thomson (JT) effect describes the temperature change of a real gas undergoing isenthalpic expansion, which is a drop in pressure at constant enthalpy. For CO_2, which is commonly injected into geological formations in a supercritical or dense phase, this expansion generally results in cooling. The magnitude of this effect is quantified by the JT coefficient, μ_{JT}:

$$\mu_{JT} = \left(\frac{\partial T}{\partial P}\right)_H, \tag{2.1}$$

Where T is temperature, P is pressure, and H is enthalpy. Under typical subsurface conditions, μ_{JT} for CO_2 is positive, which means that pressure reductions lead to temperature decreases.

The cooling observed during CO_2 injection arises from the non-ideal behavior of real gases. Unlike ideal gases, real gases experience intermolecular forces that cause enthalpy to vary with pressure. This dependence introduces temperature changes during isenthalpic expansion. The JT coefficient can be expressed using thermodynamic properties as:

$$\left(\frac{\partial T}{\partial P}\right)_H = \frac{1}{C_P}\left[T\left(\frac{\partial V}{\partial T}\right)_P - V\right]. \tag{2.2}$$

Here, C_P is the heat capacity at constant pressure, V is the molar volume, and T is the temperature. Rewrite this expression using the thermal expansion coefficient α, defined as:

$$\alpha = \frac{1}{V}\left(\frac{\partial V}{\partial T}\right)_P, \tag{2.3}$$

Leads to:

$$\mu_{JT} = \frac{V}{C_P}(\alpha T - 1). \tag{2.4}$$

This formulation highlights that cooling ($\mu_{JT} > 0$) occurs when $\alpha T > 1$, which is generally the case for CO_2 under reservoir conditions. Therefore, an accurate estimation of α and C_P is essential to quantify the temperature changes during injection.

2.2.2. Experimental and Modelling Insights into JT Cooling

Numerous studies have evaluated how operational parameters influence JT-induced cooling during CO_2 injection (Pruess, 2005). Core flooding experiments indicate that the sharpest temperature gradients develop near the wellbore, where the pressure drop is most severe (Maloney & Briceno, 2008). Mathias et al. (2010) observed cooling magnitudes of up to 30° C in analogues of depleted gas reservoirs. This is supported by Wapperom, dos Santos, and Voskov (2024), who linked increased pressure differentials and lower injection temperatures with more intense cooling effects.

Distributed temperature sensing (DTS) data from both laboratory and field setups show sharp temperature declines downstream of the injection point, consistent with the predicted JT thermal front. Flow rate is a key control: Higher injection rates drive deeper cooling into the formation as a result of stronger advective transport, whereas slower rates localize the cooling and allow for more thermal diffusion.

Reservoir properties such as permeability, pressure, and thickness also modulate the JT response. In lower pressure systems, CO_2 undergoes a more pronounced expansion, enhancing the cooling effect. The dynamic nature of the JT coefficient, which varies with pressure, temperature, and gas composition, further complicates the predictions. These dependencies emphasize the need for real-time monitoring and high-resolution thermophysical modeling (Tweed et al., 2024).

A representative example of JT cooling is shown in Figure 2.2, adapted from the work of (Maloney & Briceno, 2008). The figure demonstrates how pressure gradients and temperature changes evolve with time and distance along the core. The lower graph clearly illustrates the transient temperature drops caused by Joule-Thomson cooling, especially at shorter distances from the injection point, validating the existence and magnitude of thermal gradients predicted by theory.

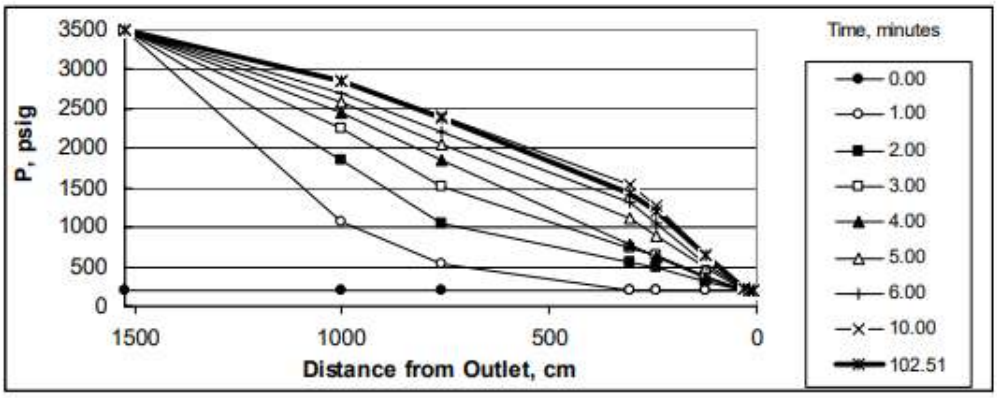

Figure 4. Pressure profiles during a **Scenario A** test.

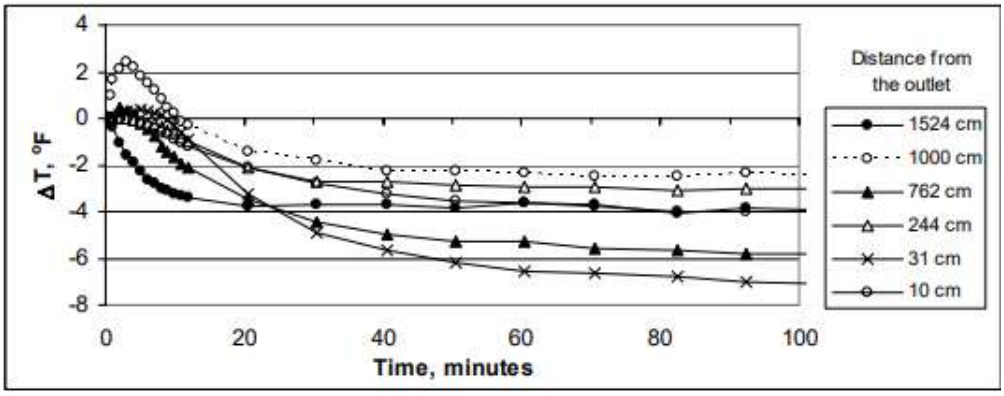

Figure 2.2: Experimental evidence of Joule-Thomson cooling in porous media. Top: Pressure profiles along the core during a Scenario A CO_2 injection test. Bottom: Temperature change over time at various distances from the outlet, showing the evolution of thermal gradients caused by isenthalpic expansion. Adapted from (Maloney & Briceno, 2008).

2.2.3. Thermal Front Propagation and Reservoir-Scale Effects

Simulation studies using TOUGH2, ECO2M, and DARTS show that the shape and velocity of the thermal front depend on the thermal conductivity of the rock, relative permeability, and injection conditions (Pruess, 2005; Wapperom, dos Santos, & Voskov, 2024). As CO_2 expands and cools, the resulting thermal contrast with the surrounding rock induces conductive heat flow into the cooled region. This re-equilibration is regulated by the effective thermal conductivity and the equivalent volumetric heat capacity, which determine the rate at which thermal equilibrium is restored.

In high-permeability zones, rapid fluid advection enhances JT cooling, whereas in low-permeability formations, both fluid and thermal propagation are delayed. The resulting steep local gradients in tight rocks confine the thermal front, while in more permeable media, the cooling zone extends further into the formation. Heterogeneities on the pore scale introduce spatial variation in the thermal response, which can affect the integrity of the near-wellbore and the stability of the caprock (Oldenburg, 2006; H. Wang et al., 2019).

2.2.4. Latent Heat and Phase Transitions

Phase transitions increase the complexity in terms of thermodynamics. Rapid temperature drop may shift CO_2 to the two-phase region or induce localized condensation, especially under confinement. Experimental deviations from the predicted phase envelopes are attributed to pore-scale effects, kinetic constraints, and thermal diffusion lags (Li et al., 2020).

Latent heat plays a crucial role during phase transitions such as CO_2 vaporization, condensation, and hydrate formation. These processes absorb or release energy without altering the temperature, affecting the local energy balance and modifying the thermal gradients during injection. The phase transition governs the thermal response by releasing latent heat after condensation and absorbing it during

vaporization, making it the primary factor in shaping the observed thermal profile during CO_2 injection into dry cores.

These effects are especially pronounced under conditions of rapid pressure decline or constrained pore-scale geometry, where thermal equilibration is limited. Duffy et al. (1995) show that CO_2 confined in nanometer-scale pores undergoes phase transitions at temperatures significantly shifted from bulk behavior. Condensation occurs at elevated temperatures due to capillary effects, while freezing is suppressed by more than 10 °C, consistent with the Gibbs-Thomson predictions, which will be discussed in Section 2.3. These observations highlight the need for pore-scale corrections in thermal and phase-transition models.

Quantitative modeling of such effects necessitates the inclusion of latent heat terms in the energy balance:

$$Q_{\text{latent}} = m \cdot L. \tag{2.5}$$

Where m is the mass that undergoes a phase change and L is the specific latent heat (for example, $16.4\,\text{kJ}\,\text{mol}^{-1}$ for CO_2 evaporation (NIST, 2025)). Q_{latent} represents the energy absorbed or released during phase transitions without a change in temperature. In porous media, this term governs the intensity and persistence of thermal anomalies during injection. Simulators such as DARTS incorporate these contributions through enthalpy-based formulations, which dynamically adjust the local energy balance as the phase boundaries are crossed within each control volume.

2.3. Mechanisms Influencing Phase Boundary Offsets During CO_2 Injection

During dry CO_2 injection into porous media, deviations between observed and expected phase transitions - referred to as phase boundary offsets - can arise due to confinement, thermodynamic non-idealities and transport limitations. These offsets play an important role in determining the spatial and temporal behavior of phase changes, particularly under JT-dominated cooling conditions.

Gibbs–Thomson Effect The Gibbs–Thomson effect describes the thermodynamic shift in condensation conditions due to curvature-induced confinement. In porous media, smaller pore diameters raise the equilibrium vapor pressure and lower the condensation temperature, leading to a deviation from bulk-phase predictions. For a cylindrical pore geometry, the shift in condensation temperature is given by

$$\Delta T_c(x) = T_{cB} - T_c(x) = -T_{cB} \frac{4\sigma_{lv} \cos\phi}{\Delta H_{\text{vap}}\, \rho_l\, x}, \tag{2.6}$$

Where T_{cB} is the bulk condensation temperature, $T_c(x)$ is the condensation temperature in a pore of diameter x, σ_{lv} is the surface tension of liquid - gas, ϕ is the contact angle, ΔH_{vap} is the vaporization enthalpy, ρ_l is the density of the liquid and x is the diameter of the pores. This expression predicts a lower condensation temperature for smaller pores, with significant suppression occurring in tight or nanoporous media (Duffy et al., 1995).

Thermal Transfer Limitations The low thermal conductivity of dry rock samples restricts heat dissipation from the cooled CO_2 plume to the surrounding matrix. This slows the equilibration of the system, enabling extended undercooled zones and non-equilibrium phase behavior. The rate of thermal recovery and the specific heat capacities thus become a limiting factor in phase boundary realignment (Singh et al., 2020).

Pore-Scale Heterogeneity Variations in grain size, mineralogy, and pore connectivity introduce local deviations in the pressure and temperature distributions. These heterogeneities cause spatially variable phase behavior, with certain zones experiencing phase transitions earlier or later than predicted by homogenized models. Pore-scale simulations have confirmed that such structural variability leads to measurable offsets in condensation or expansion fronts (Z. Wang et al., 2021).

2.4. Numerical Modelling with DARTS

To resolve the complex thermohydraulic behavior of CO_2 injection and JT cooling in porous media, the *Delft Advanced Research Terra Simulator (DARTS)* is used (D. Voskov et al., 2024). DARTS is specifically developed for fully coupled thermal-compositional simulations in subsurface systems and is well suited for applications such as CCS and geothermal energy. It features real-gas thermodynamics, phase equilibrium calculations, and spatially resolved energy transport, which are essential for capturing transient cooling and phase transitions.

The simulator solves a unified conservation law for each chemical component and for thermal energy in a discretized control volume Ω:

$$\frac{\partial}{\partial t} \int_\Omega M^c \, d\Omega + \int_\Gamma \mathbf{F}^c \cdot \mathbf{n} \, d\Gamma = \int_\Omega Q^c \, d\Omega. \tag{2.7}$$

Here, M^c denotes the accumulation of conserved quantity c, $\mathbf{F}^c$ is the total flux across the control surface Γ, and Q^c is the source term. The index c spans all components and thermal energy; $j = 1, \ldots, n_p$ refers to the fluid phases.

The accumulation of the mass of the components is given by:

$$M^c = \phi \sum_{j=1}^{n_p} x_{c,j} \rho_j S_j \,, \quad c = 1, \ldots, n_c, \tag{2.8}$$

Where ϕ is porosity, $x_{c,j}$ the mole fraction of component c in phase j, ρ_j the phase density, and S_j the phase saturation.

The accumulation of thermal energy accounts for the internal energy in both fluids and rocks:

$$M^{c+1} = \phi \sum_{j=1}^{n_p} \rho_j S_j U_j + (1-\phi) U_r, \tag{2.9}$$

Where U_j is the specific internal energy of phase j, and U_r is the volumetric internal energy of the rock. Mass fluxes are described by:

$$\mathbf{F}^c = \sum_{j=1}^{n_p} \left(x_{c,j} \rho_j \mathbf{u}_j + S_j J_{c,j} \right), \tag{2.10}$$

With $\mathbf{u}_j$ the Darcy velocity and $J_{c,j}$ the diffusive flux of the component c in phase j.

The thermal energy flux contains an advective and conductive contribution:

$$\mathbf{F}^{c+1} = \sum_{j=1}^{n_p} \left(H_j \rho_j \mathbf{u}_j \right) - \lambda \nabla T. \tag{2.11}$$

Here, $H_j = U_j + PV_j$ is the specific enthalpy of phase j, and λ is the effective thermal conductivity. In particular, the term advective enthalpy reflects the transport of heat by moving fluid, whereas the conductive term governs the thermal diffusion in the rock–fluid matrix. These equations are solved in a finite-volume framework using the two-point flux approximation. The nonlinear closure is provided by an Equation of State (EOS) and full flash calculations, which ensure accurate phase behavior and property prediction across a wide range of pressures and temperatures. Further details of these derivations can be found in Tian et al. (2024) or Wapperom, dos Santos, and Voskov (2024).

The Joule–Thomson cooling effect arises naturally from the energy balance. As CO_2 expands and flows into lower pressure zones, the flux of advective enthalpy $\sum_j H_j \rho_j \mathbf{u}_j$ dominates. Because H_j drops with decreasing pressure (under isenthalpic or near-adiabatic conditions), the injected fluid cools as it moves, generating a transient cold front. This cooling is then partially counteracted by the conductive term $\lambda \nabla T$, especially at longer timescales. The interaction between these terms controls the shape and depth of the thermal front and allows DARTS to reproduce the experimental temperature drops.

2.4.1. Numerical Implementation and Thermodynamic Modeling

DARTS uses an operator-based framework to simulate coupled multiphase flow, thermal transport, and compositional changes in porous media. The simulator uses fully implicit time discretization (backward Euler) and finite-volume spatial discretization on structured or unstructured grids. Its computational efficiency comes from the operator-based linearization (OBL) method (D. V. Voskov, 2017), which separates the physics (e.g., mass and energy conservation) from the non-linear thermodynamic relations.

The core idea is to precompute nonlinear expressions, such as phase enthalpy, density, and mobility, into multidimensional lookup tables over the (P, T, x_c) space. These tabulated operators are stored during preprocessing using the `darts-flash` module (D. Voskov et al., 2024), and dynamically interpolated during the simulation to build the Jacobian and residuals. This approach avoids repeated EOS and property evaluations at every Newton iteration, significantly improving robustness and convergence in highly non-linear scenarios such as Joule–Thomson cooling and phase transitions.

Each grid block stores its own compositional and thermal state, allowing for localized phase behavior, including gas-liquid transitions and hydrate formation. Phase equilibrium (flash) calculations determine the number and type of phases present and resolve transitions between single-phase and two-phase regions. The thermophysical properties of CO_2, including density, enthalpy, viscosity, and heat capacity, are strongly dependent on pressure and temperature and are dynamically updated using real gas EOS tables.

This architecture ensures an accurate representation of the JT cooling phenomena, where enthalpy variations with pressure and temperature are central to physics. Because the cooling effect is directly

governed by the real-gas enthalpy gradient $\partial H/\partial P|_T$, a robust EOS framework and adaptive resolution of thermodynamic states are essential. The combination of operator-based linearization and tabulated thermodynamics allows DARTS to simulate these effects efficiently and in line with experimental observations.

Source Code

The open-DARTS source code is available through GitLab [1]. It has been extensively benchmarked against other compositional simulators and validated for geothermal, CO_2, and hydrogen applications (D. Voskov et al., 2024; Wapperom, Tian, et al., 2024).

2.5. Knowledge Gaps and Relevance to This Study

Although many studies address JT cooling from a theoretical or numerical point of view, few provide direct experimental validation under dry-core, low-pressure conditions analogous to depleted fields. Most existing work also assumes homogeneous pore-scale thermal transfer, ignoring the confinement effects critical for predicting phase-transition delays. This thesis addresses this gap through systematic core-scale experimentation and cross-verification with open-DARTS modeling. The selection of Bentheimer and Kentucky sandstones reflects distinct permeability regimes, offering a contrast in the JT response under otherwise controlled conditions.

In this thesis, DARTS is used to simulate laboratory-scale core experiments of CO_2 injection under low backpressure conditions. Special attention is paid to the temperature evolution within the porous core and the accuracy of front propagation in response to real injection parameters. The numerical model is benchmarked against experimental measurements, with sensor-specific validation performed for both the temperature and the pressure response.

The key parameters calibrated include grid resolution, EOS point density, and effective thermal conductivity. These are tuned to ensure that the cold-front dynamics observed in the Bentheimer and Kentucky sandstones are accurately reproduced.

[1] https://gitlab.com/open-darts/open-darts

3

Experimental Setup

To investigate Joule-Thomson (JT) cooling during CO_2 injection into porous media under near-reservoir conditions, a core flooding setup was designed and constructed. This chapter details the design of the core holder, the fluid injection system, the sensor configuration, the data acquisition procedures, and the calibration steps used throughout the experimental campaign.

3.1. Experimental Objectives and Design Philosophy

The experimental campaign is designed to isolate and quantify the Joule-Thomson cooling effect during CO_2 injection into porous rock under controlled laboratory conditions. The primary objective is to observe and characterize the development of thermal fronts and cooling power resulting from isenthalpic expansion, under specific flow rates and pressure drops representative of near-wellbore CCS injection scenarios. It is also possible to analyze the permeability, which is important for numerical models (e.g., DARTS).

Figure 3.1 shows the experimental setup in schematic form, detailing the positions of all key components, including absolute pressure sensors (P1, P2, etc.), temperature sensors (T1, T2, etc.) and differential pressure sensors (dP1, dP2, etc.).

Appendix D.3 provides an overview of the components used in the experimental setup, along with their specifications. A summary table is also included to indicate which parts were employed in each experiment, enabling clear tracking of modifications made throughout the experimental campaign.

3.2. Scope and Limitations

The experimental program investigates how pressure drop, flow rate, and rock properties influence temperature evolution during injection, with a particular focus on the magnitude and spatial extent of Joule-Thomson induced cooling, using a core flood setup designed to simulate near-wellbore conditions in depleted reservoirs.

In parallel, preliminary numerical simulations using the Delft Advanced Research Terra Simulator (DARTS) are employed to complement the experimental results. These simulations serve as a tool for interpreting observed temperature and pressure profiles, evaluating energy balances, and estimating the onset of phase transitions.

However, several limitations apply to the scope of this study:

- **Hydrate formation is not directly modeled or visualized.** While the study focuses on the thermodynamic preconditions for hydrate formation, it does not simulate or observe hydrate nucleation and growth explicitly due to the lack of water saturation in the core. The assumptions about hydrate risk are made on the basis of the temperature and pressure proximity to known stability boundaries.

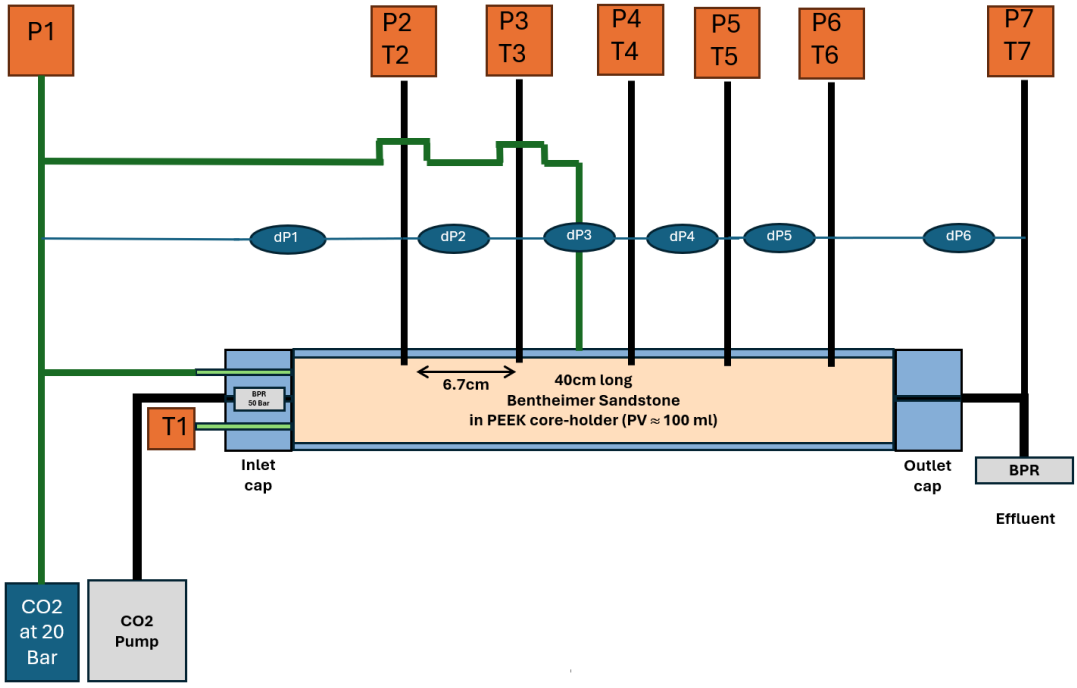

Figure 3.1: Schematic of the experimental CO_2 flooding setup. Sensor labels mark absolute pressure (P), temperature (T), and differential pressure (dP) sensors along the flow path.

- **Scaling to reservoir conditions is limited.** The experimental setup operates at laboratory scale and under ideal conditions. Spatial heterogeneity, capillary effects, and long-term thermal interactions present in real reservoirs are not fully captured. As such, results should be interpreted with caution when extrapolating to field-scale injection scenarios.
- **Gas purity and multi-component effects are not considered.** The experiments assume pure CO_2 injection. The presence of impurities (e.g. CH_4, N_2) could alter the Joule-Thomson coefficient and hydrate stability, and this complexity lies beyond the scope of the current study.

3.3. Overview of Core Properties

The experiments in this thesis were conducted using two distinct sandstone cores: Kentucky and Bentheimer sandstone. The goal was to capture the effect of permeability and pore structure on the magnitude and spatial propagation of JT cooling. This section provides an overview of their key physical properties, geometry, porosity, permeability, and effective pore scale, as well as the rationale behind their selection. Tables 3.1 and 3.2 summarize the essential core parameters used in the respective experiments.

3.3.1. Kentucky Sandstone

The Kentucky sandstone used in this study is a fine-grained light gray rock excavated from the western portion of the Kentucky Coal Field. It belongs to the Caseyville Formation, deposited during the Lower Pennsylvanian period (AlKharraa et al., 2023). These depositional conditions produced well-sorted quartz-dominated sandstones with moderate clay content and low intrinsic permeability.

Petrophysically, the core exhibits a porosity of approximately 15% and a permeability of 0.37 mD. The clay fraction is dominated by illite (3 wt%), which forms pore-bridging structures that reduce the effective diameter of the pore throat (AlKharraa et al., 2023). Illite is considered chemically inert under the tested conditions and is therefore not expected to significantly influence CO_2-rock interactions.

This lithological composition makes Kentucky sandstone a suitable analogue for tight reservoir formations. Low permeability induces large pressure gradients during CO_2 injection, allowing JT

cooling to occur readily. This enables direct comparison with DARTS simulations that apply fixed boundary pressures.

Despite the dimensions at the laboratory scale, the low-permeability regime serves as a physical analogue for field-scale reservoirs. In large formations (hundreds of meters in length), the cumulative pressure drop across the reservoir often parallels that observed across a short, low-permeability laboratory core. As such, this experimental setup offers a practical representation of near-wellbore thermal and pressure dynamics in real CCS scenarios, particularly under conditions where flow is dominated by JT effects and thermal diffusion is limited.

Table 3.1: Overview of Kentucky core parameters

Parameter	Value
Core material	Kentucky sandstone
Length	40 cm
Diameter	3.9 cm
Porosity	~15%
Permeability	0.37 mD (measured)
Effective pore radius	1.5 µm (estimated)
CT verification of sensors positions	Included (Figure A.2)

3.3.2. Bentheimer Sandstone

The Bentheimer sandstone core was selected for its well-characterized petrophysical properties and high permeability, which typically ranged from 1 to 2 Darcy. This high permeability minimizes internal pressure gradients during CO_2 injection, making it an ideal medium for isolating and analyzing JT cooling effects under controlled boundary conditions.

Geologically, Bentheimer is a quartz-rich sandstone from the Lower Cretaceous period. It exhibits high porosity (21-27%), resulting in uniform pore structures and consistent flow properties along the core (Peksa et al., 2015). Its minimal mineralogical reactivity with CO_2 ensures thermal and hydraulic stability during experiments.

To induce measurable JT cooling, an artificial pressure drop was imposed at the inlet using a back pressure cartridge (BPC). This configuration ensures that the majority of the pressure loss occurs abruptly at the core inlet, producing a sharp temperature drop and initiating a cold gas/liquid front that propagates downstream. Due to the high permeability, further pressure changes along the core are minimal, and observed thermal gradients are primarily driven by advection and conduction rather than continued isenthalpic expansion.

The Bentheimer experiments help isolate cooling effects under idealized flow conditions, providing a simplified system for gaining a better understanding of the fundamental thermodynamics.

Table 3.2: Overview of Bentheimer core parameters

Parameter	Value
Core material	Bentheimer sandstone
Length	40 cm
Diameter	3.9 cm
Porosity	~22%
Permeability	1.2-2 Darcy (measured)
Effective pore radius	20 µm (estimated)
CT verification of sensors positions	Included (Figure A.1)

3.4. Core Holder Design Schematics

The core holder was fabricated from polyetheretherketone (PEEK), a high-performance polymer selected because of its excellent mechanical stability, chemical inertness, and low thermal conductivity. These

characteristics ensure both structural integrity under high-pressure conditions and effective passive insulation to minimize heat loss during experiments.

Table 3.3: Core holder design and material properties

Parameter	Value
Core holder material	Polyetheretherketone (PEEK)
Outer diameter	98 mm
Inner diameter (core chamber)	48 mm
Length	400 mm
Wall thickness	25 mm
Thermal conductivity	~0.25 W/m·K (hpp-performance, 2019)
Sensor access	7 thermocouple ports
Sensor spacing	6.7 cm
Endcap fittings	Swagelok-compatible stainless steel (1/8″ 316)
Valves	High-pressure ball and check valves
Temperature insulation	Passive (PEEK body)

The cylindrical core chamber is sealed at both ends with end caps equipped with Swagelok fittings and o-rings for secure, leak-proof fluid connections, details can be seen in Table 3.3. Radially aligned and axially spaced holes facilitate the placement of thermocouples. A schematic of the assembly can be seen in Figure 3.2.

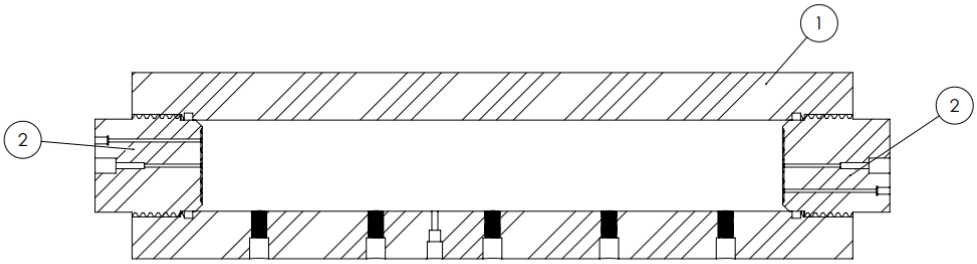

Figure 3.2: General core holder drawing showing the full PEEK housing (1) with threaded caps and sensor access points. The core chamber is 400 mm long , seated between dual-threaded caps (2).

3.5. Back pressure Regulation System

Two different back pressure regulators will be used in this setup; to differentiate between the two systems, the following table defines the naming that consistently will be used in the rest of this document.

Table 3.4: Back pressure regulation overview

Component	Position	Function
Inlet back pressure cartridge (BPC)	Upstream of core (optional use)	Pre-core pressure control
Outlet back pressure regulator (BPR)	Downstream of core	Controls the reservoir pressure

The inlet back pressure cartridge (BPC) is used to induce the primary pressure drop from high-pressure liquid CO_2 to lower-pressure gas phase conditions prior to injection into the core. This design enables controlled initiation of the JT cooling effect at manageable flowrates, particularly important when working with a high-permeability sample such as Bentheimer sandstone, where significant pressure drops would otherwise require flowrates on the order of tens of liters per minute.

The BPC is installed upstream of the coreholder and is configured to impose a fixed pressure drop, typically 37.5 or 50 bar depending on the cartridge type. These cartridges are factory-set and nonadjustable,

but can be interchanged to vary the applied pressure drop. Although this fixed design improves the repeatability and stability of the experiments, it also imposes constraints on operational flexibility. A schematic of the BPC endcap and its integration into the flow system is provided in Figure 3.3. Commercially available BPC was found to show poor performance under low-flow conditions, especially

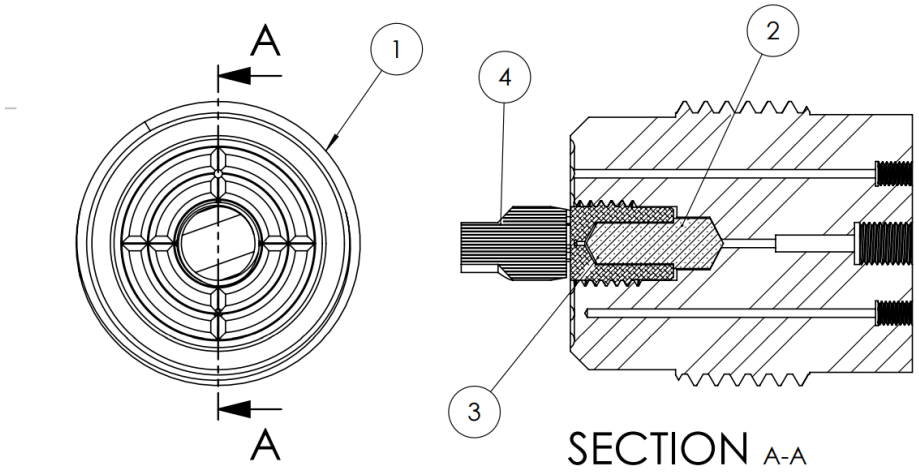

Figure 3.3: Technical drawing of the custom back-pressure cartridge endcap (1) assembly. The threaded screw tool (4) allows quick changes of the cartridge (2) to accommodate a pressure drop suitable for the current experiment.

below 4 mL/min. The primary issues included; elastomer swelling due to CO_2 exposure and pressure instability due to internal hysteresis and slow response times.

To address these challenges, multiple cartridge configurations were tested with varying O-ring materials and geometries, see Table D.2 for the complete list of tested materials. Final assemblies used either Teflon or Fluorine Kautschuk Material (FKR)- o-rings of specific sizes, chosen for their chemical inertness, mechanical stability under thermal cycling, and minimal hysteresis. These design refinements enabled smooth pressure transitions and reproducible JT cooling observations even at lower flow rates.

The function of the inlet BPC is analogous to that of a downhole choke valve in field operations. In high-permeability formations, downhole chokes are often used to impose a localized pressure drop near the wellbore, enabling controlled throttling and phase management at depth. Similarly, in the laboratory setup, the inlet BPC enforces a predefined pressure drop upstream of the core, ensuring that JT cooling is initiated under controlled and repeatable conditions, even when mass flowrates would otherwise be insufficient to create a significant pressure gradient.

The inlet BPC is only used in the Bentheimer experiments, as Kentucky sandstone has a significant pressure gradient of itself; it is not required and would overcomplicate the setup.

In contrast, the outlet back pressure regulator (BPR) serves to simulate the pressure of the reservoir by setting the downstream boundary condition of the experiment. This regulator is adjustable and can be tuned to the desired outlet pressure, allowing exploration of various injection scenarios and phase behavior envelopes. It effectively defines the pressure at which CO_2 exits the core and thus influences the extent of expansion along the core.

3.6. CO_2 Injection and Pressure Regulation System

CO_2 was injected into the core using a Vindum high-precision dual piston pump, capable of delivering high-volume constant flow rates with fine control. During each experiment, CO_2 was supplied from a main line to a gas booster to ensure that it enters the liquid phase. Once liquefied, it entered the Vindum system, where flowrates between 2.5 and 15 mL/min of liquid CO_2 could be maintained consistently.

CO_2 entered the experimental setup at pressures exceeding 65 bar, ensuring it remained in the liquid phase prior to expansion, with the exception of a single experiment (ex15) to evaluate gas-to-gas expansion. Downstream, a rapid pressure drop, induced by the inlet BPC for the Bentheimer or naturally for the Kentucky sandstone, converted the fluid to the gas phase.

Problems of flowrate overshoot or instability due to compression of the pump head and delayed BPC regulation were mitigated by ensuring that the outlet BPR was well maintained and the inlet BPC had the correct o-rings installed. Experiments typically lasted between 30 minutes and 3.5 hours, depending on the injection volume and the propagation speed of the cooling front. The total injected volume ranged from 200 to 900 mL (in the liquid state) of CO_2 per test.

3.7. Data Processing and Filtering

In several experiments (ex3, ex4, ex6, ex8 and ex12), malfunctions or delayed responses of the BPC or BPR introduced fluctuations in the sensor data, obscuring the underlying thermal and pressure trends. Temperature and pressure data were logged at 1 Hz for all channels using the MP3 data acquisition system. Although Type K thermocouples offer a nominal temperature resolution of 0.01 K, they remain susceptible to environmental fluctuations, thermal lag, and digital noise.

To extract meaningful profiles, a sequence of post-processing steps was applied. A moving average filter was used to smooth high-frequency noise without compromising the integrity of the thermal fronts. The filter window was set to 1% of the total duration of the experiment and was only applied in the cases where the initial pressure data were unreadable due to the high levels of noise. Graphs processed in this way are annotated as (smoothed) for the sake of clarity. Sensor baselines were corrected using a reference temperature channel, T-Room, placed near the setup but not in contact with it, providing an accurate measure of ambient temperature. The offsets were then applied to align all sensors to a common pre-injection baseline within ±0.1 K. Differential pressure readings were filtered using the same moving average method to remove digital spikes while preserving physical gradients.

Although a 1% filter window may appear large, preliminary tests confirmed that it provided an optimal compromise between noise reduction and readability of the underlying thermal signal. All sensor outputs were exported in CSV format and processed using a Python script, with automated alignment, filtering, and synchronized plotting of pressure and temperature data, ensuring uniform processing and consistent visual presentation in all experiments.

3.8. Experimental Procedure

The coreholder and the general description of the entire setup can be seen in Figure 3.4 and Figure 3.5. Each experiment followed a standardized protocol designed to ensure repeatability and minimize external sources of error. The following steps outline the sequence of activities leading up to, during, and following CO_2 injection:

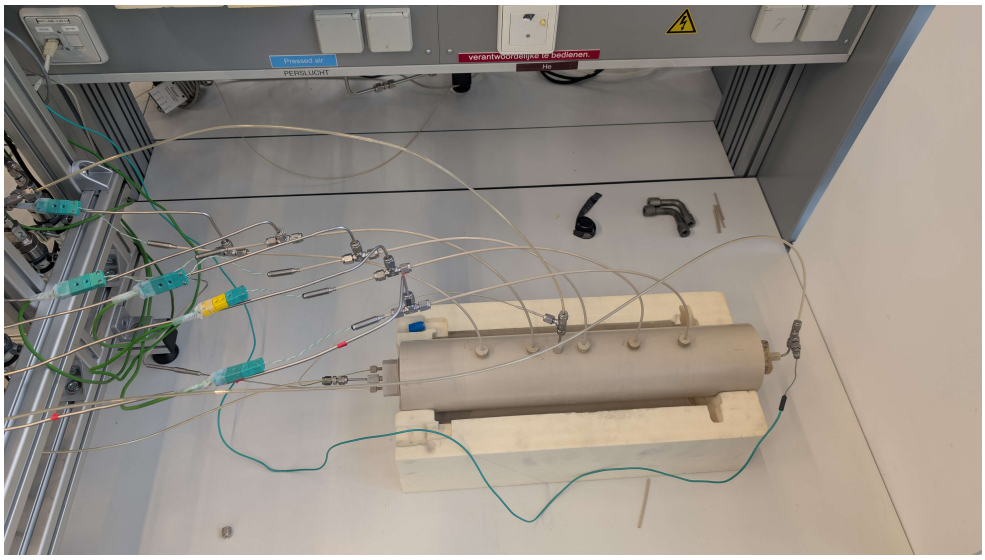

Figure 3.4: Close-up of the core holder showing thermocouples inserted through sealed ports. Sensor wiring is arranged across the top surface of the PEEK housing.

Figure 3.5: Wide-angle view of the experimental lab setup. From left to right: The Booster, Vindum pump station, sensor panel, core holder bench, and data acquisition system are all integrated into a single test rig.

1. **System preconditioning:** Prior to the first experiment, the core was flushed with dry CO_2 (to suppress any hydrate formation), which would complicate interpretation. The coreholder was then brought to thermal equilibrium with the ambient laboratory environment by leaving the system idle for a minimum of 12 hours to ensure a stable baseline temperature. All sensors were zeroed under static, no-flow conditions to establish a consistent reference state.
2. **Back pressure regulator heating:** The outlet back pressure regulator was preheated to 50°C using an external heating plate. This step was to prevent internal elastomer components from freezing during the cooling phase, which could cause back pressure instability.
3. **System pressurization:** With the core in place, both the confining pressure and the back pressure of the outlet gradually increased to their target values. This was performed stepwise to allow for inspection of all connections, valve positions, and pressure seals. Continuous leak testing is performed at this stage, while taking care that no Snoop (leak detection fluid) is dropped on the temperature sensors, which can influence the measurement.
4. **Digital system setup:** The Vindum pump controller and MP3 logging system were initialized. Experimental metadata, including injection volume, backpressure regulator setting, and target pressure drop, was encoded into the file naming convention. The files are started with a sampling rate of 1 Hz.
5. **CO_2 injection:** Once the initial conditions were verified, the valve leading to the inlet of the core was opened and the Vindum pump was activated to start the injection of liquid CO_2. Temperature and pressure were continuously monitored to observe the arrival and progression of the thermal front.

    5.1 **Visual inspection practices:** During injection, the external temperature of the PEEK outer housing and the outlet tube was regularly monitored by thermal imaging to detect the development of localized cold spots, a warm BPR, and potential indicators of sensor malfunctions or leaks. Thermal losses through the outer wall were later analytically estimated (see Section 5.3.6).
6. **Termination of injection:** Termination of the experiment was usually based on a sudden temperature drop at Sensor 7, indicating breakthrough of the cooling front to the outlet of the core. The flow was stopped when maximum cooling was achieved at T7 and liquid CO_2 visually observed exiting the tube at the end of the core.
7. **Post-injection monitoring:** Following injection, data recording was continued for an additional 15–30 minutes. This allowed observation of thermal rebound behavior, potential repressurisation effects, and any delay in sensor response due to core heat capacity or residual gas expansion.

3.8.1. Numerical Simulation Workflow Using DARTS

To complement the core-flooding experiments, numerical simulations were performed using DARTS. These simulations aimed to replicate the thermal and pressure evolution during CO_2 injection into porous media and to evaluate the sensitivity of the model to spatial resolution and the sensitivity of the Equation Of State (EOS). The Kentucky sandstone core, specifically experiment ex17, was selected as the baseline case due to its large pressure gradient, representative of the field and the absence of a back pressure cartridge. This configuration allowed for a more realistic comparison with natural reservoir conditions, without introducing high flowrates.

The simulation domain was modeled as a one-dimensional core with a uniform grid, typically consisting of 40 to 40000 cells. The boundary conditions mirrored those of the experimental setup: a fixed injection rate, a constant outlet back pressure regulator (e.g., 20 bar), and a uniform initial temperature of 293 K.

Thermodynamic properties of CO_2 were provided through EOS, generated using 101 to 2001 OBL points throughout the pressure-temperature space. These tabulations were essential for resolving non-linear behavior near the vapor–liquid saturation boundary and evaluating the impact of EOS smoothness on the resulting JT trajectories.

To explore the role of multiphase effects, additional simulations introduced an initial water saturation 90% as a proxy for liquid CO_2 accumulation. This allowed relative permeability restrictions to be approximated, improving agreement with experimental pressure build-up.

Finally, a scale-up simulation was conducted using a 400 m domain with 400 cells, representing a higher-permeability reservoir (375 mD) to demonstrate the comparison with larger-scale systems and their behavior.

Post-processing was handled using a custom Python routine that extracted temporal temperature minima, tracked phase evolution, and overlaid experimental sensor positions for direct comparison. These tools were relevant to quantify the differences between the experiment and the simulation.

4

Experimental Results: Kentucky Sandstone Series

This chapter presents the results of a series of gas- and liquid-phase CO_2 injection experiments. The aim was twofold: (1) to determine whether JT cooling can be effectively triggered and observed in low-permeability rock under field-relevant pressures and flowrates, and (2) to investigate how strongly thermal responses vary spatially and temporally under different injection regimes.

Permeability tests were performed before and after the cooling experiments. These results confirmed the mechanical stability of the core and ensured that changes in cooling behavior could be confidently attributed to injection conditions, not evolving rock properties.

Three different JT injection regimes were tested. The first (ex15) used gas-phase CO_2 at low flow to assess whether cooling could be induced by gas–gas expansion alone. The next (ex16) involved the injection and subsequent depressurization of liquid CO_2. Finally, a trio of experiments (ex17–ex19) injected CO_2 in the liquid state and allowed it to expand inside the porous core, at various injection rates and pressure drops.

4.1. Kentucky Core Permeability

A series of gas-phase permeability experiments were conducted using the Kentucky sandstone core to evaluate its intrinsic permeability under controlled flow conditions. These tests also serve to calibrate simulation models. The permeability results are first summarized in Table 4.1; detailed analysis and interpretation can be found in the Appendix C.

A second set of post-experiment measurements was used to assess whether the large imposed pressure during some JT cooling experiments, resulted in blockage of the pore pathways. Any deviation in permeability relative to the pre-experiment baseline would indicate irreversible alteration of the pore structure, requiring adjustment of the numerical model inputs.

Table 4.1: Overview of Kentucky core permeability estimates

Segment	**Pre-Experiment k_{int} [mD]**	**Post-Experiment k_{int} [mD]**
Segment 1	0.31	0.33
Segment 2	0.32	0.33
Segment 3	0.35	0.36
Segment 4	0.36	0.37
Segment 5	0.38	0.39
Segment 6	0.41	0.41

The intrinsic permeability values for the Kentucky core fall between 0.3 and 0.4 mD, aligning well with expectations. Compared to Bentheimer, these values are three to four orders of magnitude lower, consistent with the literature (AlKharraa et al., 2023).

4.2. Overview of Joule-Thomson Cooling Experiments in Kentucky Sandstone

The experiments will ensure that gas or liquid CO_2 is injected and undergoes a JT expansion within the porous medium, creating a local temperature drop. Table 4.2 summarizes the Kentucky sandstone series tests. The minimum temperature is not shown as this changes significantly for each sensor. More details can be found in Appendix D.6.2.

Table 4.2: Summary of Kentucky experiments

Exp.	Flow (mL/min (liq.) CO_2)	Inlet P (bar)	BPR (bar)	duration (hh:mm)	phase
ex15	~1.82†	50	0	22:13	Gas–Gas
ex16	0	65	40	01:40	L-G (no inj.)
ex17	5	68	20	00:47	Liquid–Gas
ex18	7	68	25	00:33	Liquid–Gas
ex19	3	68	33	01:20	Liquid–Gas

† Based on 88 g/h CO_2 injection rate (density at 68 bar ≈ 804.12 kg/m^3 (NIST, 2025)).

4.3. Experiment ex15 — Gas-Phase Injection Without Back Pressure

Experiment 15 aimed to determine whether gas phase expansion alone, at moderate injection rates, could produce measurable JT cooling in the low-permeability Kentucky sandstone core, without any other phenomena, such as evaporation, that contribute to the cooling effect. In this configuration, CO_2 was injected at an inlet pressure of 50 bar, with no imposed outlet BPR (atmospheric outlet, 0 bar gauge). The entire pressure drop thus occurred across the core. The total CO_2 injection rate was measured at 88 g/h at the inlet of the core, which given the gas density under these conditions (~804.12 kg/m^3), corresponds to an average volumetric flowrate of approximately 1.82 mL/min of liquid CO_2 injected at the inlet compared to the other experiments.

4.3.1. Temperature Response

Figure 4.1 shows the temperature profile of ex15. The lowest temperature, recorded by T6, was approximately 12.2°C.

Although cooling is clearly present, it occurs slowly and is sensitive to environmental perturbations. These results suggest that the injected gas lacked sufficient cooling power to provide consistent cooling. Instead, the observed behavior is governed by slow thermal diffusion and ambient heat flux from the surroundings. In particular, around t = 20,000 s, a rise in ambient laboratory temperature caused a complete halt in the cooling trend, suggesting that the system was operating near the thermal equilibrium threshold with its surroundings. The upward trend in temperature across all sensors at the end of the experiment suggests that the cooling power associated with gas–gas expansion was insufficient to overcome heat losses, thus the experiment was stopped.

4.3.2. Pressure Response

Figure 4.2 displays the evolution of the pressure during ex15. As differential pressure sensors (max range of 3 bar per sensor) were outside their working range, only absolute pressure sensors were used.

The pressure drop over each segment increases significantly near the outlet (Ps5–Ps7). This behavior is consistent with compressible gas flow: As the gas expands downstream, its velocity increases, resulting in higher local friction, and thus higher pressure loss per unit length. This confirms that even at modest flowrates, gas expansion exerts a non-trivial effect on the downstream pressure distribution.

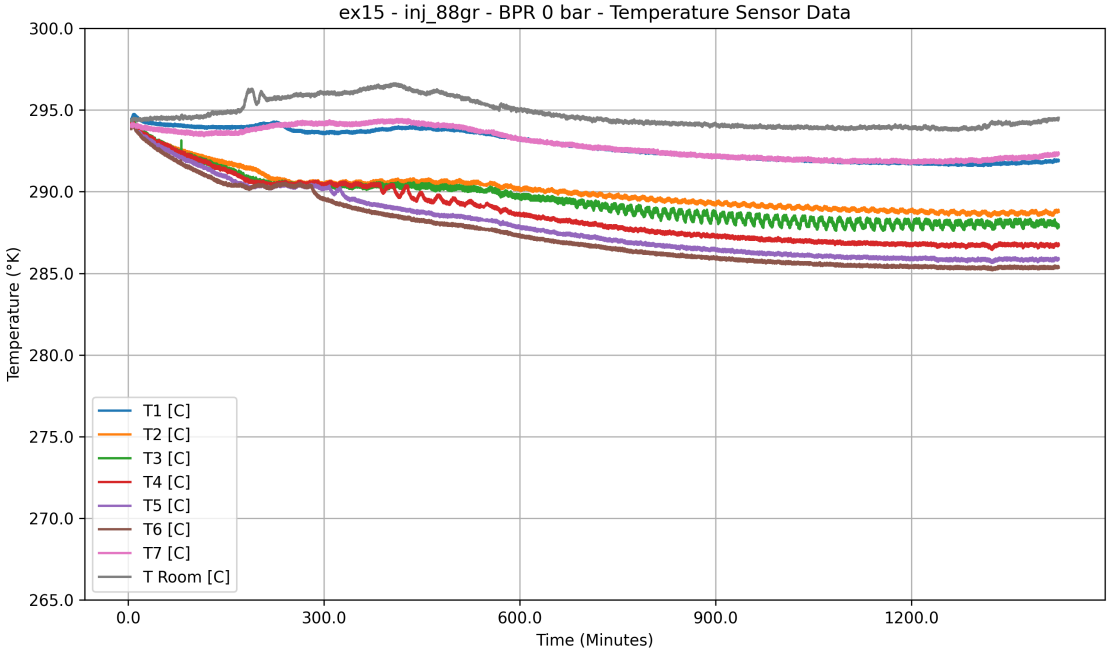

Figure 4.1: Temperature response during ex15. Cooling is observed across all sensors, but easily disturbed by an increase in room temperature. T6 records the lowest temperature.

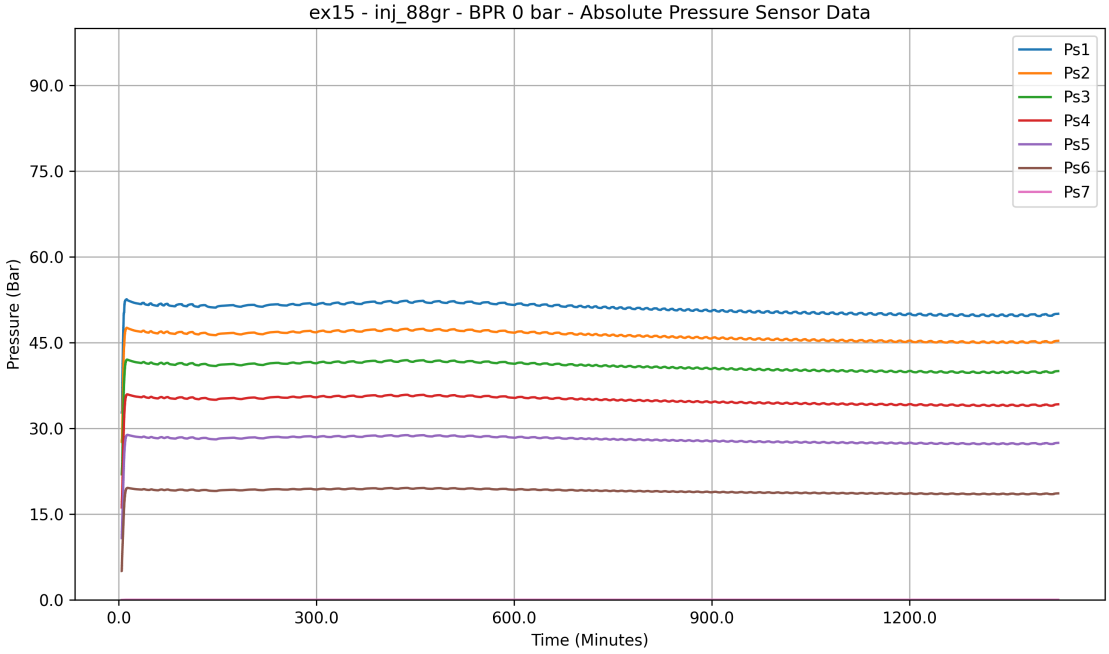

Figure 4.2: Pressure response during ex15. A nonlinear pressure drop develops toward the outlet due to volumetric expansion of the gas.

4.4. Experiment ex16 - Depressurizing Phase of the Core

Experiment 16 was the first test performed on the Kentucky sandstone core with direct injection of liquid CO_2. During the initial stage, the injection rate was set higher than the optimal setting in combination with the set pressure for the BPR resulting in the injection of liquid CO_2 at high pressure without substantial JT cooling. Within the first 3 minutes, the system rapidly pressurized and stabilized, and the injected CO_2 remained largely in the liquid phase throughout the core, suppressing cooling due to the

absence of expansion. This caused liquid CO_2 to exit the core at T7, which could be observed in the outlet tube.

Instead of looking at the injection phase, the focus of the analysis was shifted to the depressurization phase after the injection was stopped. This reversal of the usual experimental condition offered an opportunity to observe phase change dynamics and thermal response as the core discharges and the liquid CO_2 front recedes toward the inlet. Although this method does not achieve the same cooling magnitude as during injection, it allows for clear and time-resolved tracking of the in-core phase boundary and depletion behavior.

Figure 4.3 shows the evolution of the temperature and pressure after stopping the injection. The retreat of the liquid CO_2 front is evident in both datasets. At around 13 minutes, when the injection is stopped, the pressure curves for all sensors converge and begin a gradual decline in order from Ps7 (outlet) toward Ps1 (inlet), corresponding to the progressive vaporization and pressure equalization as the liquid evaporates. The temperature signals exhibit a similar behavior: the minimum temperatures are observed first at T7 and then sequentially upstream toward T1, consistent with the reverse motion of a cooling front governed by delayed phase transition and local expansion.

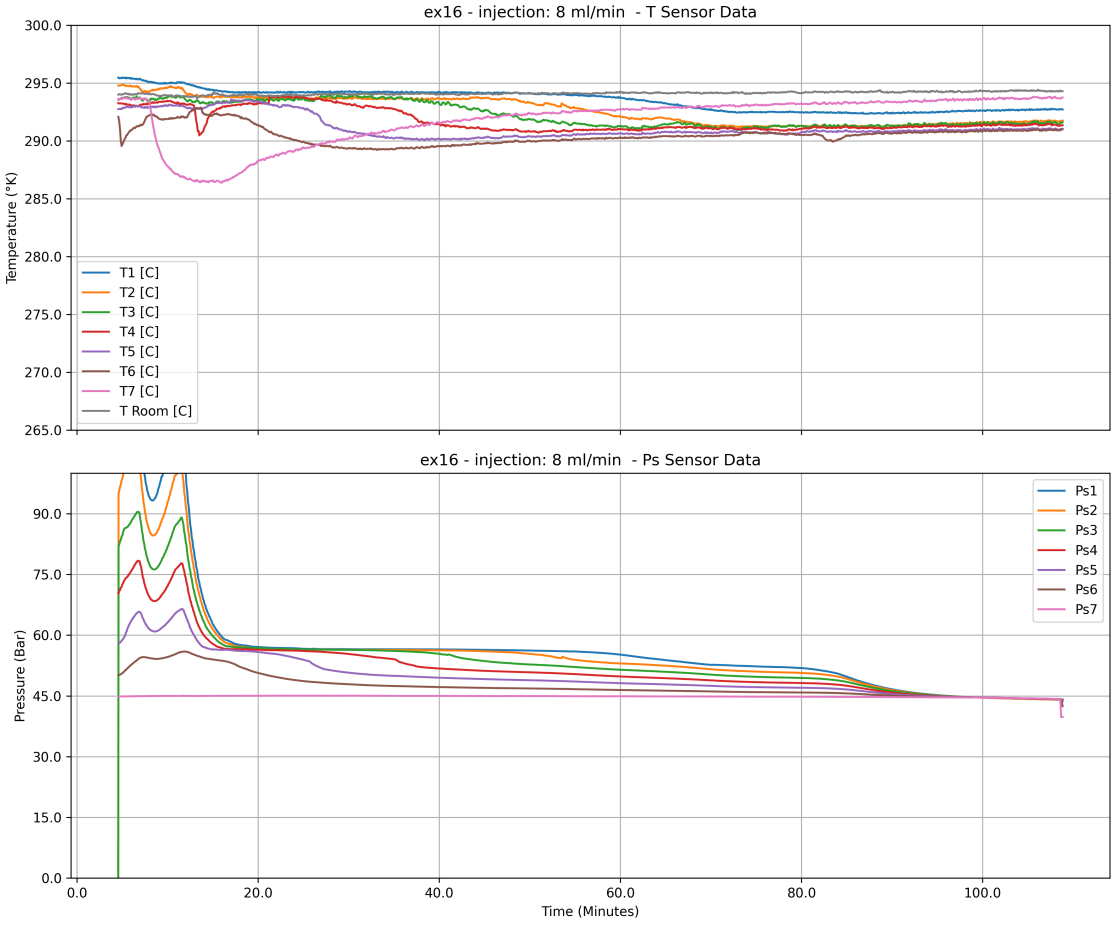

Figure 4.3: Temperature and pressure response of ex16 following injection shutdown. The depressurization phase causes a reverse migration of the liquid CO_2 front from outlet to inlet, with corresponding phase change and cooling signals observable across the core.

4.5. Experiment ex17 — Liquid-Phase Injection Without Back Pressure

As observed in ex15, it was essential to generate sufficient cooling power to consistently overcome ambient thermal losses, something that proved difficult under gas-phase injection alone. Therefore, experiments ex17, ex18 and ex19 were designed to increase both the injection rate and the pressure, allowing the injection of CO_2 in its liquid state and facilitating its expansion to the gas phase within the core, while maintaining a low outlet pressure. This configuration more accurately represents the subsurface conditions encountered during field-scale liquid CO_2 injection.

In experiment ex17, the injection conditions were increased to support liquid-phase CO_2 flow. The system was operated at an inlet pressure of 68 bar with an outlet back pressure of 20 bar, resulting in a net pressure drop of 48 bar across the core. A flowrate of 5 mL/min of liquid CO_2 was injected.

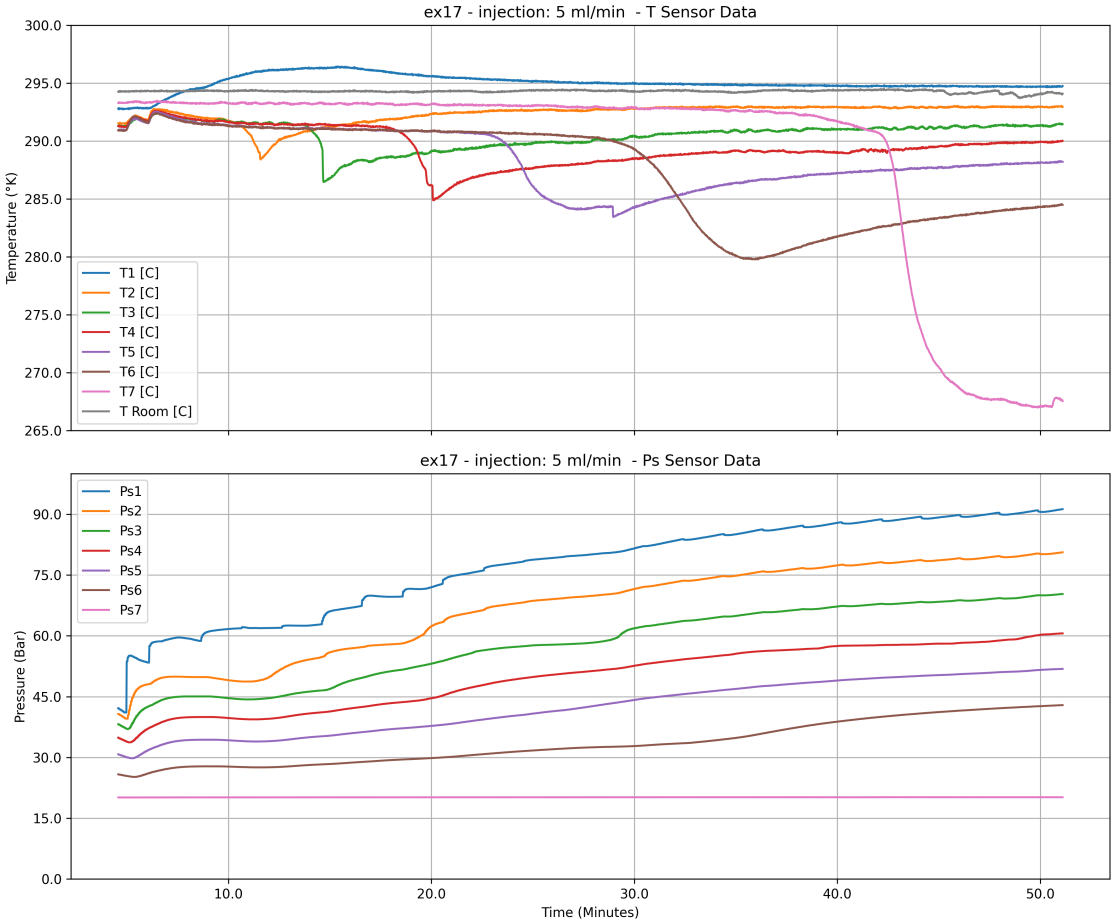

Figure 4.4: Temperature (top) and pressure (bottom) profiles during ex17. A sharp thermal front is observed, with distinct segmental responses indicating phase transitions.

The temperature response of experiment ex17 reveals several phenomena. Initially, a temperature increase is observed at the inlet sensor (T1), which is attributed to compression heating. Due to the relatively high injection rate in combination with the low permeability of the Kentucky core, CO_2 accumulates at the inlet, causing local pressurization. This results in a reverse JT effect and a corresponding rise in temperature. As injection continues, each sensor records a temperature drop, followed by a sharp drop that progresses sequentially from T2 through T7. This pattern indicates the advancement of a cooling front along the core.

After the sharp drop, a thermal rebound is observed at most locations. The absence of additional cooling allows residual heat from the surrounding rock matrix to warm the local region, gradually shifting it

toward a new steady state. Notably, the degree of cooling differs spatially: T2 shows a relatively shallow minimum, while T7 exhibits significantly lower temperatures. This gradient is directly linked to local pressure: lower pressures near the outlet allow for more extensive cooling via gas-phase expansion, whereas higher pressures near the inlet suppress this effect. This is explained by phase transitions induced by local cooling: once the temperature drops below the phase boundary line, liquid CO_2 forms and stops the cooling of the JT due to expansion.

The pressure data confirm this interpretation. The Kentucky core exhibits a substantial pressure build-up, from 40 bar to 70 bar during the experiment. This increase results from flow resistance induced by the progressive formation of liquid CO_2 within the porous structure. The liquid phase significantly impedes flow, leading to a system-wide increase in pressure as the experiment proceeds.

The bottom panel of Figure 4.4 shows a steady pressure gradient forming across the core. The increase in dP from start to finish is likely caused by a combination of increased liquid CO_2 content and temperature drop, both factors increasing fluid viscosity. Later, the Bentheimer results in Chapter 5.3.2 will demonstrate similar trends.

Follow-up Experiments: ex18 and ex19

To validate and extend the observations of ex17, two follow-up experiments were conducted, ex18 and ex19, designed to test the system response under varying injection rates. Figures associated with ex18 and ex19 are included in Appendices D.16 and D.17, allowing comparison between varying injection regimes. Together, these three experiments form a coherent series that strengthens the interpretation of thermal signals under progressively more favorable conditions for JT cooling in low-permeability media.

Experiment ex18 was executed with a reduced injection flowrate of 3 mL/min of liquid CO_2, specifically to investigate the transient thermal behavior near the minimum temperature. In ex17, the sensors exhibited a sharp and rapid temperature rebound shortly after reaching their minimum values, likely due to high-rate injection pushing the liquid front forward before thermal equilibration was achieved. The lower injection rate in ex18 slowed the front progression, giving the temperature sensors more time to stabilize, and thus improving the likelihood of capturing the true minimum temperature at each location. This helped confirm the consistency and accuracy of the minimum temperature data observed in earlier tests.

Experiment ex19, in contrast, increased the injection rate to 7 mL/min of liquid CO_2 to amplify the effects of compression heating at the inlet, particularly the temperature increase observed at T1 in ex17. This allowed for more robust testing of the hypothesis that rapid injection in a confined pore network induces local overpressure and warming, a reverse JT effect. In fact, a stronger temperature spike was observed at the inlet, validating the thermal interpretation.

Furthermore, ex19 aimed to push the outlet sensors (T6–T7) closer to their theoretical temperature limits (according to the PT curve, discussed in Chapter 7) by increasing the cooling power. However, the required temperatures were too low to be fully reached due to thermal conduction losses at the outlet and the limited residence time of CO_2 in that region. Although full saturation was not observed, the experiment confirmed the expected qualitative trends and added further weight to the hypothesis.

5

Experimental Results: Bentheimer Sandstone Series

This chapter presents results from a series of CO_2 injection experiments conducted on the Bentheimer sandstone core. The primary objective is to characterize Joule-Thomson (JT) cooling under controlled conditions and evaluate the thermal front behavior across different injection scenarios. Due to the quasi-steady-state conditions achieved during the experiments, it became feasible to perform simplified thermal calculations to evaluate heat transfer mechanisms and isolate other parameters for further analysis.

Permeability measurements were conducted using CO_2 gas under varying flow and pressure conditions to estimate input parameters for numerical simulations, in the same manner as the Kentucky permeability tests. At this stage of the experimentation, it was chosen to perform a single permeability evaluation before the cooling experiments.

A total of fourteen experiments were conducted on the Bentheimer core. These tests varied in flow rate, pressure conditions, and boundary configurations. Particular focus is placed on experiment ex13, which served as the benchmark case due to its pronounced and clearly interpretable thermal front propagation.

5.1. Bentheimer Core Permeability

The system was configured to perform dedicated gas permeability tests. For these measurements, a mass flow controller (MFC) was installed at the inlet of the coreholder to impose a constant gas flowrate, while the inlet BPC was removed to allow uninterrupted inflow. This configuration enabled calculation of permeability using the pressure drop across each segment of the core, in combination with the known volumetric flowrate. The results can be found in Table 5.1, and the details of the procedure can be found in Appendix C.2.

Table 5.1: Permeability values for the Bentheimer sandstone based on Klinkenberg correction per segment.

Sensor	Permeability (m^2)	Permeability (Darcy)
dP1	2.13×10^{-12}	2.16
dP2	1.82×10^{-12}	1.84
dP3	1.69×10^{-12}	1.71
dP4	1.40×10^{-12}	1.42
dP5	1.27×10^{-12}	1.29
dP6	1.05×10^{-12}	1.06

The resulting intrinsic permeability values align well with the literature ranges for Bentheimer sandstone (Peksa et al., 2015).

5.2. Overview of Joule Thomson Experiments

Table 5.2 summarizes the key parameters of each experiment, including flow conditions, experiment duration, and cooling intensity. A more detailed table where the BPC, BPR, pump pressure used and the goal of the experiment are listed in the Appendix D.4. Graphs per experiment are shown in Appendix D.6, where the temperature, pressure, and pressure difference graphs of the sensors will be shown together. For completion, the pump graphs will also be included along the experimental plots, demonstrating the stability of the pressure. Using both the pressure from the pump and the system, the pressure drop from the inlet back pressure cartridge can be calculated as well.

Table 5.2: Summary of Bentheimer Joule-Thomson cooling experiments.

Experiment	Flow mL/min CO_2(l)	BPR bar	Duration hh:mm	Min T °C	Injected Volume mL CO_2(l)
ex1	5.0	38.2	01:40	7.04	506.6
ex2	10.0	39.7	00:29	8.50	299.5
ex3	2.5	40.0	05:00	9.49	751.2
ex4	7.5	38.0	01:01	6.40	460.5
ex5	5.0	14.8	00:46	0.94	231.8
ex6	10.0	35.4	01:01	4.33	613.7
ex7	10.0	45.8	00:21	13.67	212.3
ex8	7.5	32.5	01:02	1.75	472.2
ex8.5	9.0	32.7	00:22	2.11	202.7
ex9	10.0	35.2	00:47	3.68	478.8
ex10	8.5	34.8	01:11	4.24	610.7
ex11	12.5	36.0	01:03	5.59	791.7
ex12	5.0	35.0	03:58	8.90	1194.5
ex13	**12.5**	**25.4**	**01:08**	**-5.20**	**861.6**

The most significant result was obtained in experiment ex13, which showed the largest observed temperature drop and thermal front development as a result of numerous improvements to the setup made over time, including a different back pressure regulator, a Teflon o-ring inside the BPC, and a hotplate placed to heat the outlet BPR. The following sections will analyze only this case in depth, making references to other experiments where required.

5.3. Experiment Results

Experiment ex13, with flow parameters as described in Table 5.3, demonstrated the most pronounced cooling behavior in all Bentheimer experimental runs. It is considered the benchmark case for evaluating front propagation, cooling consistency, and thermodynamic alignment. The results will be discussed in the following sections.

5.3.1. Temperature Evolution and Sensor Response

Figure 5.1 shows the temperature profiles for ex13. The cold front propagates through the core, starting from T1, ending with T7. T4, embedded centrally within the core, recorded the lowest temperature, reaching approximately **-5.2 °C** at the end of the experiment.

The difference between Kentucky and Bentheimer in terms of temperature response is supposed to be clear; since Bentheimer has no large pressure gradient, all sensors should converge to the same temperature. Looking at the temperature graph at the top of Figure 5.1, one thing to notice is the difference in the minimum temperature reading of each sensor, where T4, and at the end of the experiment T7, show the largest response to the experiment. Although other sensors showed mild to moderate temperature drops, but they do not seem to converge to the same temperature. During the end of the experiment, liquid CO_2 can be seen exiting the core, paired with the sharp temperature drop in T7, which most likely reflects direct contact with the accumulated liquid CO_2 as T7 is external to the core and in the tube where liquid CO_2 is observed.

Thermal images confirm the same decrease in temperature as can be seen in the experiment results.

Table 5.3: Experimental parameters and observed values for benchmark test ex13.

Parameter	Value
Core material	Bentheimer sandstone
Permeability	1.2–2 Darcy (measured)
Porosity	~22% (Peksa et al., 2015)
Pore throat size	20 μm (Peksa et al., 2015)
Flow rate	12.5 mL min^{-1}
Injection pressure	90 bar
Injection temperature	20 °C
Inlet BPR cartridge	65 bar drop
Outlet pressure (BPR)	25.4 bar
Total experiment duration (hh:mm)	01:08
Total injected volume	861.6 mL
Minimum temperature (T4)	−5.2 °C
Joule-Thomson cooling power (estimated)	14.7 W

This minimum temperature at T7 is 2 degrees higher than the T4 temperature, possibly due to higher thermal losses, as the T7 sensor placement is in a metal t-coupling with large thermal losses to the surrounding. The remaining sensors appear to respond in a similar way as T4, although this is not observed. T1 is insulated by 1 mm of PEEK in the inlet cap, so the sensor is expected to give a damped (or attenuated) response, for the remaining sensors, their location was verified to differ, which caused this difference in behavior. The lack of convergence of temperature sensors will be further discussed in a detailed investigation of the problem in the Appendix A.1.

5.3.2. Pressure Dynamics

The pressure drop profile, particularly the evolution of the differential pressure (dP) as can be seen in Figure 5.1, reveals the arrival and advancement of a denser phase (liquid CO_2) within the core. A clear increase in dP is observed beginning at 4 minutes for sensor dP1, with the other sensors following in order afterwards. This corresponds to the moment when CO_2 begins to condense, leading to a progressive increase in viscous resistance. This difference in viscosity between the liquid and gaseous phase of CO_2 causes a gradual increase until the liquid front moves past the segment.

The second subsplot in the middle of Figure 5.1 presents the raw pressure data from the pressure sensors distributed along and before/after the core. The plot itself looks like a flat line, with all sensors overlapping; this is to be expected and illustrates the large difference in pressure response compared to the Kentucky core. All values remain consistently at 25.4 bars, with a slight gradient building up during injection. This phenomenon is to be expected with the pressure regulator used; the issue is also known to be slightly present in other laboratory setups, and as long as these increases are not too extreme, this is not relevant for research.

The data in Figure 5.1 is unfiltered and the noise in the signal, in particular in the differential pressure graph, comes from the effect of the pressure variation in the injection pump; as the pressure in the Vindum pump inlet was lower than the system pressure, the pump struggled to correct for this. Switching between pistons therefore caused a short decrease in the overall pressure fed to the system. Figure 5.2 displays the full pump pressure during the experiment. The system reached steady-state injection behavior after 2 minutes. The oscillation in the pump pressure can be seen in this image. The booster pressure was increased halfway through the experiment at 30 minutes, to reduce the resonance of the pressure with the resulting local minima and maxima coming closer together. The oscillation that was still there after the adjustment proved to be of no concern to the outcome of the experiment.

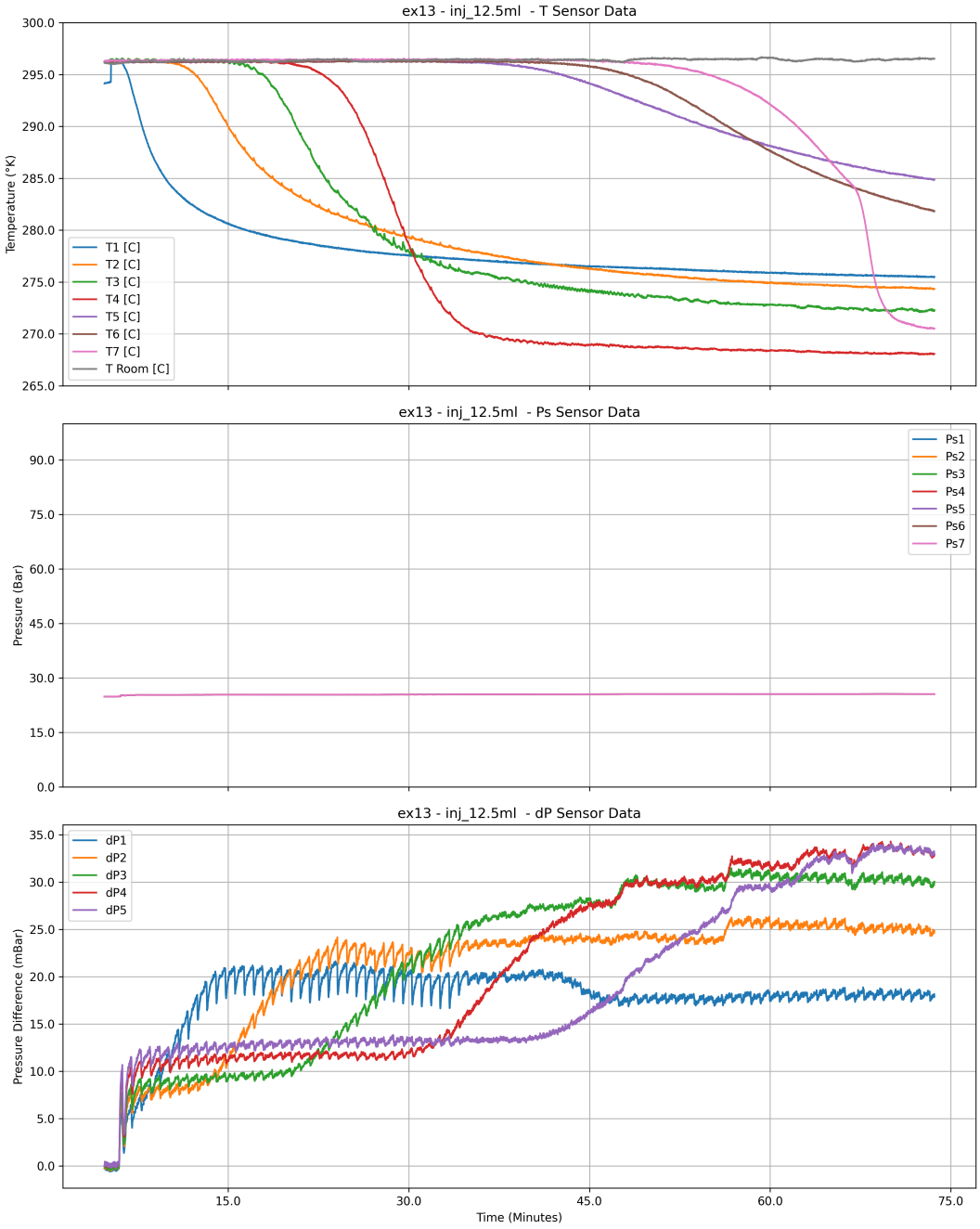

Figure 5.1: Temperature (top), pressure (middle), and differential pressure (bottom) data for ex13. Sensor T4 displays the lowest temperature, while T7 records a delayed but sudden and steep drop, due to contact with liquid CO_2.

5.3.3. Estimated Joule-Thomson Cooling Power

To evaluate the thermodynamics of this experiment, the cooling power can be calculated. This gives an indication of the amount of energy that can be extracted per unit of time, which is a direct indicator of the performance of the Joule-Thomson cooling effect.

The theoretical cooling power Q_{JT} can be estimated using the molar flow rate $\dot{n}$, the specific heat capacity C_p of CO_2, and the observed temperature drop ΔT:

$$Q_{JT} = \dot{n} \cdot C_p \cdot \Delta T, \tag{5.1}$$

where:

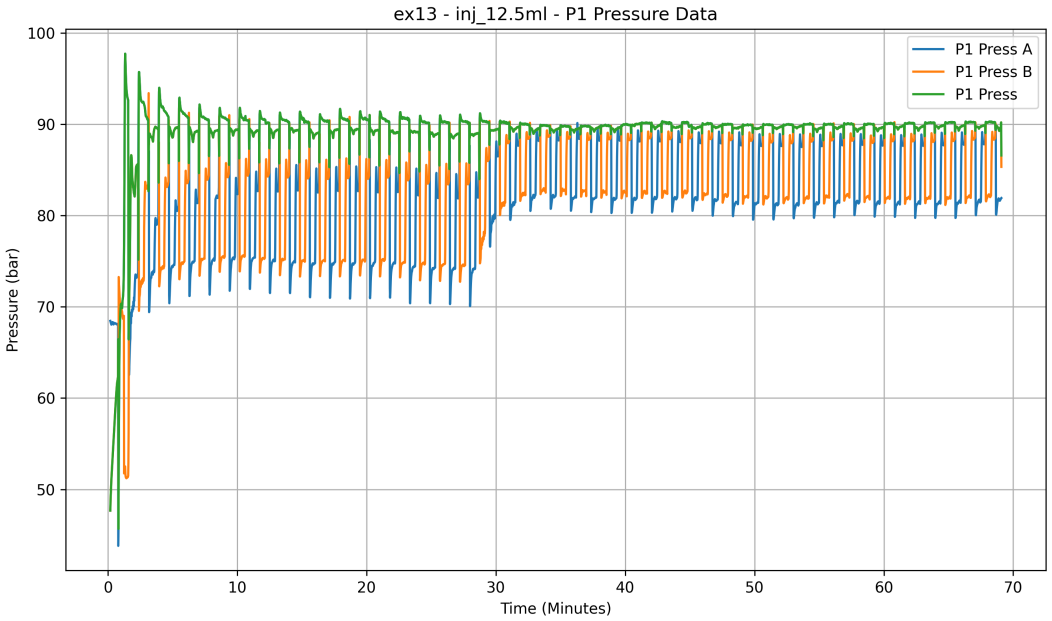

Figure 5.2: Pump pressure during ex13. The plot shows the pressure of cylinder A, B and the effective pressure going out of the pump, showing the oscillations caused by the struggle of the pump to correct for the difference in inlet and outlet pressure.

- $\dot{n} = 12.5$ mL/min of liquid $CO_2 \cdot 18.8$ mol/L $= 0.2083$ mL/s $\cdot 18.8$ mol/L $= 3.92 \times 10^{-3}$ mol/s,
- $C_p \approx 150$ J/mol·K,
- $\Delta T \approx 25$ K.

All thermophysical properties of CO_2 such as molarity, were obtained from NIST (2025). Substituting the values:

$$Q_{JT} = (3.92 \times 10^{-3}) \cdot 150 \cdot 25 = 14.7 \text{ W}. \tag{5.2}$$

Thus, the estimated instantaneous cooling power is approximately 14.7 W.

5.3.4. Thermal Mass of the System

To evaluate whether this cooling power is sufficient to cool the thermal mass of the system, this will be evaluated next. The following properties are known and used to calculate the thermal mass:

- Core volume: $V_{\text{core}} = \pi r^2 L = \pi \cdot (0.0195)^2 \cdot 0.40 \approx 4.78 \times 10^{-4}$ m^3,
- Density of dry Bentheimer: $\rho_r \approx 1975$ kg/m^3 (Orlander et al., 2018),
- Heat capacity of Bentheimer: $c_r \approx \frac{2.1 \times 10^6 \text{ J/m}^3\text{·K}}{1975 \text{ kg/m}^3} \approx 1063$ J/kg·K (Fuchs et al., 2021),
- PEEK volume: $V_{\text{PEEK}} = \pi(0.049^2 - 0.024^2) \cdot 0.40 \approx 2.29 \times 10^{-3}$ m^3,
- Density of PEEK: $\rho_{\text{PEEK}} \approx 1300$ kg/m^3 (hpp-performance, 2019),
- Heat capacity of PEEK: $c_{\text{PEEK}} \approx 2200$ J/kg·K (hpp-performance, 2019).

Assuming $\Delta T_{\text{core}} = 25$ K and $\Delta T_{\text{PEEK}} = 12.5$ K (Figure 5.3):

$$Q_{\text{removed, core}} = \rho_r \cdot V_{\text{core}} \cdot c_r \cdot \Delta T_{\text{core}} \approx 1975 \cdot 4.78 \times 10^{-4} \cdot 1063 \cdot 25 \approx 25,032 \text{ J} \tag{5.3}$$

$$Q_{\text{removed, PEEK}} = \rho_{\text{PEEK}} \cdot V_{\text{PEEK}} \cdot c_{\text{PEEK}} \cdot \Delta T_{\text{PEEK}} \approx 1300 \cdot 2.29 \times 10^{-3} \cdot 2200 \cdot 12.5 \approx 81,675 \text{ J} \tag{5.4}$$

Total thermal energy removed:

$$Q_{\text{total}} = Q_{\text{core}} + Q_{\text{PEEK}} \approx 25,032 + 81,675 = 106,707 \text{ J} \tag{5.5}$$

Cooling time at $Q_{JT} = 14.7$ W:

$$t_{\text{cool}} = \frac{Q_{\text{total}}}{Q_{JT}} = \frac{106,707}{14.7} \approx 7,257 \text{ s} \approx 2.02 \text{ hours} \tag{5.6}$$

This calculation is in the same order of magnitude as the results of the experiment. The calculation estimated the experiment to take 2 hours without thermal losses to the environment, but the actual experiment was shorter (68 minutes), taking heat exchange with the surroundings into account, the difference between the calculated and experimental duration would only increase. This difference may be due to an overestimation of some parameters, falsely assuming that the coreholder has a homogeneous 12.5 °C, or ignoring other secondary cooling phenomena, such as cooling by evaporation.

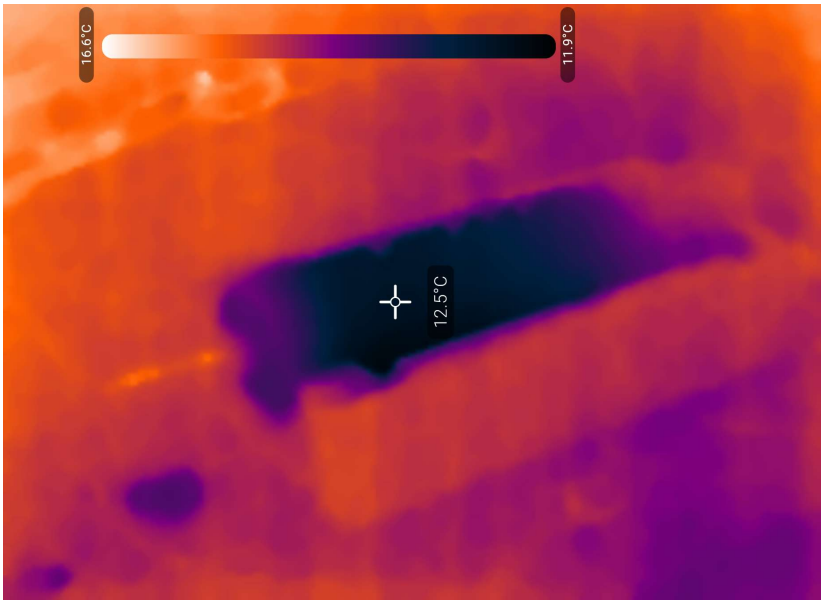

Figure 5.3: Thermal camera snapshot showing external coreholder temperature during ex13.

5.3.5. Evaporative Cooling Estimate

If a phase change occurs, an additional source of cooling could be due to the latent heat absorbed during vaporization. Assuming that partial evaporation occurred at the outlet of the core, the associated enthalpy change can be approximated.

To quantify the potential contribution of evaporative cooling due to the phase change at the outlet of the core, the latent heat of vaporization of CO_2 is taken as $\Delta H_{\text{vap}} = 16.5\,\text{kJ mol}^{-1}$. The molar density of liquid CO_2 is approximately $18\,\text{mol L}^{-1}$ (NIST, 2025). The molar flow rate $\dot{n}$ (mol/s) is calculated from the volumetric flow rate Q (mL/min) as:

$$\dot{n} = \frac{Q \cdot \rho_{\text{mol}}}{60} \tag{5.7}$$

Where Q is in mL/min of liquid CO_2, $\rho_{\text{mol}} = 18\,\text{mol L}^{-1} = 0.018\,\text{mol mL}^{-1}$, and the factor 60 converts minutes to seconds.

The cooling power is then estimated by:

$$Q_{\text{evap}} = \dot{n} \cdot \Delta H_{\text{vap}} \tag{5.8}$$

Substituting values:

- For $Q = 5\,\text{mL}\,\text{min}^{-1}$:

$$\dot{n} = \frac{5 \cdot 0.018}{60} = 0.0015\ \text{mol}\,\text{s}^{-1}, \quad Q_{\text{evap}} = 0.0015 \cdot 16500 = 24.8\,\text{W}$$

- For $Q = 7.5\,\text{mL}\,\text{min}^{-1}$:

$$\dot{n} = \frac{7.5 \cdot 0.018}{60} = 0.00225\ \text{mol}\,\text{s}^{-1}, \quad Q_{\text{evap}} = 0.00225 \cdot 16500 = 37.1\,\text{W}$$

- For $Q = 10\,\text{mL}\,\text{min}^{-1}$:

$$\dot{n} = \frac{10 \cdot 0.018}{60} = 0.0030\ \text{mol}\,\text{s}^{-1}, \quad Q_{\text{evap}} = 0.0030 \cdot 16500 = 49.5\,\text{W}$$

Table 5.4: Estimated cooling power from evaporative CO_2

Flow Rate (mL/min)	Molar Flow (mol/s)	Cooling Power (W)
5	0.0015	24.8
7.5	0.00225	37.1
10	0.0030	49.5

The presence of vaporization at the outlet, supported by the PT diagram (Figure 7.1), suggests that further temperature drops are thermodynamically limited by the onset of the phase transition. As can be seen in Table 5.4, the cooling power due to pure evaporation is significant compared to the Joule-Thomson cooling effect. As not all CO_2 evaporates, the actual power would likely be lower; however, the power of evaporative cooling appears to be around three times as potent as JT cooling.

5.3.6. Estimate of Ambient Conduction and Convection

The core is encased in a PEEK shell with a wall thickness of 25 mm, forming a cylindrical insulation layer around the core. Heat loss from the cold core to the ambient air occurs in two stages: radial conduction through the PEEK, followed by convective heat transfer from the outer surface of the PEEK to the ambient air. These two mechanisms can be modeled using the concept of thermal resistances in series.

Total Thermal Resistance

Using the model for concentric cylindrical heat transfer with outer convection (Zhou et al., 2021), the total thermal resistance R_{total} is:

$$R_{\text{total}} = \frac{\ln(r_2/r_1)}{2\pi L k_{\text{PEEK}}} + \frac{1}{2\pi r_2 L h} \tag{5.9}$$

where:

- $r_1 = 0.024\,\text{m}$: inner radius (core radius),
- $r_2 = 0.049\,\text{m}$: outer radius (PEEK outer radius),
- $L = 0.40\,\text{m}$: core length,
- $k_{\text{PEEK}} = 0.25\,\text{W}\,\text{m}^{-1}\,\text{K}^{-1}$: thermal conductivity of PEEK (hpp-performance, 2019),
- $h = 10\,\text{W}\,\text{m}^{-2}\,\text{K}^{-1}$: convective heat transfer coefficient for natural convection around cylinder (Lienhard, 2020).

Substituting:

$$R_{\text{cond}} = \frac{\ln(0.049/0.024)}{2\pi \cdot 0.40 \cdot 0.25} \approx 0.730\,\text{K}\,\text{W}^{-1},$$
$$R_{\text{conv}} = \frac{1}{2\pi \cdot 0.049 \cdot 0.40 \cdot 10} \approx 0.0813\,\text{K}\,\text{W}^{-1},$$
$$R_{\text{total}} = R_{\text{cond}} + R_{\text{conv}} \approx 0.811\,\text{K}\,\text{W}^{-1}.$$

Steady-State Heat Loss
Assuming a temperature difference $\Delta T = T_{\text{ambient}} - T_{\text{core}} = 12.5 - (-5) = 17.5\,\text{K}$:

$$Q_{\text{loss}} = \frac{\Delta T}{R_{\text{total}}} = \frac{17.5}{0.811} \approx 21.6\,\text{W} \tag{5.10}$$

This model shows a total heat loss rate of approximately 21.6 W. Although this is a simplified steady-state estimate, it provides a useful estimate.

Conclusion
Combining Joule-Thomson cooling power (14.7 W), the estimated contribution from evaporative cooling (up to 49.5 W), and ambient heat ingress through conduction (21.6 W), the net effective cooling during peak conditions is approximately:

$$Q_{\text{net}} = 14.7 + 49.5 - 21.6 \approx 42.6\,\text{W}$$

Using this net cooling power to reevaluate the cooling time for the total thermal mass of the system (106 707 J), the required time becomes:

$$t_{\text{cool}} = \frac{Q_{\text{total}}}{Q_{\text{net}}} = \frac{106707}{42.6} \approx 2504\,\text{s} \approx 42\,\text{min}$$

This result is much more closely aligned with the experimental durations (68 min). The overestimation is expected because the evaporation power is likely to be smaller and the heat transfer to the surrounding could be greater. This confirms that Joule-Thomson cooling, in the Bentheimer sandstone experiment, is not the main driving force of cooling, but evaporative effects dominate.

6

Numerical Simulation Results: DARTS

This chapter presents the results of numerical simulations conducted using DARTS. The purpose of these simulations is to assess the precision of DARTS in reproducing the thermal and hydraulic trends observed during CO_2 injection experiments. Next, the influence of numerical discretization and equation of state (EOS) sensitivity on the simulation results will be evaluated. The primary benchmark for comparison is experiment `ex17`, performed on the Kentucky sandstone core at 293 K injection temperature and a BPR of 20 bar at the outlet.

Simulations replicate experimental boundary conditions and core properties with minor additional tuning. The input parameters are either gathered from calculations, like permeability, or assumed from literature (like porosity and thermal conductivity). The heat capacity required some adjustments from the values in the literature to align it with the experimental results. Where applicable, the simulated pressure and temperature profiles are compared directly with experimental measurements to identify strengths and shortcomings in the numerical approach.

Table 6.1: Simulation input parameters for DARTS model replicating experiment `ex17`.

Parameter	**Value / Description**
Core length (L)	0.40 m
Core diameter	0.039 m
Grid resolution	400–40,000 cells (1D)
Porosity (ϕ)	15.0% (AlKharraa et al., 2023)
Permeability (k)	0.375 mD (from experiments)
Injection temperature (T_{inj})	293.0 K
Injection pressure	90.0 bar
Injection rate	5 ml/min (CO_2(l))
back pressure (outlet) (p_{prod})	20.0 bar
Initial core temperature	293.0 K
EOS resolution	101–2001 OBL points
Rock heat capacity (c_r)	$\sim 830\ J/kg \cdot K$[†] (Vivas et al., 2023)
CO_2 heat capacity (c_f)	EOS-derived
Rock thermal conductivity (λ_r)	3 W/m·K (Vivas et al., 2023)
Heat loss model	None (adiabatic assumption)
Simulation time	50 min
Time step control	Adaptive (0.01–1 s)

[†] A value of 2000 J/kg·K was used in the simulations to better match the experimental thermal inertia, differing from the literature value of 830 J/kg·K.

6.1. Base Case Simulation of Experiment ex17

To reproduce the experiment `ex17`, a 1D DARTS model was configured, with all relevant core parameters extracted from laboratory logs. Table 6.1 summarizes the main input values.

Figure 6.1 compares the simulated (top) and experimental (bottom) sensor profiles. On the left, the temperature evolution along the core is shown and on the right, the corresponding pressure profiles. The comparison reveals that DARTS accurately captures the early-time cooling response, particularly the magnitude of the minimum temperature near the inlet (within ±1 K), but further down the core both the temperature and pressure start to deviate. However, the thermal rebound observed in the experiments is less pronounced in the simulation, and the simulated minimum temperature is lower than the corresponding experimental values as a result of the lower pressure in the simulated case.

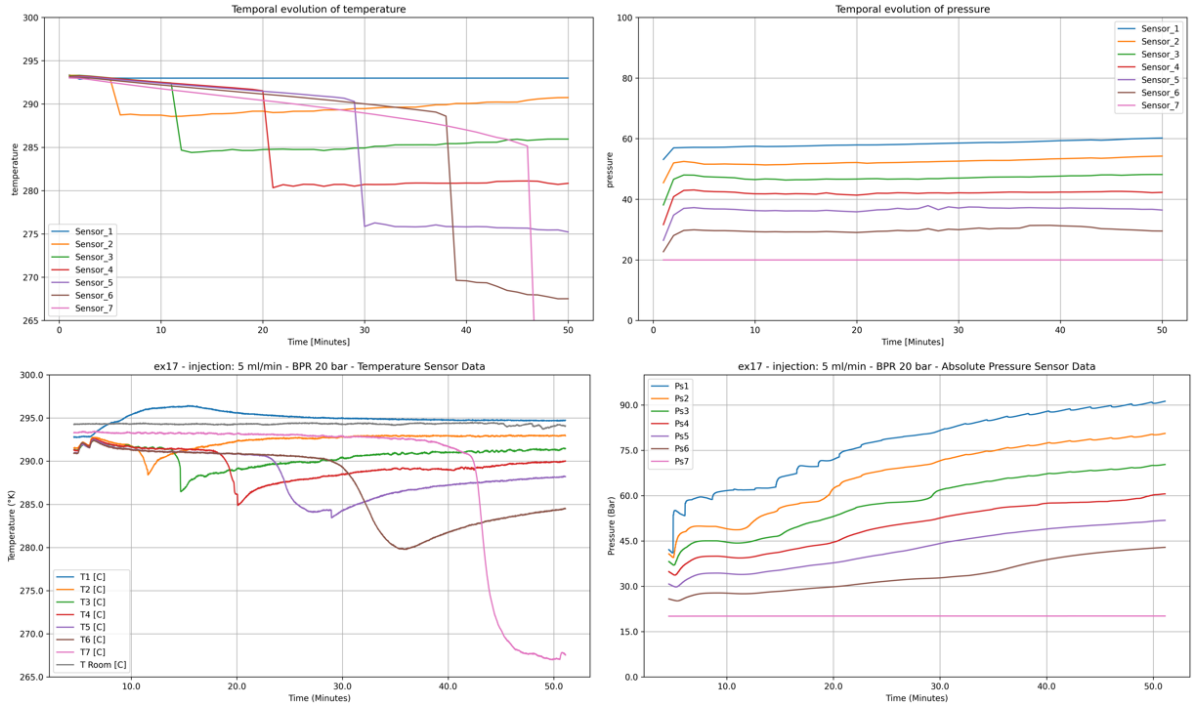

Figure 6.1: Simulated (top) vs. experimental (bottom) results for experiment `ex17`. Left: temperature profiles; Right: pressure profiles.

The gradual temperature rise observed experimentally, particularly in upstream sensors after the cold front passes, is significantly more pronounced than in the simulation. This upward creep in temperature likely results from heat conduction from the coreholder and environment, which is currently not modeled in the adiabatic simulation setup.

For the pressure response, similar overall pressures are observed between the experiment and the simulation in the initial 10 minutes, but several key differences remain. In the experimental data, pressure fluctuations are more pronounced, particularly during startup. These variations are attributed to the compressibility effect, which in turn affects the pressure response. Unlike the simulation, where the pressure field evolves smoothly from the input, sensor 1 in the experiment shows an immediate response to injection, whereas subsequent sensors exhibit progressively delayed and dampened responses. This indicates a physical pressure front propagating through the porous medium, which is not captured accurately in the DARTS model.

6.1.1. Importance of Relative Permeability

Although the simulation of the base case of the experiment `ex17` reproduces the general shape and magnitude of the JT cooling signal, a key divergence emerges in the evolution of pressure over time. The DARTS model increases to 65 bar over time. In contrast, the experimental pressure profile, especially as seen in the first 10 min shows a larger increase in pressure across all segments of the core.

This progressive pressure buildup is interpreted as a direct consequence of condensation within the porous medium. As liquid CO_2 accumulates due to temperature reduction, the relative permeability of the rock matrix is dynamically altered. This effect is particularly strong in the Kentucky sandstone core, where the low intrinsic permeability amplifies the impact of even small liquid fractions on the effective flow resistance.

Crucially, this behavior is not accurately captured in the current DARTS simulation. Although DARTS can resolve the flow of multicomponent, multiphase CO_2, it currently does not include accurate parameter inputs for the relative permeability function for the interactions of the liquid-gas CO_2 phase. As such, the simulation model assumes that both phases flow almost with equal ease, irrespective of the phase composition. This assumption leads to a relatively flattened pressure field once thermal equilibrium is reached, underestimating the experimental pressure build-up seen in Figure 6.1.

Interestingly, if we zoom in on the early phase of the experiment (first 10 min), the experimental response aligns much more closely with the full 50 min DARTS simulation data (see Figure 6.2). Both show an initial stabilization of the pressure field around 65 bar, before diverging as the experimental system begins to evolve under phase-dependent flow resistance due to the higher liquid CO_2 ratio.

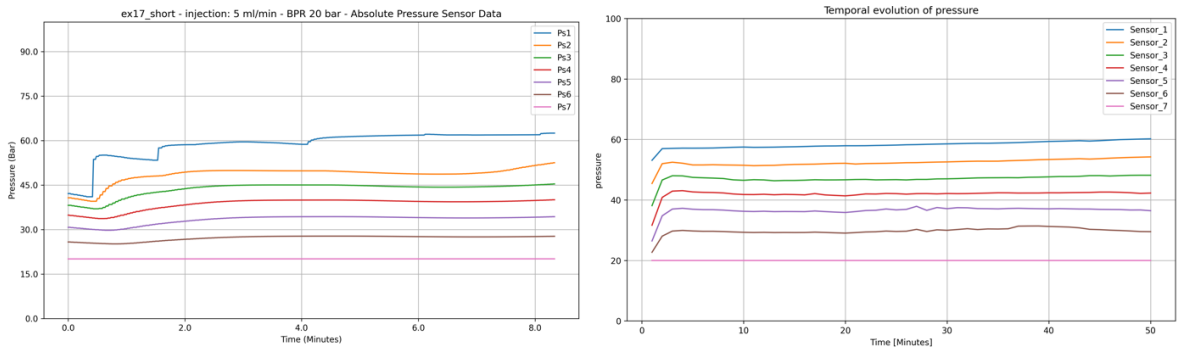

Figure 6.2: Early pressure evolution in experiment `ex17` (first 8 min) compared to the 50 min simulation result. Note that on this scale, the pressure responses are similar.

This comparison highlights the importance of incorporating phase-dependent relative permeability input parameters for the DARTS model. Without them, simulations systematically underestimate pressure build-up during JT cooling in tight rocks, reducing the model's accuracy for reservoir-scale forecasting under multiphase CO_2 injection scenarios.

6.2. Effect of Grid Resolution on Cooling Front

One of the questions in modeling JT cooling using numerical simulators such as DARTS is whether a finer spatial resolution is required to capture the steep thermal gradients and localized phase transitions that occur during CO_2 expansion. To evaluate this, a series of simulations were conducted with varying grid densities, ranging from 40 to 40,000 cells over the 40 cm length of the core. These correspond to cell sizes between 10 mm and 0.01 mm. The results are presented in Figure 6.3.

The goal of this resolution sweep was to determine whether a higher spatial discretization could better resolve the dynamics of the thermal front, particularly the sharp temperature drops found in the experimental tests. In theory, finer grids should allow an improved spatial representation of gradients in temperature, pressure, and saturation, especially where the fronts are narrow and evolve rapidly. However, contrary to expectations, the results indicate that increasing the number of grid cells has a negative effect on the accuracy of the simulation. The shape, position, and steepness of the cooling front remain largely unchanged between the 400-cell and 40,000-cell cases, but after the cooling front has passed, numerical instability seems to become active, resulting in both unexpected pressure and temperature fluctuations. For 40 cells but also for 4000 and 40000 cells, numerical errors arose, meaning 400 cells is a good resolution for this system.

This finding suggests that, under the current model configuration, namely, an adiabatic assumption without heat loss and a smooth, high-resolution equation-of-state (EOS), the thermal front is dominated

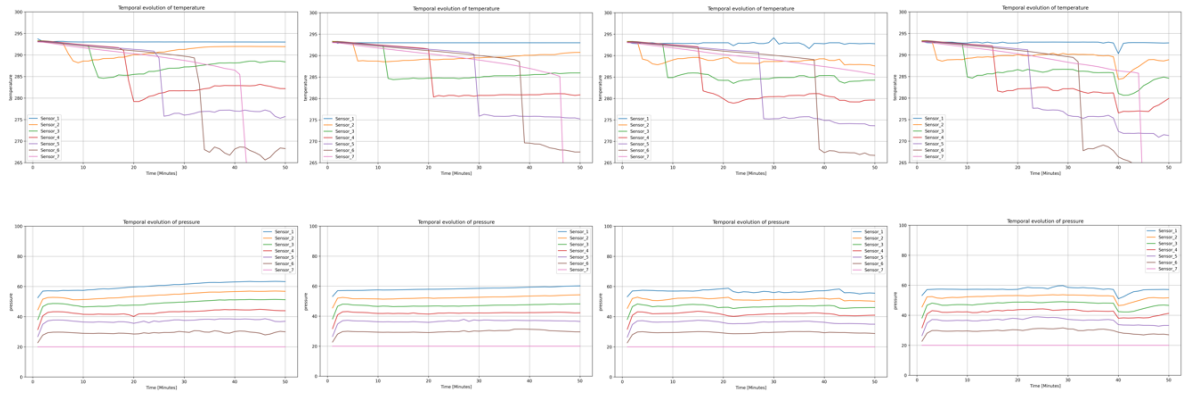

Figure 6.3: Simulated temperature profiles at low and high spatial resolutions (40 and 40,000 cells, from left to right). While the cooling front remains similar, numerical instabilities appear at very low (40 cells) and very high (4,000 and 40,000 cells) resolutions, indicating an optimal grid density is required for this problem.

more by EOS-driven thermodynamic response than by numerical diffusion or grid coarseness. As long as the underlying thermodynamic interpolations are stable and the time step is well controlled, 400 point grids appear sufficient to reproduce the cooling behavior in 1D core-scale simulations.

Importantly, this outcome has significant practical implications. Although high-resolution grids may still be warranted in scenarios with strong heterogeneities, multiphase capillary interactions, or steep permeability contrasts, they offer limited added value in homogeneous, adiabatic JT simulations. Since increasing the number of grid cells leads to a near-linear increase in computational time and memory usage, this result supports the use of moderate grid densities (e.g. 400–2000 cells) for efficient simulation without loss of physical accuracy. This becomes even more relevant when considering the scalability of the simulation framework. Extending this model to 2D or 3D geometries such as radial flow from a wellbore or complex-layered reservoirs would dramatically increase the total number of cells. For example, a 3D model with comparable axial resolution would require cells on the order of 10^7–10^8 cells, which would be expensive to run even for short simulation times. The fact that the 1D system does not require extreme grid refinement means that future extensions to multidimensional simulations can proceed with manageable computational loads, provided EOS point density remains high and numerical schemes remain stable.

6.3. EOS Resolution and Thermodynamic Smoothness

The equation-of-state (EOS) framework in DARTS provides the thermodynamic backbone of multiphase compositional simulations. It translates pressure-temperature (PT) input into corresponding physical properties, such as enthalpy, density, viscosity, and phase compositions, based on a pre-computed operator grid. This grid is constructed via the Operator-Based Linearization (OBL) approach, and its resolution is controlled through the number of interpolation points specified during the simulation setup. To evaluate how EOS resolution influences the quality and stability of the simulation output, a resolution sweep was performed using EOS tables with 101, 1001, and 5001 points. The results are shown in Figure 6.4, which shows the simulated pressure and temperature evolution for each case during a JT cooling scenario.

At the lowest resolution (101 points), the simulation exhibits pronounced artifacts in both the pressure and temperature fields. These include abrupt shifts and step-like plateaus, which originate from the coarse interpolation of enthalpy and density values between sparse EOS entries. This behavior can significantly distort thermal gradients, particularly in cases where the system operates near the CO_2 phase boundary, as is typical during CO_2 injection into the subsurface.

Increasing the resolution to 501 points smooths out many of these non-physical features. The overall thermal profile becomes more continuous and the pressure curve begins to more accurately reflect the gradual propagation of the front. However, small oscillations and residual interpolation noise still persist in some regions, especially near phase transitions, where property gradients are steep.

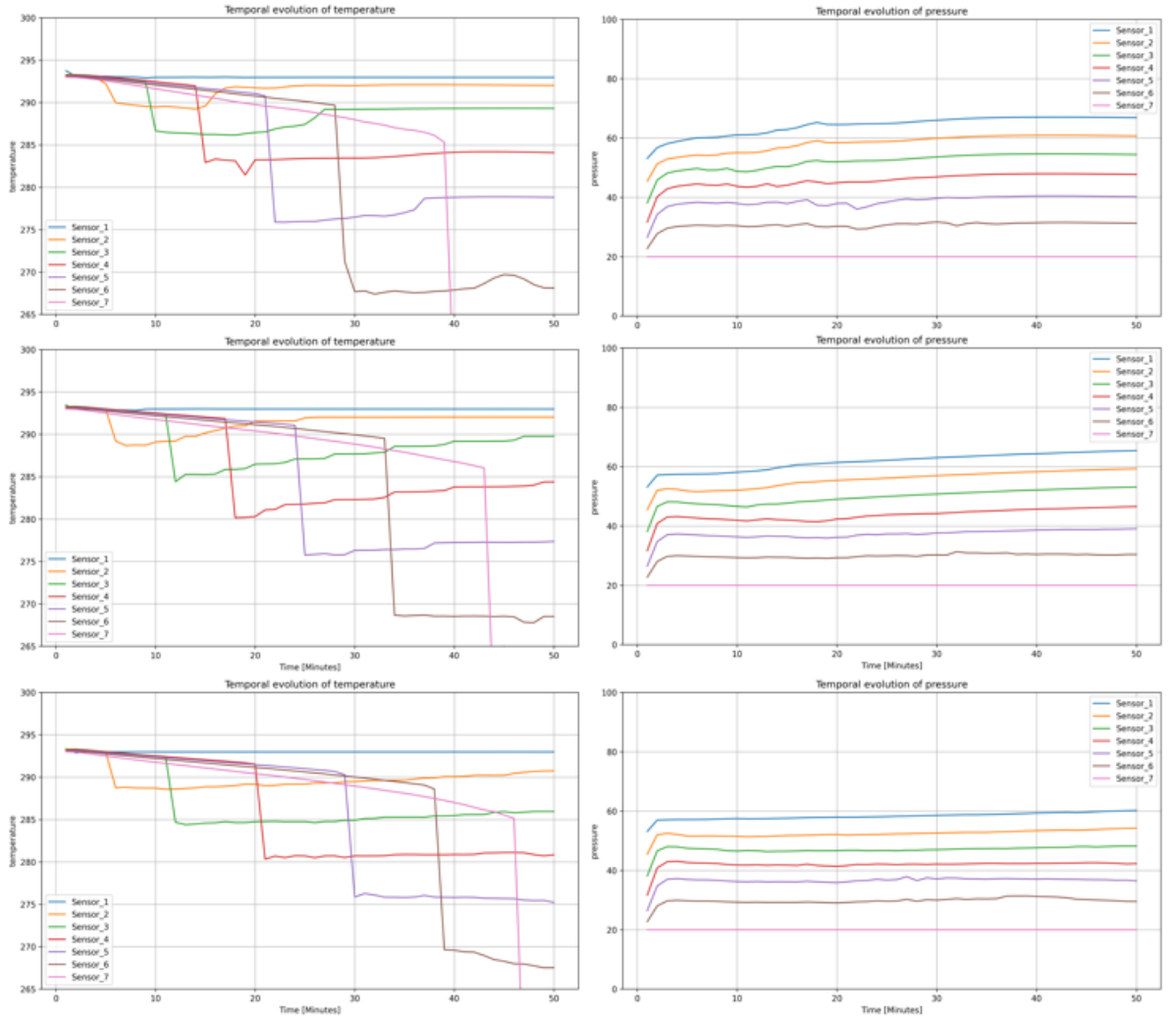

Figure 6.4: Pressure and temperature response for varying EOS resolution: 101 (top), 501 (middle), 2001 (bottom).

Only at the highest tested resolution (2001 points) does the EOS interpolation yield a thermodynamically consistent output. The temperature front is sharp, yet smooth, and the pressure response follows a physically plausible trajectory. In this configuration, enthalpy changes due to expansion and phase transition are accurately represented, and no numerical diffusion or stepwise jumps are visible.

It is important to note that increasing the EOS resolution improves not only the realism of the temperature predictions, but also the accuracy of the derived flow properties, such as effective viscosity and fluid density. These directly influence pressure build-up, front velocity, and saturation profiles. However, the gain in accuracy comes at the cost of computational overhead: Higher resolution tables significantly increase memory usage and lookup time during the simulation.

The correlation between EOS resolution and cooling intensity is particularly important. As seen in Figure 6.4, simulations using finer EOS tables predict deeper minimum temperatures, approaching the experimentally observed values. This underscores the importance of high-resolution EOS when modeling CO_2 expansion in porous media, where enthalpy gradients and latent heat release dominate energy redistribution, if the computational cost increase proves to be acceptable.

In conclusion, the number of interpolation points used in the EOS operator grid acts as a key tuning parameter for the accuracy of the simulation. For JT cooling simulations involving liquid–gas transitions of CO_2, EOS resolutions of at least 500 points are recommended. Where computationally feasible, 2000-point tables provide the best match to experimental behavior and minimize interpolation-induced

artifacts, particularly near critical phase boundaries.

6.4. Simulation With Initial Water Saturation

To investigate the impact of multiphase occupancy on thermal and pressure evolution during CO_2 injection, a DARTS simulation was performed with an initial water saturation (S_w) of 90 %. Although actual experiments were carried out under dry conditions, the introduction of water as a pseudo-phase provides a valuable proxy to represent accumulations of liquid CO_2 and the associated permeability restrictions. Water acts as an incompressible component, displacing gas and reducing the effective permeability of the porous system, mimicking the dynamic behavior expected when condensed CO_2 forms during JT cooling.

Figure 6.5 shows the temporal evolution of temperature throughout the core. Compared with the "dry" simulation, this case shows significantly improved agreement with the experimental data. As in the experiment, the cooling front advances through the core with sharper gradients and more realistic magnitudes.

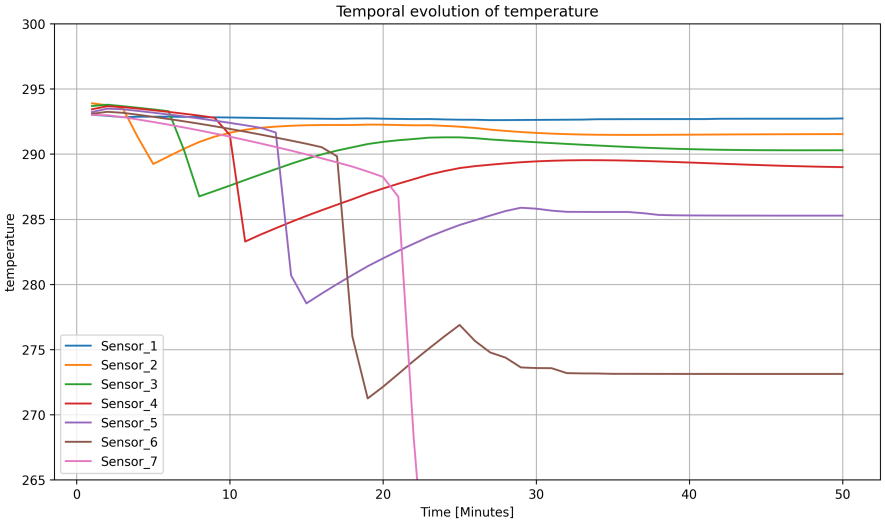

Figure 6.5: Simulated temperature evolution for 90 % initial water saturation.

The pressure response in Figure 6.6 now mirrors the experiment more closely than before. A clear and sustained pressure increase is observed throughout the core, driven by the displacement of the incompressible water phase. The accumulation is gradually increasing per segment and is continuous, as in the laboratory data. Compared to the relatively flat-pressure profile seen in "dry" DARTS simulations, this case provides a much more faithful representation of the experimental data.

The evolution of (S_w) itself is shown in Figure 6.7. CO_2 injection causes a sharp displacement front that sweeps through the core, pushing the initial water phase toward the outlet. Saturation values fall from 90 % to a residual level around 40 %, indicating clear phase separation and invasion dynamics. The nonlinear progression of pressure resembles the behavior observed during the condensation of liquid CO_2, supporting the use of water as a proxy for immobile secondary phases in this context.

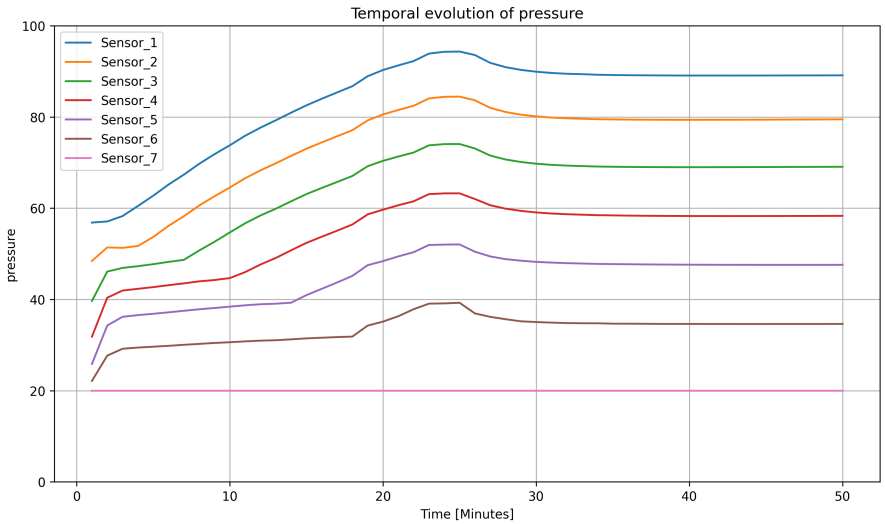

Figure 6.6: Simulated pressure evolution for 90 % water saturation. A strong resemblance to experimental pressure buildup is observed.

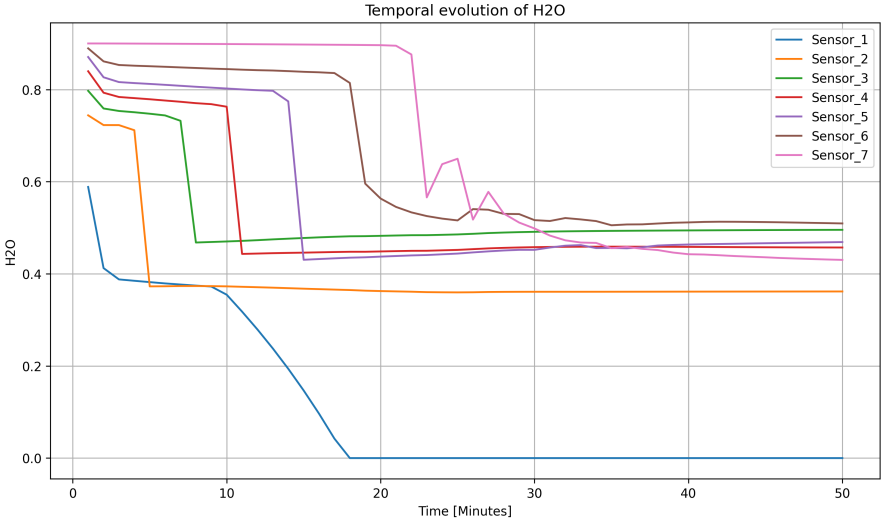

Figure 6.7: Temporal evolution of water saturation. A sharp displacement front forms, reducing water content to residual levels and restoring gas flow.

6.5. Scaling Up: Large-Scale Simulation of Joule-Thomson Cooling

To evaluate whether the Joule–Thomson cooling effect observed in core-scale experiments remains relevant at the reservoir scale, a larger DARTS simulation was configured. The length, permeability, and injection time are all multiplied by 1000, representing a simplified segment of an analog high-permeability reservoir. This allows us to assess whether similar thermodynamic behavior—including in-core cooling and pressure evolution—occurs at field-representative distances. The input parameters can be seen in Table 6.2.

Figures 6.8 and 6.9 show the evolution of temperature and pressure over time at multiple sensor positions. Although absolute cooling and pressure drops occur over longer distances and timescales than in the Kentucky core, the same thermodynamic signatures are clearly visible. An advancing thermal front, with increasing cooling depth further away from the inlet and gradual pressure build-up propagating through the core as the injected fluid displaces native gas.

This result confirms that Joule-Thomson cooling is not limited to laboratory-scale systems: under the right thermodynamic and flow conditions, the same coupled pressure–temperature evolution can

Table 6.2: Input parameters for large-scale Joule-Thomson cooling simulation

Parameter	Value / Description
Core length	400 m
Grid resolution	400 cells (1 m per cell)
Permeability	375 mD
EOS resolution	2001 points
Simulation time	34.7 days
Injection rate	5 mL/min
Initial pressure and temperature	20 bar, 293 K
Boundary conditions	Identical to Kentucky `ex17` base case

emerge in field-scale scenarios. Although propagation is more gradual and spatial extent is larger, the governing phenomena remain intact.

This simulation is intended as a proof of concept rather than a detailed reservoir model. For accurate field-scale predictions, further refinement would be necessary, including improved boundary conditions, radial geometry, heat loss integration, heterogeneity, and incorporation of an optimized relative permeability. For example, a simple 1 D model is used for scale-up, but a radial model would benefit greatly in terms of improving the results, as the flow is spread over an ever increasing area, the local flowrate and pressure gradient will decline, altering the idealized results given in this example significantly. However, these results establish an example case that bridges laboratory observations with practical CO_2 storage contexts, and offer a stepping stone for future work in upscaled Joule-Thomson modeling.

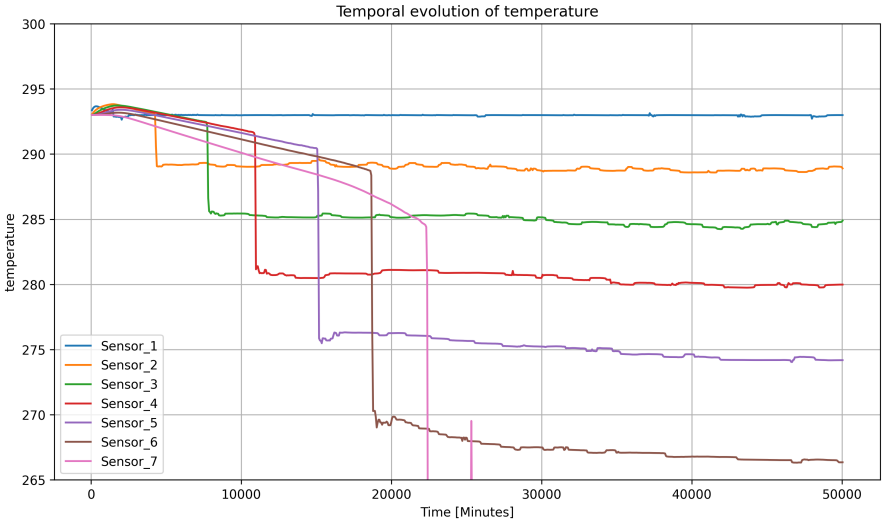

Figure 6.8: Simulated temperature evolution for a 400 m core with high permeability. The same cooling front observed at core scale is present, scaled over a longer distance.

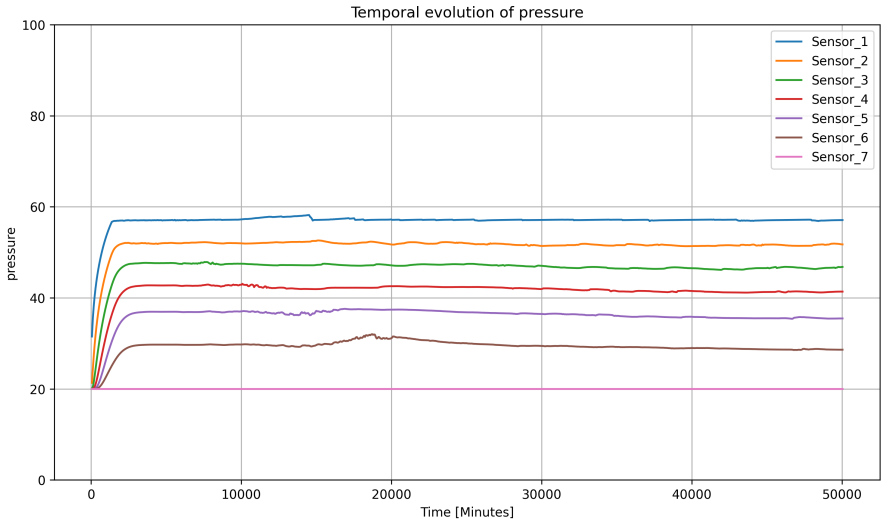

Figure 6.9: Simulated pressure evolution in the 400 m domain. The trends mirror those from core-scale ex17, but occur over a longer timescale due to the larger volume.

7

Phase Boundary in bulk versus in porous media

7.1. Phase boundary interactions

One of the key objectives of this thesis is to evaluate whether Joule-Thomson (JT) cooling in porous media can be predicted using bulk-phase thermodynamic data or whether pore-scale effects introduce measurable deviations. The appearance of phase boundary offsets, where the transition of CO_2 to the gas phase takes place at temperatures that diverge from those predicted by the bulk behavior, are of interest in this chapter. Such deviations may affect the prediction of hydrate formation, thermal front development, and injectivity in CCS scenarios.

Experimental observations support the presence of a phase change. During multiple runs, boiling CO_2 was visibly present in the transparent tube at the outlet of the core, at low recorded temperatures and under controlled BPR conditions. This indicates that vaporization occurred within the porous matrix, governed by the phase boundary of CO_2.

The progression and magnitude of cooling in both the Bentheimer and Kentucky sandstone cores consistently suggest that local thermodynamic conditions approach the CO_2 vapor–liquid phase boundary. Determining the pressure and temperature at which the minimum values occur enables an assessment of whether the cooling is capped by phase transition and whether the phase conditions exhibit confinement-induced shifts relative to the bulk data.

To quantify this relationship, the experimental results were compared with pressure–temperature (PT) and pressure–enthalpy (PH) phase diagrams generated using DARTS-Flash and thermophysical data from NIST (2025). The minimum temperatures recorded in each core segment were plotted against the corresponding local pressures, and least-squares regression was applied to fit empirical phase boundaries and identify potential deviations from bulk behavior.

7.2. Thermodynamic Diagrams and Cooling Regimes

Figure 7.1 shows the thermodynamic context in which Joule-Thomson cooling occurs. This figure is obtained with DARTS-flash. The cooling trajectory is constrained by the phase boundary of CO_2, and the maximum drop in enthalpy (cooling power) is observed when the injection path crosses the phase boundary.

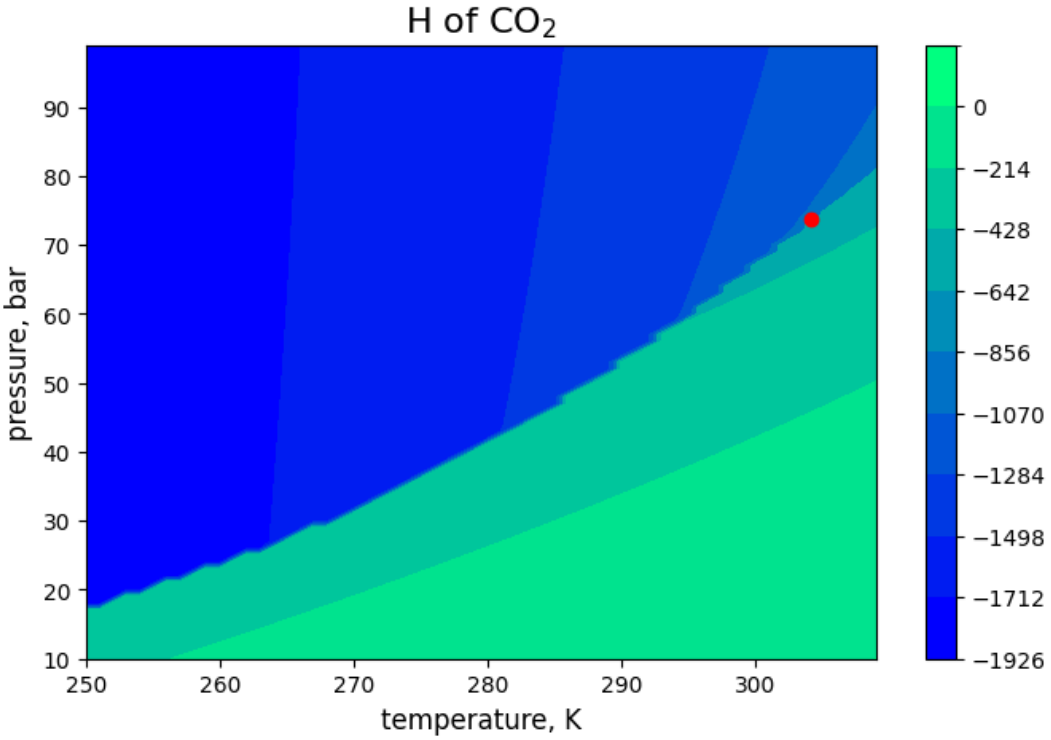

Figure 7.1: Pressure–enthalpy profile from DARTS-Flash. The phase boundary is used to determine the theoretical cooling bounds. The red dot indicates the critical point of CO_2. The green segments globally represents the gas phase and blue the liquid phase of CO_2.

7.2.1. Joule-Thomson Coefficient as Cooling Driver

Figure 7.2 shows the Joule-Thomson coefficient μ_{JT} of CO_2 as a function of pressure under four different isothermal conditions, calculated using DARTS-Flash. Experimental data from NIST (2025) are also included for comparison as data points.

The μ_{JT} coefficient quantifies the temperature change during isenthalpic expansion. Positive values indicate cooling. As shown, the coefficient increases sharply when CO_2 is in the gas phase near the boundary of the vapor-liquid phase. This is particularly clear at 250 K, where the onset of significant cooling coincides with the pressure at which CO_2 enters the gas phase. For higher temperatures, this onset shifts to higher pressures, reflecting the shift in the phase boundary.

This figure illustrates a central principle: to observe strong JT cooling, CO_2 must be fully in the gas phase or at the gas–liquid boundary. In the liquid phase, μ_{JT} remains low and cooling is negligible. Therefore, experimental conditions must be selected such that the pressure and temperature trajectory passes near the phase boundary to access the region of high μ_{JT} and thus maximize measurable cooling.

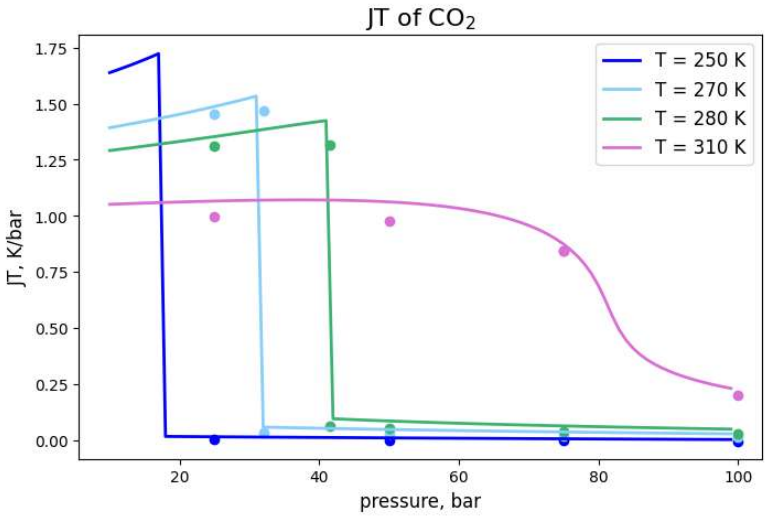

Figure 7.2: Joule-Thomson coefficient μ_{JT} of CO_2 as a function of pressure, showing strong cooling potential near 250 K and weakening below the saturation line. Calculated using DARTS-flash, with datapoints from NIST (2025) included for verification.

7.3. Phase boundary offset: Kentucky core (per-sensor)

Due to the low permeability of the Kentucky sandstone and the strong pressure gradient across the core, a per-sensor analysis was required for this series of tests. For experiments ex17, ex18, and ex19, the minimum temperature and corresponding pressure were recorded for the sensors T2 to T5. T1 and T7 are only used as an indication, as the position is less ideal compared to T2-T5 due to the PEEK insulation (T1) and confined in a metal T-coupling outside the core (T7).

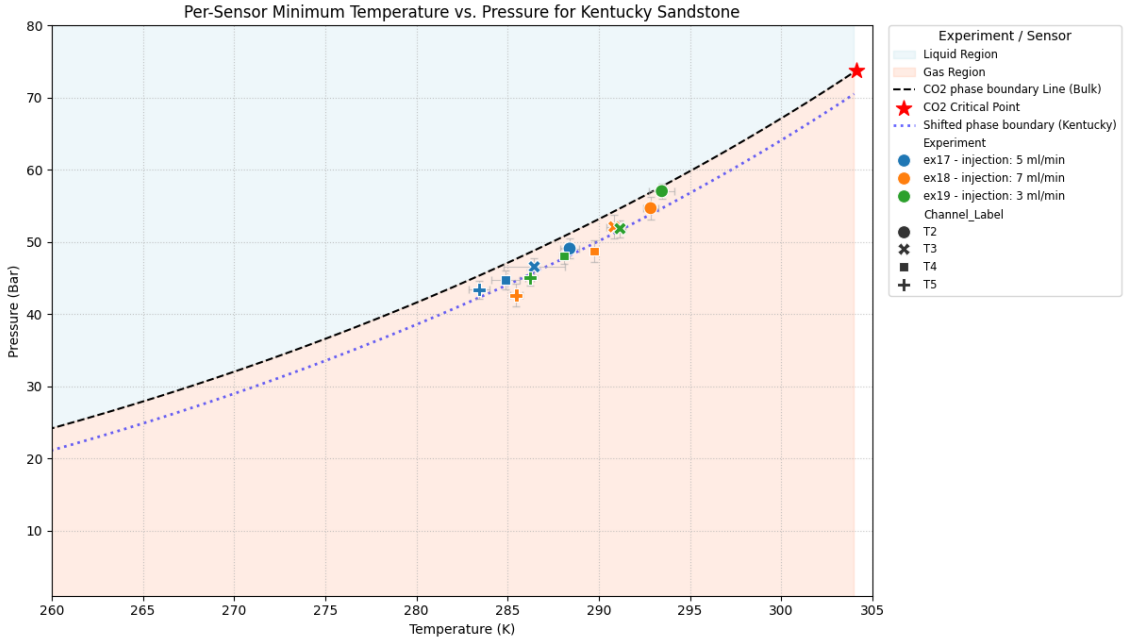

Figure 7.3: Kentucky core: per-sensor minimum temperature vs. pressure. Offset relative to the phase boundary again indicates confinement effects.

Observed phase boundary Offset

Fitting a phase boundary to this data gave:

$$\Delta P_{\text{offset, Kentucky}} = -3.18 \text{ bar} \quad \Delta T_{\text{offset, Kentucky}} = 2.3\,^{\circ}\text{C}$$

The temperature and pressure offsets relative to the CO_2 phase boundary are valid and interdependent metrics. The choice of reference depends on the framework of the analysis: a downward pressure shift or a leftward temperature shift. In this case, the observed phase transition occurs at a pressure 3.18 bar lower than expected, or equivalently, at a temperature 2.3°C higher than predicted by bulk-phase thermodynamics.

7.4. Phase Boundary Offset: Bentheimer Core (Per-Experiment)

For the Bentheimer series, the higher permeability and lower pressure gradient allowed only for a single datapoint per experiment. The minimum recorded temperature was paired with the average pressure at the corresponding sensor location, evaluated over a ±5 s window around the minimum temperature to account for thermal response delay and fluctuation of pressure.

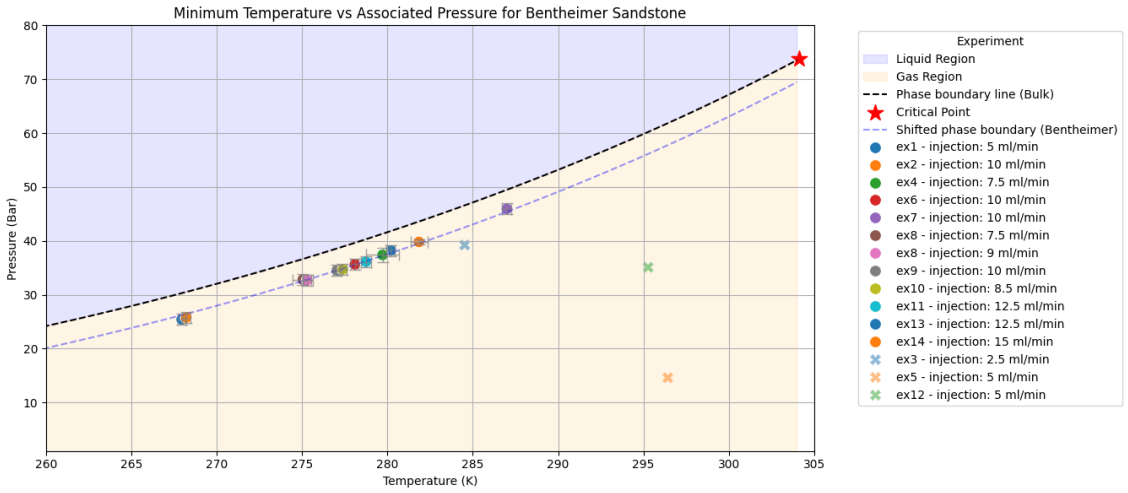

Figure 7.4: Bentheimer core: per-experiment minimum temperature vs. pressure. Consistent offset from the phase boundary indicates moderate confinement effects.

Observed Phase Boundary Offset

Fitting a saturation envelope to the (P, T_{min}) data yielded the following:

$$\Delta P_{\text{offset, Bentheimer}} = -4.10 \text{ bar} \quad \Delta T_{\text{offset, Bentheimer}} = 3.0\,^{\circ}\text{C}$$

As with the Kentucky core, both temperature and pressure offsets are presented to facilitate comparison. In this case, the phase transition occurs at a pressure 4.10 bar lower than predicted, or at a temperature 3.0° C above the value of the bulk phase. The offset is attributed to the effects of confinement and capillarity in the porous matrix.

For three of the experiments (ex3, ex5 and ex12) the collected data points seem to deviate from both the bulk and shifted phase boundary. This is because these experiments were not completed and the maximum cooling possible was not observed.

7.5. On the Relevance and Limitations of the Gibbs-Thomson Effect

The observed phase boundary offset was initially attributed to the Gibbs–Thomson effect, a classical framework that describes phase suppression, or delayed phase transitions in confined geometries. However, a quantitative evaluation reveals that this model does not accurately predict either the magnitude or direction of the offset observed in these experiments. An example calculation is included to illustrate the discrepancy. This suggests that while confinement probably contributes to the offset, it is not the sole governing mechanism. Given the absence of a consistent correlation, the precise origin of the observed deviation remains unresolved at this moment.

7.5.1. Gibbs-Thomson Effect

The Gibbs-Thomson effect describes the shift in phase equilibrium conditions (such as melting, condensation, or hydrate formation) due to the curvature of an interface or confinement within small geometries. In essence, it reflects the influence of surface energy on the thermodynamic stability of phases. This effect becomes especially pronounced in nanoscale systems or porous materials where the characteristic pore size approaches the molecular scale, as described in Equation 2.6.

In the context of this thesis, the Gibbs-Thomson effect is invoked to explain the observed deviations between the bulk CO_2 phase behavior and that measured within a porous rock matrix during JT driven cooling. Experimental data consistently show that the onset of phase change, such as gas-liquid condensation, occurs at lower temperatures than predicted by bulk equilibrium curves.

A preliminary estimate of the saturation shift was made applying the Gibbs-Thomson framework using a representative pore size from other studies, while assuming constant values for other parameters such as interfacial tension and contact angle. This approximation was motivated by practical limitations: accurate in situ measurement of all contributing variables is infeasible, and the experimental timeline did not permit full parametric exploration. Some values are therefore assumed from the literature, or for example the contact angle, and the maximum value is taken to evaluate the upper bound of the influence of the Gibbs-Thomson effect.

Using typical values to evaluate the magnitude of the effect:

- $\sigma_{lv} \approx 0.0125\ \mathrm{J/m^2}$ (Mulero et al., 2012)
- $\rho \approx 800 kg/mol$(NIST, 2025)
- $\Delta H_{\mathrm{vap}} \approx 16.4 \times 10^3\ \mathrm{J/mol}$ (NIST, 2025)
- $\cos\theta \approx 1$ (assuming $\theta = 0°$ as an upper bound)
- $r \approx 20\ \mu$m for Bentheimer, 1.5 μm for Kentucky

Assuming these values, the corresponding temperature offset is approximately 0.0023 °C for Bentheimer and 0.031 °C for Kentucky sandstone, respectively.

Even for the smallest estimated pore sizes. This is orders of magnitude too small to explain the empirically observed shifts of several degrees Kelvin, unless pores are at the nanometer scale, which is not the case here.

Furthermore, the direction of the predicted shift conflicts with experimental results: the Gibbs-Thomson effect implies that the phase transition should occur at *higher* pressures in smaller pores, yet Kentucky, having the tighter pore system, exhibits a *smaller* offset in the experimental findings.

This concludes that the Gibbs-Thomson equation is not the driving force for this offset, and other possibilities need to be explored further.

7.5.2. The Kelvin Equation

The Kelvin equation, which describes capillary condensation and predicts a shift in equilibrium vapor pressure due to surface curvature, was also evaluated based on these findings:

$$\ln\left(\frac{P}{P_0}\right) = -\frac{2\gamma V_m}{rRT}, \tag{7.1}$$

where γ is the liquid–vapor surface tension of CO_2, P_0 the bulk saturation pressure, P the equilibrium pressure in a curved pore, R the gas constant and T the absolute temperature.

Using:

- $\gamma \approx 0.0125\ \mathrm{J/m^2}$,
- $R = 8.314\ \mathrm{J/(mol \cdot K)}$,
- $T = 293\ \mathrm{K}$,
- $V_m = 5.5230 \times 10^{-5}\ \mathrm{m^3/mol}$,
- $r = 100\ \mathrm{nm} = 1 \times 10^{-7}\ \mathrm{m}$,

we obtain:

$$\ln\left(\frac{P}{P_0}\right) = -\frac{2 \cdot 0.0125 \cdot 5.5230 \times 10^{-5}}{1 \times 10^{-7} \cdot 8.314 \cdot 293} \approx -0.0565,$$

implying $P/P_0 \approx e^{-0.0565} \approx 0.945$, or a pressure depression of about 5.5% relative to the bulk pressure. For $P_0 = 30$ bar, this corresponds to an offset of approximately 1.65 bar.

However, such a result requires nanopore-scale confinement ($r \leq 100$ nm), which is inconsistent with the known pore size distribution in Bentheimer and Kentucky sandstones. Bentheimer, in particular, has pore radii on the order of 10–50 μm, which would yield < 0.1 bar shifts. Thus, neither Gibbs–Thomson nor Kelvin effects at realistic pore sizes can fully explain the magnitude or reversed trend of the observed phase boundary offset.

Recent studies indicate that CO_2 adsorption on mineral surfaces can dynamically alter the contact angle of the CO_2–brine–mineral system, thereby affecting capillary behavior and phase transition dynamics. Jones et al. (2022) demonstrated that changes in wettability, especially under the influence of surfactants or surface-active interactions, can significantly change the effective capillary pressure and therefore modify the phase envelope. Although the experiments in this thesis excluded water or surfactants, the underlying mechanism remains applicable: adsorption-induced changes in interfacial energy directly affect local phase stability conditions. In addition to altering wettability, adsorption of CO_2 is an exothermic process that releases heat, in the order of 20–25 kJ/mol as reported by Zhang et al. (2016), which can locally counteract cooling from Joule–Thomson expansion. This dual effect of adsorption, through both thermal buffering and contact angle modification, introduces non-trivial shifts in phase-transition behavior within porous media, complicating any straightforward application of bulk phase diagrams.

7.6. Validation with Experimental P−T Diagram using DARTS

The DARTS simulation results align with the initial expectations based on the bulk thermodynamic predictions: specifically, no apparent offset from the phase boundary is observed. This agreement holds under the assumption that a sufficiently high resolution equation-of-state (EOS) table is used to capture the thermodynamic behavior of CO_2 near the phase transition. With a relatively low EOS resolution, offsets of around 1.5 bar or 1 K can be expected. By increasing this to a high-resolution model, this error can be decreased to 0.1 bar, or 0.07 K. Interesting to note; the offset in this case is **above** the bulk phase line, while the experimental results are all **below** the bulk phase boundary.

However, the accuracy of this result depends not only on EOS resolution, but also on a wide range of additional factors. Both numerical simplifications and an incomplete understanding of the physical processes can introduce discrepancies.

8

Discussion

In this discussion, theoretical interpretations are proposed, unresolved phenomena are revisited, and implications for larger CO_2 injection processes are considered. These reflections aim not only to account for the discrepancies observed in the data but also to provide a basis for future hypotheses, experimental directions, and model refinements.

8.1. Deconvolution of Cooling Mechanisms: Permeability as a First-Order Control

The experimental campaign successfully isolated two distinct thermal transport regimes, revealing that reservoir permeability is a first-order control of the dominant cooling mechanism.

In the low-permeability Kentucky sandstone (0.37 mD), cooling was a continuous isenthalpic expansion process throughout the pressure gradient of the core, as detailed in Chapter 4. This was evidenced by the spatially dependent temperature minima, where sensors closer to the low-pressure outlet recorded progressively colder temperatures. The continuous pressure build-up observed during these experiments is a direct hydraulic consequence of multiphase flow; as liquid CO_2 formed within the pore space, it impeded the flow of the gas phase, increasing the overall flow resistance. This highlights the strong coupling between thermal evolution and hydraulic response in tight formations. Furthermore, these experiments revealed a clear trade-off: Higher flow rates were necessary to overcome ambient heat gain but introduced measurement instabilities and compressional heating at the inlet, while lower flow rates improved observational accuracy, but were more vulnerable to thermal losses.

In contrast, high-permeability Bentheimer sandstone (1–2 Darcy) exhibited a negligible internal pressure gradient. Here, cooling was initiated by a large synthetic pressure drop at the inlet BPC, causing the liquid CO_2 to "flash" into a two-phase mixture. The subsequent thermal evolution within the core was not driven by further expansion, but by the advection of this cold, two-phase front. The dominant cooling mechanism was the absorption of latent heat during the evaporation of liquid CO_2. The energy balance calculation (Section 5.3.3) confirms this, showing that the potential cooling power of evaporation (up to 49.5 W) far exceeds that of the isenthalpic expansion (14.7 W). This explains a key finding from the Bentheimer series: The final temperature was dictated by the outlet pressure (the BPR setting), not by the magnitude of the inlet pressure drop or the flow rate.

This fundamental difference confirms that in high-permeability reservoirs, near-wellbore cooling may be dominated by phase-change effects in a distinct zone, while in low-permeability reservoirs, cooling is a more distributed process governed by the pressure gradient within the rock matrix itself.

8.2. The Phase Boundary Anomaly in Porous Media

A key finding of this research is the systematic deviation of the observed CO_2 phase transition from the bulk thermodynamic boundary. In both rock types, the onset of condensation occurred at pressures 3–4 bar lower (or temperatures 2–3 K higher) than predicted by standard phase diagrams.

The quantitative analysis in Chapter 7 confirmed that classical confinement theories are insufficient to explain this offset. The Gibbs-Thomson and Kelvin effects, which depend on the radius of the pores, predict shifts of less than 0.1 K and 0.1 bar, respectively, for the micrometer-scale pores of these sandstones. Furthermore, these theories predict a greater shift for smaller pores, yet the tighter Kentucky core exhibited a smaller offset than the Bentheimer core.

This discrepancy suggests that the observed offset arises from a more complex interplay of phenomena not captured by equilibrium thermodynamics. The most likely contributors include:

- **Non-Equilibrium Kinetics:** The rapid expansion during the experiments may not allow enough time for the system to equilibrate. The fluid could exist in a metastable, undercooled state before nucleation and phase change occurred, thus shifting the observed P-T point.
- **Adsorption Effects:** The adsorption of CO_2 on mineral surfaces is an exothermic process that releases heat (Zhang et al., 2016). This localized heating could counteract JT cooling, requiring a larger pressure drop (and thus a lower P-T state) to initiate net condensation. This effect would be more pronounced in the illite-rich Kentucky sandstone, potentially explaining its smaller net offset compared to the quartz-dominant Bentheimer.
- **Measurement Artifacts:** As detailed in Appendix A.1, inconsistencies in thermocouple placement and thermal contact, particularly in the early Bentheimer tests, remain a contributing factor. The dead volume in the pressure tubing of the low-flow Kentucky experiments may also have caused a lag in the pressure readings, which affected the precise P-T data used to quantify the offset.

The true mechanism is likely a combination of these factors. This finding is significant because it implies that predictive models cannot rely solely on bulk phase diagrams and must incorporate rock-specific, pore-scale physics.

8.3. Heat Exchange Dynamics: Transient vs. Steady-State Models

Understanding the thermal evolution of CO_2 during injection is central to interpreting Joule–Thomson cooling behavior in porous media. In this study, two contrasting models for heat transfer were evaluated: a *steady-state balance model* and a *transitory delay front model*.

- The **steady-state model** (Chesnokov et al., 2024) assumes that Joule-Thomson cooling is continuously offset by the influx of conductive heat from the surrounding rock matrix. As a result, temperature minima remain shallow and stationary in space, particularly under low injection rates and prolonged operation.
- The **transient delayed-front model** (Chesnokov et al., 2025), on the contrary, accounts for the finite thermal diffusivity of the rock. In this case, heat inflow lags behind the advancing pressure and enthalpy fronts, resulting in a propagating cooling wave. This delay allows localized undercooling and can produce multiple temperature minima over time, especially under rapid injection or in formations with poor thermal coupling.

Our experimental data consistently support the transient model. In the Bentheimer core, a critical injection rate threshold of approximately 6 mL/min was identified. Below this threshold, Joule-Thomson cooling was quickly overwhelmed by conductive heating from the surrounding environment, leaning more towards the steady-state model. Above it, sustained cooling was observed, with the temperature decreasing progressively throughout injection, indicative of thermal inertia and delayed equilibration.

8.4. Implications for CCS Operations and Hydrate Risk

Although these experiments excluded water, our pressure-temperature (PT) minima clearly enter hydrate stability zones. For example, hydrate formation can begin around conditions as moderate as 275 K and 20 bar. Considering that JT cooling within our experiments reached temperatures as low as 265 K, the practical risk of hydrate formation is significantly increased in field scenarios involving water-bearing reservoirs. Hydrate plugs that form near the injection well could substantially reduce the injectivity of the reservoir, impede the effective storage of CO_2, and pose significant operational challenges. Moreover, the formation of hydrates can lead to a build-up of pressure behind these plugs, potentially affecting the integrity and safety of the well.

Practical recommendations to mitigate hydrate risks during CCS operations include:

- **Maintain injection flow rates below identified thermal thresholds**, ensuring that Joule–Thomson cooling is sufficiently balanced by ambient heat conduction, thus avoiding significant temperature drops below hydrate formation conditions.
- **Implement comprehensive real-time temperature monitoring near the wellbore**, particularly using high-resolution thermocouples or advanced distributed temperature sensing (DTS) systems. Such technologies enable detailed tracking of the thermal evolution around the injection site, facilitating accurate predictions of hydrate formation zones, and allowing timely operational adjustments.
- **Simulate transient cooling processes with enhanced thermal modeling approaches**, explicitly accounting for multiphase occupancy, thermal delays, pore-scale heterogeneities, and non-equilibrium effects. Improved numerical simulations, such as those that integrate advanced EOS accuracy and relative permeability functions, can greatly enhance the predictive capability for hydrate formation risks.
- **Consideration should be given to pre-injection conditioning methods**, such as gradual increases in temperature or pressure management strategies, should be considered to reduce the potential for hydrate formation in sensitive reservoir regions.

Ultimately, these proactive measures, grounded in rigorous experimental data and validated modeling approaches, will be crucial for the robust and safe implementation of large-scale CCS projects, ensuring long-term operational stability and environmental security.

8.5. Limitations and Model Gaps

Although the presented experiments and simulations offer valuable insight into the Joule-Thomson cooling dynamics, several simplifications limit their applicability to field-scale CO_2 injection scenarios. These limitations span both the physical realism of the laboratory setup and the representational accuracy of the numerical models.

- **Homogeneous core material:** Bentheimer and Kentucky sandstone cores are well characterized and largely homogeneous, lacking the mineralogical, textural and permeability heterogeneities found in natural reservoirs. This reduces the variability of cooling fronts and phase transitions, potentially underestimating spatially complex behavior in the field due to the heterogeneity present.
- **Short experimental timeframes:** Experiments were carried out over a period of minutes to hours, depending on when the liquid CO_2 breakthrough was reached. In contrast, field operations occur over weeks to years, allowing for more complete thermal equilibration, gradual saturation changes, and long-term feedbacks (e.g., mineral reactions or hydrate accumulation).
- **Simplified simulation physics:** The simulation approach, while capable of capturing complex multiphase CO_2 behavior, currently does not optimize the input parameters for relative permeability. Such phenomena should be evaluated through a separate set of experiments or inversed from JT experiments.
- **Neglected boundary effects and system-scale coupling:** Laboratory experiments impose boundary conditions (e.g., fixed outlet pressure or inlet flow rate) that are controlled and repeatable, but do not fully replicate field-scale feedbacks such as near-wellbore flow divergence or variable pressure support from the formation.

These limitations restrict the predictive power of current models. However, they successfully capture key first-order effects: the onset of JT cooling, its dependence on injection rate and reservoir pressure, and the interaction between cooling dynamics and pore-scale confinement. The agreement between simulation and experiment, especially when optiomal resolution grids and dense EOS tables are used, suggests that meaningful insights can still be drawn under controlled conditions.

8.6. Challenges in This Research

Investigating the Joule-Thomson cooling effect in porous media experimentally presents several significant technical challenges. The first of these arises from the mechanical complexity of the core-flooding apparatus itself. The experimental setup consists of a dense network of fittings, couplings, and seals, all of which must remain leak-tight under high-pressure CO_2 flow. Even small leaks can cause pressure inconsistencies or thermal disturbances, reducing the accuracy and interpretability of the measured data.

Another key challenge concerns sensor integration. Accurately capturing the transient temperature and pressure fields within the core requires sensors placed with millimeter accuracy. Thermocouples and pressure transducers must be embedded in a way that ensures consistent contact with the porous matrix while simultaneously minimizing disruption to flow paths. Positional mismatches, even on the order of millimeters, can lead to discrepancies in the recorded data.

Furthermore, CO_2 itself presents difficulties in handling. Liquid-phase CO_2 is known to degrade common elastomeric materials, causing swelling and hardening that reduces the responsiveness of components such as back pressure regulators (BPR). Inconsistent BPR behavior has been observed during long-duration experiments, particularly under low-flow conditions, where rubber O-rings become sluggish or deform permanently under thermal stress.

Finally, the thermal response time of the sensors is a limiting factor in transient measurements. Thermocouples with insufficient sensitivity may smooth out or delay the apparent signal of a sharp Joule-Thomson-induced cooling front. As such, it is essential to account for both thermal inertia and potential gas bubble interference, especially near the thermocouple tips, when interpreting the sensor data.

8.7. Key Takeaway

This research highlights that the prediction of JT cooling in CO_2 storage operations extends beyond bulk thermodynamics. It requires insight into the pore-scale processes that govern multiphase flow, flow resistance, and transient heat exchange. Experimental results demonstrate that JT cooling is sensitive to the fluid phase state, porous geometry, and injection regime, with cooling fronts shaped by both enthalpic expansion and confinement-related deviations from classical phase behavior.

The offsets observed from the bulk phase boundary conditions indicate that traditional models alone are insufficient. Accurate forecasting demands simulation tools that incorporate adsorption, dynamic wettability, and improved representations of heat and mass transfer. These findings underscore the need for further experiments that include improved sensor placement, thermal insulation, and possibly in situ visualization to validate and refine numerical predictions and investigate the thermodynamics that govern this offset.

Together, the experiments and simulations presented in this thesis provide a useful insight for understanding JT cooling in porous media. These insights form a necessary foundation to advance CO_2 injection strategies and mitigate hydrate risks in field-scale carbon storage operations.

9

Conclusion and Recommendations

This thesis presented a detailed experimental and numerical investigation of the Joule-Thomson cooling effect during CO_2 injection into porous sandstone cores. By examining the thermal and hydraulic response of two contrasting rock types, this study assessed the feasibility of replicating near-wellbore thermal effects under realistic CCS conditions and generated datasets for the validation of numerical models. The main conclusions and recommendations for future work are summarized below.

9.1. Conclusions

This research was guided by a primary research question and four sub-questions. Based on the experimental and numerical results synthesized and interpreted throughout this thesis, the following conclusions are drawn:

Laboratory setups can successfully validate and deconvolve the core physical mechanisms of JT cooling, but prediction remains challenging without empirical calibration.

The methodology developed, using contrasting core permeabilities, effectively isolated two dominant cooling regimes: continuous isenthalpic expansion in low-permeability media (Chapter 4) and evaporation-dominated cooling in high-permeability media (Chapter 5). This confirms that the dominant cooling process is rock-type dependent. However, a systematic offset of up to 4 bar or 3°C from the bulk CO_2 phase boundary was consistently observed, highlighting the limitations of using bulk thermodynamics alone for prediction (Chapter 7).

Permeability is a first-order control on the cooling mechanism, while the final outlet pressure dictates the minimum achievable temperature.

In low-permeability systems, the internal pressure gradient governs the spatial distribution of cooling. In high-permeability systems, the outlet pressure (simulating reservoir pressure) controls the phase transition, making it the key determinant of the final temperature. Flow rate was found to primarily affect the propagation speed of the thermal front and measurement stability rather than the final temperature. Ultimately, the reservoir pressure, which sets the minimum pressure for expansion, dictates the maximum attainable temperature drop in both core types.

A systematic offset from the bulk CO_2 phase boundary exists and is not explained by classical theories.

Phase transitions were consistently observed at pressures 3–4 bar lower than predicted by bulk data. As analyzed in Chapter 7, this deviation is too large to be attributed to Gibbs-Thomson or Kelvin effects and is likely governed by a combination of non-equilibrium kinetics and rock-fluid interactions, such as adsorption. This implies that using bulk thermodynamics alone is insufficient for accurate prediction of hydrate risk. Furthermore, residual experimental uncertainties, such as sensor placement and thermal

lag, were found to be contributing factors, as confirmed by CT scans and detailed in Appendix A.1.

Predictive numerical simulation is critically dependent on the quality of physical input models.

Although the DARTS simulator qualitatively reproduced the observed cooling trends, the quantitative accuracy was highly sensitive to the input of the model. Achieving a match with the experimental data required high-resolution Equation of State (EOS) tables (>2000 points) to avoid numerical artifacts. Most importantly, the absence of an accurate relative permeability model for the liquid-gas CO_2 system was a key limitation, which prevented the simulation from capturing the pressure build-up observed in low-permeability experiments (Chapter 6). Although using elevated initial water saturation as a proxy for liquid accumulation successfully reproduced similar pressure dynamics, this workaround highlights the fundamental need for empirically derived physics to be incorporated into the simulation framework. Similarly, optimal grid resolution (around 400 cells for this system) was found to be necessary, since both coarser and significantly finer grids introduced numerical instabilities.

9.2. Recommendations for Future Research

Based on the findings of this work, the following areas are recommended for future investigation:

- Optimize relative permeability functions for the liquid-gas CO_2 system through dedicated two-phase flow experiments or inverse modeling of the pressure data from this study.
- Establish an empirical database of phase boundary offsets across a wider range of lithologies to develop predictive correlations based on petrophysical properties like mineralogy and surface area.
- Investigate the coupled feedback between hydrate formation, flow assurance, and pressure evolution by conducting experiments with initial water saturation.
- Refine experimental accuracy by redesigning sensor cavities to minimize thermal lag and by employing in-situ imaging techniques (e.g., micro-CT) to directly visualize multiphase flow.
- Examine the impact of cyclic injection schemes and long-term geochemical interactions on the thermal and mechanical stability of the reservoir rock.
- Advance numerical models by extending them to 3D radial geometries and incorporating the empirically derived physics for relative permeability and phase behavior identified in this work.

References

AlKharraa, H. S., Wolf, K. H. A., Kwak, H. T., Deshenenkov, I. S., AlDuhailan, M. A., Mahmoud, M. A., Arifi, S. A., AlQahtani, N. B., AlQuraishi, A. A., & Zitha, P. L. (2023). A Characterization of Tight Sandstone: Effect of Clay Mineralogy on Pore-Framework. *Society of Petroleum Engineers - SPE Reservoir Characterisation and Simulation Conference and Exhibition 2023, RCSC 2023*. https://doi.org/10.2118/212638-MS

Bachu, S. (2008). CO2 storage in geological media: Role, means, status and barriers to deployment. *Progress in Energy and Combustion Science*, *34*(2), 254–273. https://doi.org/10.1016/J.PECS.2007.10.001

Benson, S. M., & Cole, D. R. (2008). CO2 sequestration in deep sedimentary formations. *Elements*, *4*(5), 325–331. https://doi.org/10.2113/gselements.4.5.325

Chesnokov, C., Farajzadeh, R., Ohemeng, K., Prempeh, K., Kahrobaei, S., Snippe, J., & Bedrikovetsky, P. (2025). *Joule-Thomson cooling of CO2 injected into aquifer under heat exchange with adjacent formations by Newton's law-1D exact solution* (tech. rep.). https://scispace.com/pdf/joule-thomson-cooling-of-co2-injected-into-aquifer-under-46j7bwvzsn.pdf

Chesnokov, C., Farajzadeh, R., Prempeh, K. O. K., Kahrobaei, S., Snippe, J., & Bedrikovetsky, P. (2024). Analytical model for Joule-Thomson cooling under heat exchange during CO2 storage. *Advances in Water Resources*, *190*, 104758. https://doi.org/10.1016/J.ADVWATRES.2024.104758

Duffy, J. A., Wilkinson, N. J., Fretwell, H. M., Alam, M. A., & Evans, R. (1995). Phase transitions of CO2 confined in nanometer pores as revealed by positronium annihilation. *Journal of Physics: Condensed Matter*, *7*(50), L713. https://doi.org/10.1088/0953-8984/7/50/003

Energy Agency, I. (2020). *Technology Perspectives Energy Special Report on Carbon Capture Utilisation and Storage CCUS in clean energy transitions* (tech. rep.). Energy Technology Perspectives. https://www.iea.org/reports/ccus-in-clean-energy-transitions

Fuchs, S., Förster, H. J., Norden, B., Balling, N., Miele, R., Heckenbach, E., & Förster, A. (2021). The Thermal Diffusivity of Sedimentary Rocks: Empirical Validation of a Physically Based α - ϕ Relation. *Journal of Geophysical Research: Solid Earth*, *126*(3). https://doi.org/10.1029/2020JB020595

Hoteit, H., Fahs, M., & Soltanian, M. R. (2019). Assessment of co_2 injectivity during sequestration in depleted gas reservoirs. *Geosciences*, *9*(5), 199. https://doi.org/10.3390/geosciences9050199

hpp-performance. (2019). Typical properties PEEK. https://www.hpp-performance.com/fileadmin/user_upload/user_upload/fluteck_K_300-FLS_v15.03_datenblatt_PEEK.pdf

IPCC. (2022, June). *Climate Change 2022: Mitigation of Climate Change. Contribution of Working Group III to the Sixth Assessment Report of the Intergovernmental Panel on Climate Change*. Cambridge University Press. https://doi.org/10.1017/9781009157940

Jones, S. A., Kahrobaei, S., Van Wageningen, N., & Farajzadeh, R. (2022). CO2Foam Behavior in Carbonate Rock: Effect of Surfactant Type and Concentration. *Industrial and Engineering Chemistry Research*, *61*(32), 11977–11987. https://doi.org/https://doi.org/10.1021/acs.iecr.2c01186

Li, J., Rao, Q., Xia, Y., Hoepfner, M., & Deo, M. D. (2020). Confinement-mediated phase behavior of hydrocarbon fluids: Insights from Monte Carlo simulations. *Langmuir*, *36*(26), 7277–7288. https://doi.org/10.1021/acs.langmuir.0c00652

Lienhard, J. H. (2020). *A heat transfer textbook fifth edition*. http://ahtt.mit.edu.

Maloney, D. R., & Briceno, M. (2008). Experimental Investigation of Cooling Effects Resulting from Injecting High Pressure Liquid or Supercritical CO2 into a Low Pressure Gas Reservoir. *International Symposium of the Society of Core Analysts*. https://www.researchgate.net/publication/281181852_Experimental_Investigation_of_Cooling_Effects_Resulting_from_Injecting_High_Pressure_Liquid_or_Supercritical_CO2_Into_a_Low_Pressure_Gas_Reservoir

Mathias, S. A., Gluyas, J. G., Oldenburg, C. M., & Tsang, C. F. (2010). Analytical solution for Joule-Thomson cooling during CO2 geo-sequestration in depleted oil and gas reservoirs. *International Journal of Greenhouse Gas Control*, *4*(5), 806–810. https://doi.org/10.1016/j.ijggc.2010.05.008

Mulero, A., Cachadiña, I., & Parra, M. I. (2012). Recommended Correlations for the Surface Tension of Common Fluids. *Journal of Physical and Chemical Reference Data*, *41*(4). https://doi.org/10.1063/1.4768782

NIST. (2025). Carbon dioxide. https://webbook.nist.gov/cgi/cbook.cgi?ID=C124389&Mask=4

Oldenburg, C. M. (2006). *JOULE-THOMSON COOLING DUE TO CO2 INJECTION INTO NATURAL GAS RESERVOIRS* (tech. rep.). https://www.osti.gov/servlets/purl/898956

Oldenburg, C. M. (2007). Joule-Thomson cooling due to CO2 injection into natural gas reservoirs. *Energy Conversion and Management*, *48*(6), 1808–1815. https://doi.org/10.1016/j.enconman.2007.01.010

Orlander, T. ; Adamopoulou, E., Jerver Asmussen, J., Marczyński, A. A., Milsch, H. ; Pasquinelli, L. ; & Fabricius, I. L. (2018). General rights Thermal conductivity of sandstones from Biot's coefficient Thermal conductivity of sandstones from Biot's coefficient. *Geophysics*, *83*(5), 173–185. https://doi.org/10.1190/geo2017-0551.1

Peksa, A. E., Wolf, K. H. A., & Zitha, P. L. (2015). Bentheimer sandstone revisited for experimental purposes. *Marine and Petroleum Geology*, *67*, 701–719. https://doi.org/10.1016/J.MARPETGEO.2015.06.001

Pruess, K. (2005). Numerical studies of fluid leakage from a geologic disposal reservoir for CO2 show self-limiting feedback between fluid flow and heat transfer. *Geophysical Research Letters*, *32*(14), 1–4. https://doi.org/10.1029/2005GL023250

Singh, M., Tangirala, S. K., & Chaudhuri, A. (2020). Potential of CO2 based geothermal energy extraction from hot sedimentary and dry rock reservoirs, and enabling carbon geo-sequestration. *Geomechanics and Geophysics for Geo-Energy and Geo-Resources 2020 6:1*, *6*(1), 1–32. https://doi.org/10.1007/S40948-019-00139-8

Tian, X., Volkov, O., & Voskov, D. (2024). An advanced inverse modeling framework for efficient and flexible adjoint-based history matching of geothermal fields. *Geothermics*, *116*. https://doi.org/10.1016/j.geothermics.2023.102849

Tweed, L. E., Bickle, M. J., & Neufeld, J. A. (2024). Transient Joule–Thomson cooling during CO2 injection in depleted reservoirs. *Journal of Fluid Mechanics*, *997*. https://doi.org/10.1017/jfm.2024.845

Vivas, C., Hu, Z., & Salehi, S. (2023). Texture-Dependent Thermal Properties of Sandstone Rocks Examined by Scanning Electron Microscopy for Thermal Energy Storage Applications. https://doi.org/10.1115/1.4064030

Voskov, D., Saifullin, I., Novikov, A., Wapperom, M., Orozco, L., Seabra, G. S., Chen, Y., Khait, M., Lyu, X., Tian, X., de Hoop, S., & Palha, A. (2024). open Delft Advanced Research Terra Simulator (open-DARTS). *Journal of Open Source Software*, *9*(99), 6737. https://doi.org/10.21105/joss.06737

Voskov, D. V. (2017). Operator-based linearization approach for modeling of multiphase multi-component flow in porous media. *Journal of Computational Physics*, *337*. https://doi.org/10.1016/j.jcp.2017.02.041

Wang, H., Wang, J., Wang, X., Dou, F., & Hu, B. (2019). Coupled hydro-thermal-mechanical analysis for cold CO2 injection into a deep saline aquifer. *Thermal Science*, *23*, S917–S925. https://doi.org/10.2298/TSCI180511127W

Wang, Z., Pereira, J. M., & Gan, Y. (2021). Effect of Grain Shape on Quasi-Static Fluid-Fluid Displacement in Porous Media. *Water Resources Research*, *57*(4). https://doi.org/10.1029/2020WR029415

Wapperom, M., dos Santos, J. H., & Voskov, D. (2024). SPE-223902-MS Thermal-Compositional Simulation of CO2 Sequestration in Depleted Hydrocarbon Reservoirs. *SPE Annual Technical Conference and Exhibition*. https://doi.org/10.2118/223902-MS

Wapperom, M., Tian, X., Novikov, A., & Voskov, D. (2024). FluidFlower Benchmark: Lessons Learned from the Perspective of Subsurface Simulation. *Transport in Porous Media*, *151*(5). https://doi.org/10.1007/s11242-023-01984-8

Zamani, N., Shokri, A. R., Chalaturnyk, R., Gasda, S. E., & Berenblyum, R. (2024). *Significance of the Joule-Thomson Cooling Effect for Geological CO 2 Storage in Depleted Gas Reservoirs* (tech. rep.). https://ssrn.com/abstract=5070337

Zhang, J., Clennell, M. B., Liu, K., Pervukhina, M., Chen, G., & Dewhurst, D. N. (2016). Methane and Carbon Dioxide Adsorption on Illite. *Energy and Fuels*, *30*(12), 10643–10652. https://doi.org/https://doi.org/10.1021/acs.energyfuels.6b01776

Zhou, L., Parhizi, M., & Jain, A. (2021). Temperature distribution in a multi-layer cylinder with circumferentially-varying convective heat transfer boundary conditions. *International Journal of Thermal Sciences*, *160*, 106673. https://doi.org/10.1016/J.IJTHERMALSCI.2020.106673

Ziabakhsh-Ganji, Z., & Kooi, H. (2014). Sensitivity of Joule-Thomson cooling to impure CO2 injection in depleted gas reservoirs. *Applied Energy*, *113*, 434–451. https://doi.org/10.1016/j.apenergy.2013.07.059

A

Experimental improvements in methodology

A.1. Sensor Configuration and Calibration

The experimental setup employs a comprehensive array of sensors to accurately capture the profiles of temperature, absolute pressure, and differential pressure (dP) profiles during CO_2 injection. Eight pressure sensors (rated at 100 bar) and seven Type-K thermocouples (0.5 mm diameter) were placed at regular intervals of 6.7 cm along the axial length of the core. In addition, six differential pressure sensors with a range of 300 mbar provided detailed measurements of subtle pressure variations along the flow path. These sensors ensured accurate measurements of pressure gradients and detection of potential internal leaks, such as those identified during preliminary tests (e.g., negative readings in differential pressure sensor dP6 indicating internal bypass flow paths).

Sensor calibration was performed prior to the experiments:

- Thermocouples were calibrated to ensure accurate readings in a wide range (−50 °C to 100 °C).
- Absolute pressure and dP pressure sensors were verified against known reference pressures, ensuring stable baselines and minimal drift throughout the experiments.

During initial Bentheimer experiments, the sensors T2, T3, T5 and T6 exhibited inconsistent readings, likely due to suboptimal insertion geometry. This was confirmed by early CT scans, which revealed a variation in sensor depth, as can be seen in Figure A.1 These alignment issues were resolved in later experiments by carefully adjusting the depth of insertion.

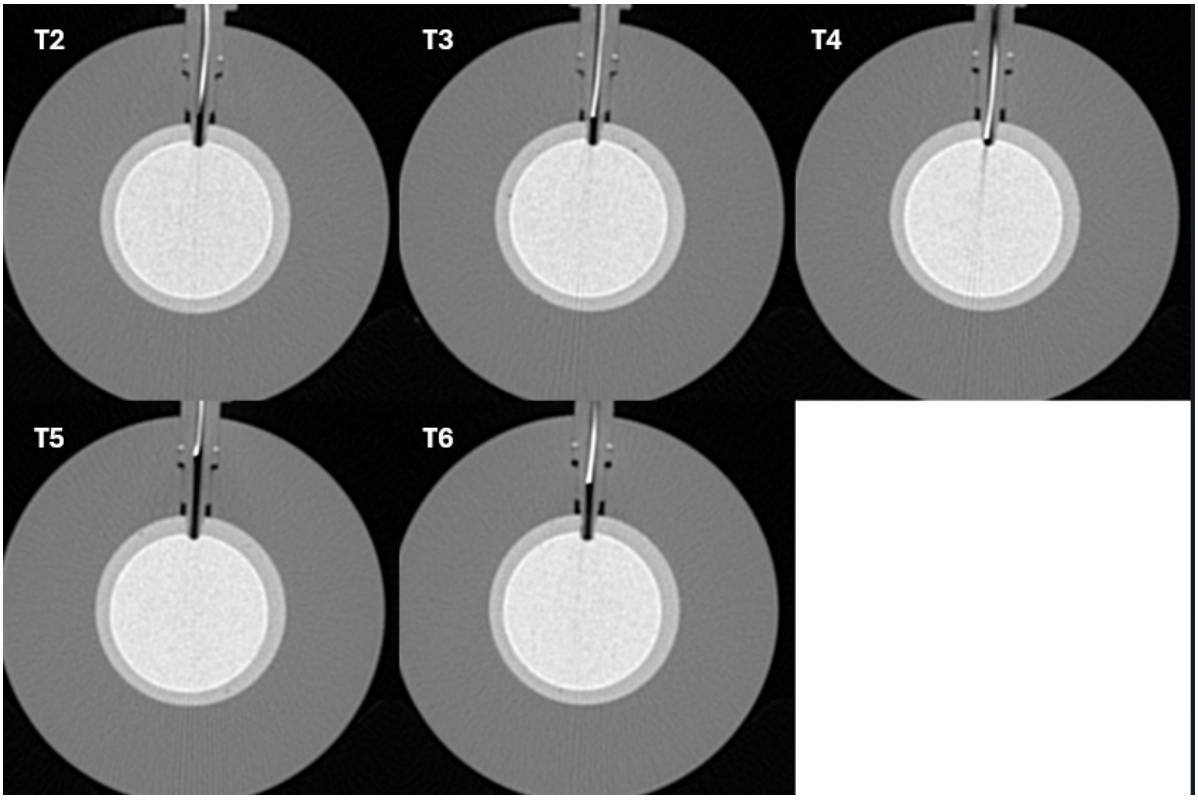

Figure A.1: Ct scan of the Bentheimer rock sample, where the exact radial slices of T2 (top left) to T6 (bottom right) are shown. The bright white traces represent the metal sensor bodies. A clear difference in insertion depth and positioning is visible, with T4 being the deepest and T5 being the shallowest sensor.

The design of the sensor cavity was a major contributor to the observed problems. The radial thermocouple ports are sealed and do not allow for flow, leading to stagnant zones around the sensor tips during injection. CO_2 gas has low thermal conductivity ($\lambda_{\text{gas}} \approx 0.014$ W/(m · K) at 1 bar, 20°C), which delays thermal equilibration between the sensor tip and the surrounding rock. In contrast, liquid CO_2 has a higher conductivity ($\lambda_{\text{liq}} \approx 0.08$ W/(m · K)), improving heat transfer if present (NIST, 2025).

In addition to this insulation effect, parasitic heat conduction along the metallic thermocouple wires contributed to signal damping. These wires, housed in a PEEK sheath, can transfer heat from the ambient lab environment to the sensor tip. This effect becomes significant during steep thermal gradients, counteracting the local cooling from the JT effect and flattening the measured signal.

CT imaging confirmed that the thermocouples were inserted at varying depths, forming stagnant gas volumes between the tip and the flowing pore fluid. For example, in the Kentucky core scan, the sensor depths ranged from deepest (T4) to shallowest (T6), consistent with the observed signal delays. The CT scan image slices can be found in Figures A.1.

The optimized configuration shown in Figure A.2, demonstrates full insertion of all active thermocouples into the pore volume boundary, significantly improving the temperature tracking accuracy across the core. Although T6 is more difficult to identify due to non-ideal positioning within the machined port, a faint bright tip can be discerned upon close inspection, indicating contact with the rock boundary. Hypotheses on why this caused the temperature sensors to differ so much from each other are explored in further detail in Appendix B.

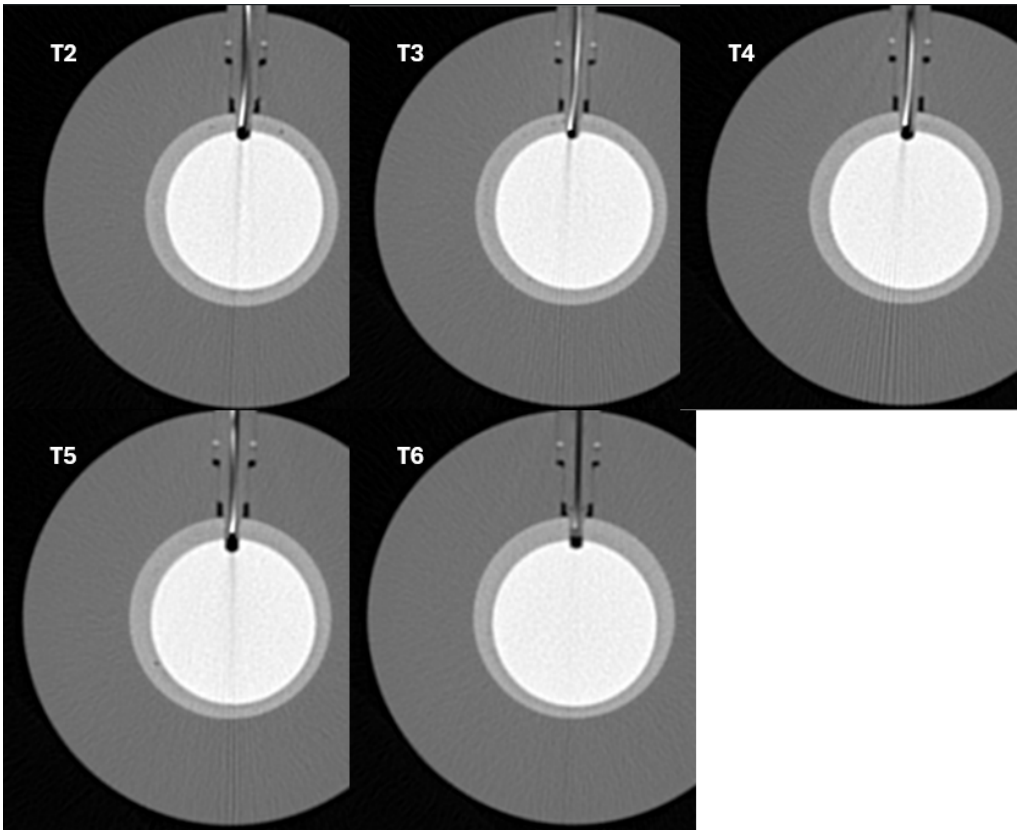

Figure A.2: CT scan showing the optimized sensor configuration in the Kentucky core. All thermocouples are now in full contact with the outer rock surface, ensuring reliable thermal readings. The insertion depths are uniform and the sensor shafts visibly intersect the rock boundary. T6 is harder to spot but by close inspection, a faint bright tip can be spotted at the correct position.

A.2. Leak Detections With Thermal Imaging

Although the system is designed to observe Joule-Thomson cooling in isolation, thermal losses to the environment are unavoidable and must be addressed.

Thermal imaging is used to detect unwanted flow; the Joule-Thomson cooling effect ensured a visible change in temperature, this cold gas is able to move towards a leak in the system (eg. A leak in the pressure sensor tube or connector) resulting in the following image A.3. This image shows a synthetic leak in the pressure sensor lines to force cold gas in the tubes.

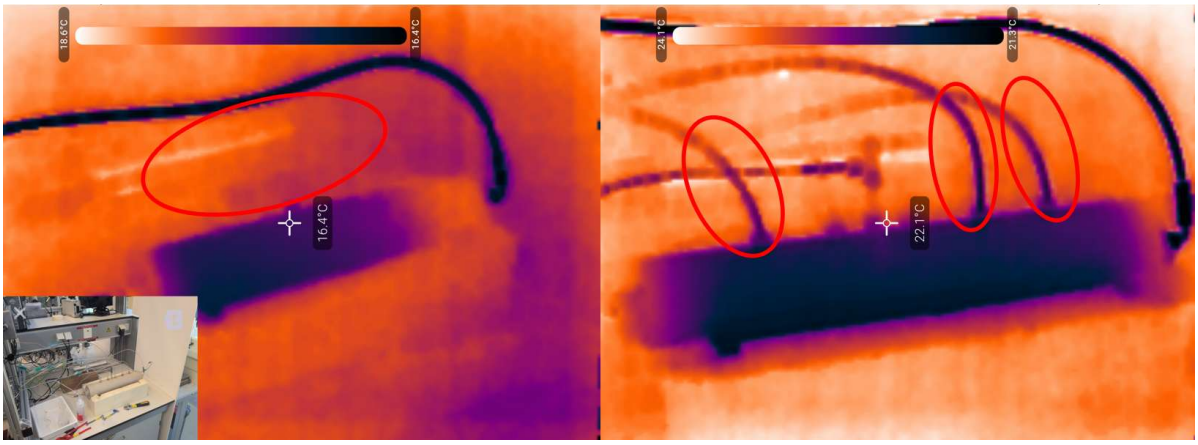

Figure A.3: Example of leak detection with a thermal camera. On the left, the non-leaking core can be seen with no visible cold line towards the pressure sensors. On the right, indicated with red circles, cold lines can be observed due to the cold gas moving towards the leak in the pressure sensor tube.

A.3. Iterative Optimizations and System Refinements

During the preliminary Bentheimer experiments, several hardware and procedural improvements were implemented to enhance the stability, reliability, and reproducibility of the test setup.

Sensor data acquisition was initially handled by two communication modules, each with distinct noise characteristics and latency. This configuration introduced inconsistencies in digital noise across sensor channels. To resolve this, all sensors were consolidated into a single communication and logging unit. This ensured synchronized sampling and uniform signal processing across the dataset.

Another critical upgrade involved the outlet back pressure regulator. The original PEEK-based unit was replaced with a stainless steel variant featuring a redesigned internal geometry. This change improved the stability of the pressure response under dynamic flow conditions. Furthermore, the stainless steel body allowed external heating (e.g., via a hotplate), which ensured the internal elastomeric seals remain above freezing and prevents stiffness-induced instability in the outlet pressure.

B

Temperature Sensor Location Methodology

Throughout the experimental campaign, temperature readings from thermocouples embedded in the core-holder occasionally exhibited delayed responses, reduced amplitude, or anomalously shallow cooling behavior. Under steady-state JT cooling conditions, particularly in a high-permeability core such as Bentheimer, one would expect that all internal sensors eventually register similar minimum temperatures, reflecting thermal equilibrium between the injected CO_2 and the surrounding rock matrix. However, contrary to this expectation, significant variations were observed between sensors, some of which failed to capture the full extent of the cooling front even after extended injection periods.

These discrepancies were especially pronounced during the Bentheimer test series. At that time, the coreholder configuration had not yet been optimized for uniform sensor placement. These irregularities raised concerns about the reliability of the temperature data, prompting a more detailed investigation into possible causes.

To assess the origin of the observed deviations and ensure the physical validity of the thermal profiles, a set of diagnostic procedures and working hypotheses were developed. These included mechanical inspection of the sensor assembly, thermal calibration checks, controlled heat transfer tests, and CT imaging of sensor positions relative to the flow domain. The goal was to distinguish between instrumentation-related artifacts (e.g. sensor depth, thermal lag) and genuine physical effects (e.g., heterogeneous flow, phase separation) that could influence temperature readings.

The insights gained from this diagnostic effort directly informed the subsequent redesign of the thermocouple mounting system and the calibration procedure, thus improving the overall accuracy and comparability of temperature measurements in the series of experiments with Kentucky sandstone.

B.1. Temperature Sensor Response Tests

Although the Type-K thermocouples used are rated for high accuracy (±0.01 K resolution), several issues emerged when they were used in the radial sensor ports of the coreholder, as described in Chapter 5.3.1. These problems were amplified under rapid Joule-Thomson (JT) cooling conditions, where accurate measurements of the temperature fronts are critical, which is why the problem was found. Most notably, sensors T2, T3, T5 and T6 often displayed shallower or slower responses than expected based on flow conditions and pressure drops.

Test 1: Passive Thermal Inertia Evaluation

To exclude sensor malfunction or electronic drift, the first response test involved external heating of the core to 35°C using a heating sleeve and subsequently allowing it to cool passively through ambient conduction. The temperature evolution was tracked for all sensors.

Result: All sensors responded symmetrically and exhibited similar cooling profiles. No specific sensor

showed persistent offsets or timing lags. Although this ruled out electronic or calibration-based error, it did not recreate the specific transient features of JT-driven cooling experiments, where each sensor has a different response. As heating and cooling are driven by external devices or room temperature, the heat flux is happening from the outside inward, while the temperature change from JT effect occurs from the inside to the outside. This difference could be the key to the location of the problem. This result also restricted the problem to the inside of the coreholder, either a secondary cooling phenomenon or a translation issue from the core to the sensors, and prompted a deeper investigation into potential mechanical or flow-induced causes.

Test 2: Gravitational Orientation and Stratification Effects

To investigate whether gravitational stratification influences the fluid distribution and thermal sensor response, the coreholder was rotated by 130° about its longitudinal axis, reversing the orientation of the thermocouples so that they entered from below the core instead of from above. The rationale was that denser, liquid-phase CO_2 might preferentially accumulate at the bottom of the core under gravity, potentially improving thermal contact with sensors inserted from this direction.

Result: Figure B.1 shows that the overall temperature profiles closely resemble those observed in upright orientation (experiment 13), particularly with respect to the minimum temperatures reached at each thermocouple location. This indicates that gravitational stratification does not significantly affect the final thermal equilibrium or the ultimate extent of JT cooling at steady state.

However, a key distinction is evident in the initial cooling rate. In the rotated configuration, the temperature drops are more abrupt, suggesting faster heat transfer and more immediate thermal contact between the sensor tips and the cold CO_2 phase. This observation supports the hypothesis that the gravitational pooling of liquid CO_2 near the tip of the sensor enhances the transient thermal response, even if it does not change the final temperature plateau.

However, these early cooling dips are often short-lived and are followed by a rapid temperature rebound. This behavior is attributed in part to the supply instability caused by the backpressure cartridge (BPC). During the experiment, irregular pressure pulses from the BPC caused fluctuations in inlet pressure and injection rate. These transient instabilities altered the instantaneous cooling capacity of the flow, leading to sharp but short cooling spikes that temporarily exceeded the expected equilibrium minima.

Despite this, the consistent pattern of accelerated initial temperature decline suggests that the improved sensor response is not merely an artifact of BPC instability. The enhanced transient conductivity probably results from better contact between the sensor tip and the cold liquid CO_2 that accumulates near the base of the core.

In conclusion, while buoyancy effects do not appear to govern steady-state JT cooling behavior, they do modulate the rate at which thermocouples register the onset of cooling. These results reinforce the idea that mechanical and geometric characteristics of the sensor cavities (e.g., insertion depth, liquid accessibility) remain the dominant factors in determining thermal response sensitivity but that gravity may enhance transient thermal coupling under specific configurations.

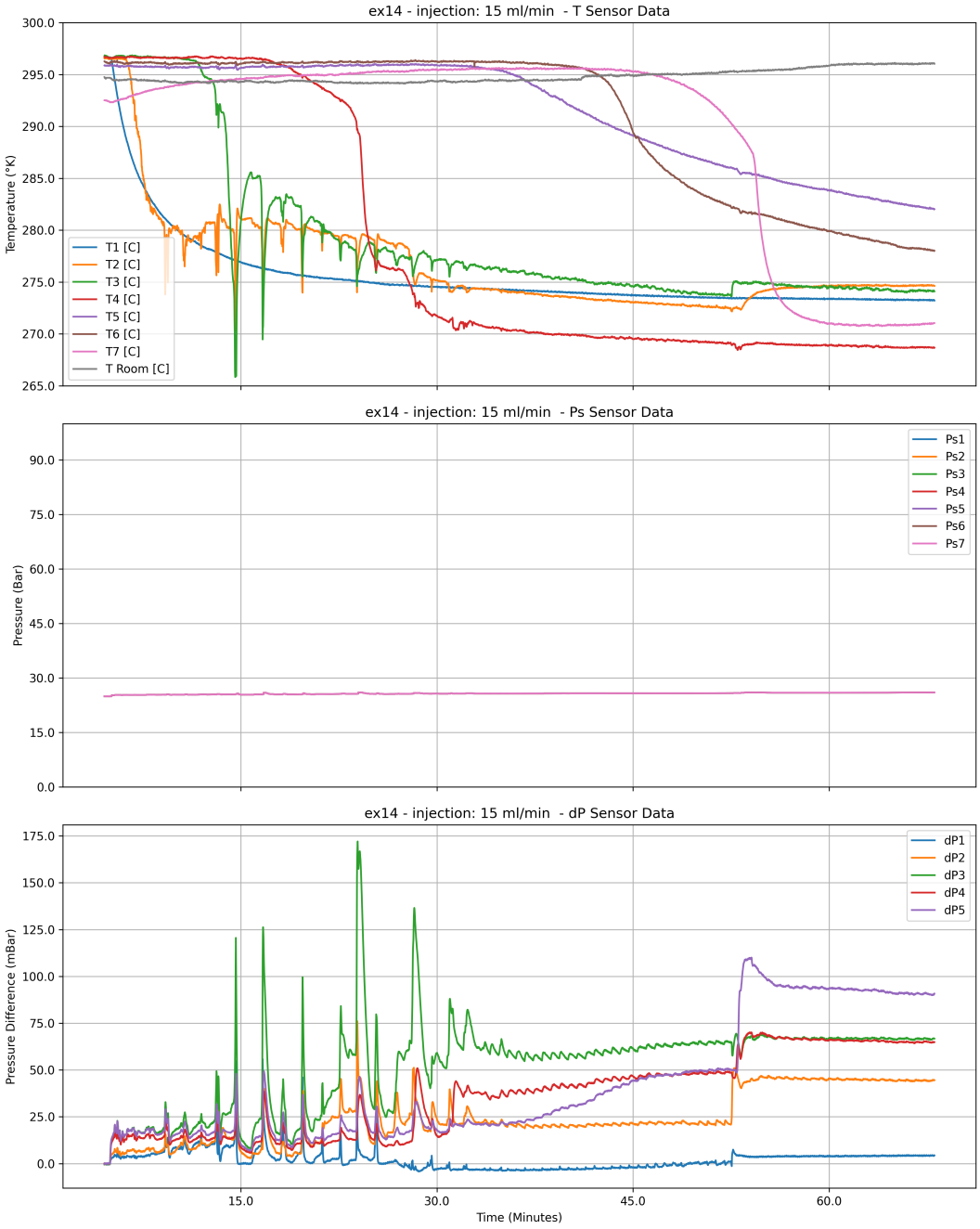

Figure B.1: Temperature evolution during experiment 14 with coreholder rotated 130°. The faster decline suggests improved contact between thermocouples and cold liquid CO_2.

Test 3: Venting Individual Sensor Cavities

To directly evaluate whether sensor placement causes stagnant gas which acts as a partial insulator, a third experiment was conducted. After completion of a standard JT cooling experiment and reaching a core fully saturated with liquid CO_2, the injection was continued to maintain the liquid state. The individual sensor cavities were then briefly vented by opening the lines connected to the differential pressure sensors. This induced a localized pressure drop, drawing cold liquid CO_2 directly from the porous matrix into the sensor cavity and through the thermocouple. Venting was performed one sensor at a time to isolate responses.

Result: In all cases, the sensor registered a rapid and sharp temperature drop within seconds of venting,

much steeper than during core injection. In several cases, the measured temperatures dropped below the values recorded during regular injection, consistent with additional cooling from rapid depressurization as calculated in 5.3.5. All sensors shared this trait, except for T4, which remained relatively constant, indicating that this sensor was already in good contact with liquid CO_2 before bleeding. This confirmed that the primary source of damping is not sensor electronics, but thermal isolation due to the imperfect design of the thermocouple positions.

Connection to Other Experiments

It is important to contextualize the thermocouple positioning improvements in relation to the broader experimental series. All Bentheimer experiments were conducted **before** these optimizations were implemented. As a result, sensor placement during the Bentheimer phase exhibited notable inconsistencies in terms of the axial insertion depth within the PEEK connector housings.

Specifically, the order of sensitivity T4 > T3 > T2 > T6 > T5 matches the progression from the shallowest to the deepest cavity. This alignment reinforces the interpretation that the mechanical insertion depth plays a critical role in thermal signal fidelity during JT cooling experiments. Only T4 is considered reliable for precise temperature-based analysis. Other sensor readings in that dataset are treated qualitatively or used only for cross-comparison when showing similar trends.

To address this issue, all thermocouple connectors were physically modified **after** the Bentheimer experiment series by shortening the PEEK tubes that held the sensors. This adjustment allowed the thermocouples to protrude further into the flow path, improving their thermal contact with the rock matrix and fluid stream. The success of this modification was verified through a second CT scan of the Kentucky core setup, which confirmed the consistent placement of all sensors near the internal face of their respective housings.

As a consequence of this improvement, the Kentucky experiments can be interpreted with significantly higher confidence in the thermal data across all sensors in the core (T2 to T6)

C

Permeability calculations

C.1. Kentucky

C.1.1. Pre-experiment permeability measurements

Permeability tests were performed with CO_2 as the working gas. A mass flow controller (MFC) was installed upstream of the core to provide a constant volumetric flow rate. The inlet back pressure cartridge was removed to avoid artificial pressure drops, allowing a purely pressure-driven configuration.

Multiple outlet back pressures were applied in a range of approximately 0 to 15 bar. For each back pressure step, the CO_2 mass flow was held steady for long enough to reach the pressure equilibrium in all segments.

Table C.1 summarizes the conditions for each test. Normal flowrate defined as the flowrate set at the inlet mass flow controller.

Table C.1: Flow test configurations for the Kentucky sandstone core

Test	BPR [bar]	Normal flowrate [mL/min]
Kentucky_flowtest1	0	5–20
Kentucky_flowtest2	10	5–100
Kentucky_flowtest3	15	10–125

Permeability Calculation Methodology

Permeability k was calculated using Darcy's law:

$$k = \frac{Q\mu L}{A\Delta P}$$

where:

- Q is the volumetric flow rate [m^3/s],
- μ is the dynamic viscosity of the injected gas (CO_2) [Pa·s],
- L is the segment length [m],
- A is the cross-sectional area of the core [m^2],
- ΔP is the measured pressure drop across each segment [Pa].

CO_2 viscosity was evaluated at the measured mean pressure and temperature using standard correlations according to NIST (2025). The calculations were repeated for each flow step to obtain a series of measured permeabilities as a function of the inverse mean pressure.

Klinkenberg Correction

Due to gas slippage effects, especially at lower pressures, the measured permeability tends to be higher than the intrinsic permeability. This is corrected using the Klinkenberg relation:

$$k_{\text{app}} = k_{\infty}\left(1 + \frac{b}{P}\right)$$

where k_{app} is the apparent gas permeability, k_{∞} is the intrinsic permeability (liquid equivalent), P is the mean pressure, and b is the Klinkenberg slip factor.

Linear regression was applied to the plots of k_{app} vs. $1/P$ to determine both k_{∞} and the slip factor b for each segment. Figure C.1 shows representative fits and the resulting permeability corrections.

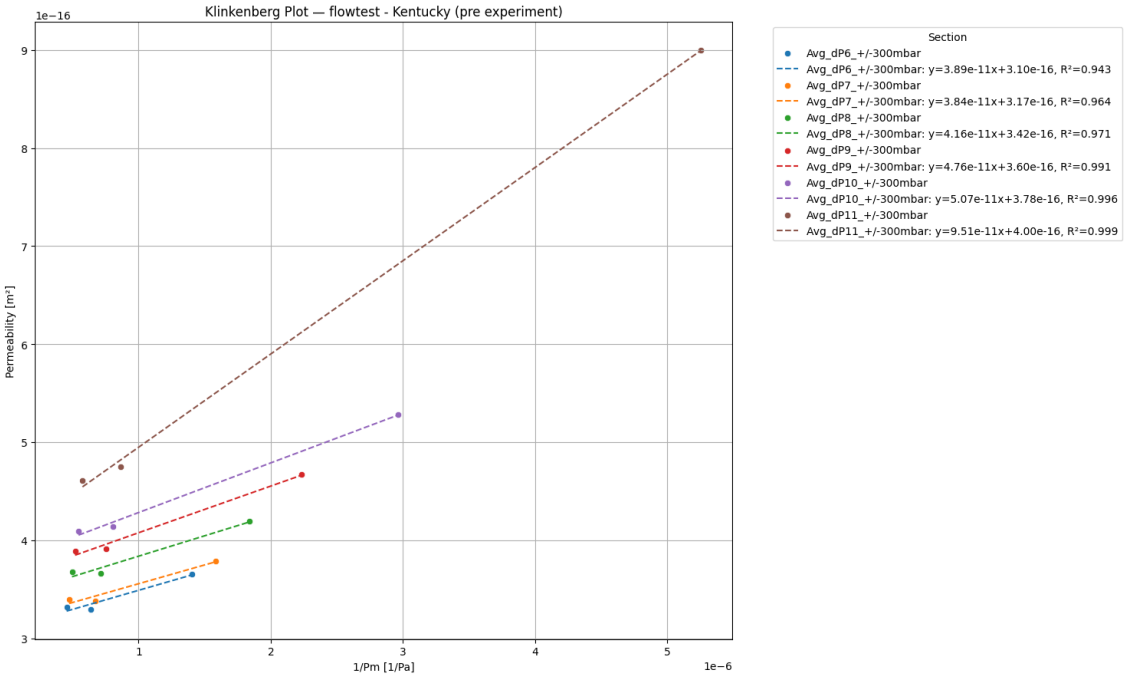

Figure C.1: Klinkenberg-corrected permeability plots for the Kentucky sandstone core. Linear regressions yield intrinsic permeability per segment.

C.1.2. Post-experiment permeability measurements

A second series of gas-phase permeability tests was performed after the JT cooling experiments. The setup and procedure mirrored those of the pre-experiment flow tests.

Table C.2: Detailed overview of mass flow permeability tests, including inlet pressures, back pressure regulator steps, and applied flowrate ranges.

Test Name	back pressure regulator Steps [Bar gauge]	Normal flowrates [mL/min]
flowtest1	0, 1, 2.3, 3.5, 5, 10.7	50–600
flowtest2	15.1, 20.8	100–600
flowtest3	25.85, 30.2	100–600

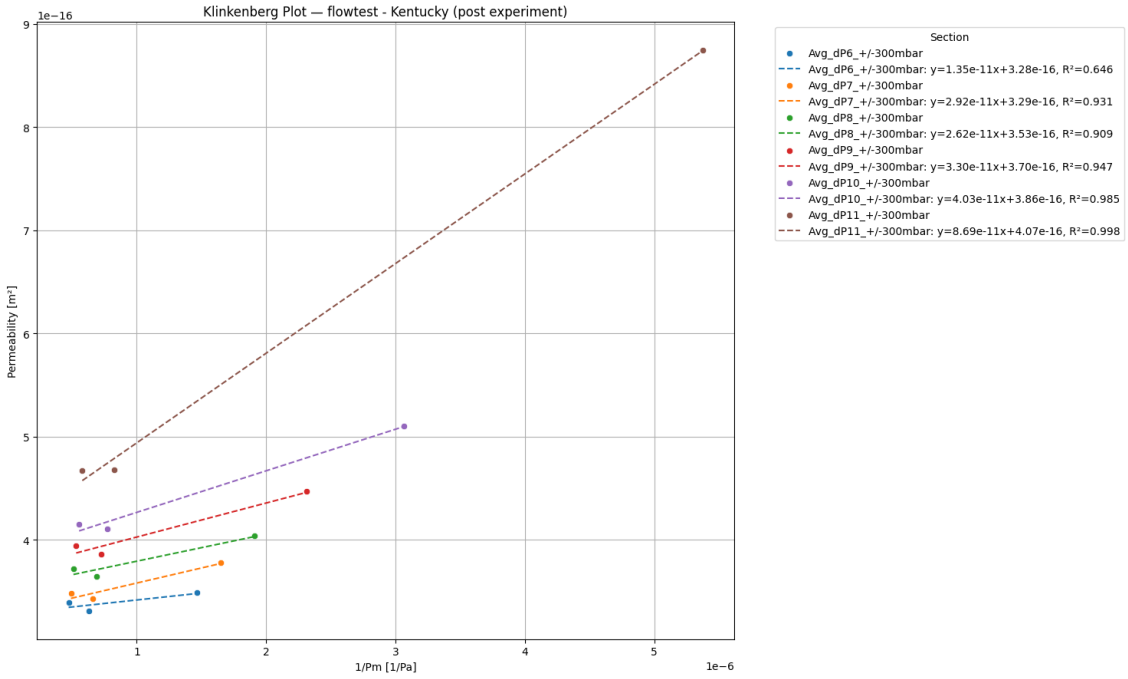

Figure C.2: Klinkenberg-corrected permeability plots for the Kentucky sandstone core after the Joule-Thomson cooling experiments. Permeability trends are consistent with pre-experiment values.

Figure C.2 shows the results of the Klinkenberg correction applied to the post-experiment data. The permeability profiles across the segments closely match those from the pre-experiment tests, confirming that the core remained largely unaltered during the full Joule-Thomson cooling campaign.

C.1.3. Implications

From both a modelling and an experimental design perspective, the repeatability of permeability in the Kentucky core is critical. It allows calibration of the DARTS simulations using verified post-experiment permeability measurements without requiring time-dependent permeability evolution models. These values will be used as direct input for the Kentucky Joule-Thomson cooling simulations in Chapter 6.

C.2. Bentheimer

Experimental Configuration

Multiple flow rates were applied over a range of system pressures (1 to 30 bar) by controlling the BPR at the outlet. At each pressure step, the mass flow controller delivered steady-state flow, and differential pressures between the core segments were recorded. The flow stability and sensor integrity were closely monitored, as unstable behaviour (e.g., pressure oscillations) would invalidate assumptions of laminar, steady flow and were thus excluded from analysis.

Table C.2 summarizes the flowtest configurations, including the pressure steps applied to the BPR. The pressure indicated for the BPR is in bar according to the gauges. The flow rate is indicated as normal flow, which means the flow measured at the MFC. Each subtest included a set of differential pressure

measurements at multiple outlet pressure levels, increasing the robustness of the regression for the Klinkenberg correction. However, at higher system pressures, a significant decrease in the pressure differential between segments was observed, as a result of the compressibility effect. This reduction in the actual flow rate increased the relative uncertainty in the calculated permeability, to such an extent that the measured dP values were close to the digital noise level (0.5 mBar).

As these values are not accurate and the effect becomes more pronounced at higher back pressure, it was chosen to exclude data points obtained above 10 bar.

Klinkenberg Correction

Linear regressions were performed for the plot of k_{app} vs. $1/P$ for each segment. Figure C.3 shows the resulting fits. For the Klinkenberg effect, a downward trend towards infinite pressure (to the left) is expected, which can also be seen.

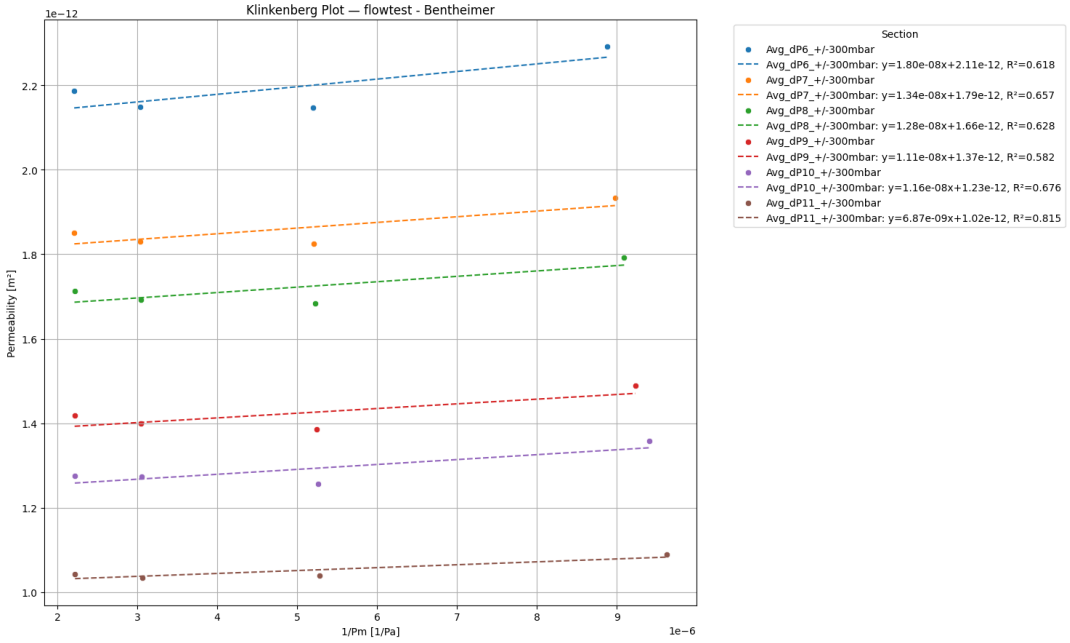

Figure C.3: Klinkenberg-corrected permeability estimates from multiple flow tests in the Bentheimer sandstone. Solid lines represent linear regression fits for each segment.

D

Part Lists and Experiment Tables

D.1. Back pressure cartridges

Table D.1: Specifications for IDEX Health & Science Back Pressure Regulator Cartridges. These models were tested during experiments. O-rings are replaced by CO_2 resistant variants.

Pressure Rating	Part Number	Color Code (Body/End-Cap)	Standard Wetted Materials
50 psi (3.4 bar)	P-760*	Tan / Gray	PEEK, ETFE, Perfluoroelastomer,
100 psi (6.9 bar)	P-763	Tan / Red	Gold-Plated Stainless Steel
250 psi (17 bar)	P-764	Tan / White	(Applies to all models listed)
500 psi (34 bar)	P-765	Tan / Green	
750 psi (52 bar)	P-795	Black / Blue	
1000 psi (69 bar)	P-796	Black / Green	

D.2. O-ring configurations

Table D.2: Comparative specifications of O-Rings for BPR Cartridges (Size AS568-008, 4.47 x 1.78 mm).

Material (Compound)	Origin / Compound Code	Hardness	Temp. Range (°C)	Characteristics & Suitability for CO_2 Service
NBR (Nitrile)	Eriks NBR 70	70 Shore A	-30 to +110	Standard material. Good mechanics, but vulnerable to swelling and explosive decompression with high-pressure CO_2.
EPDM	Eriks EPDM 70	70 Shore A	-45 to +150	Excellent weather and water resistance. Generally considered unsuitable for high-pressure CO_2 due to high gas permeation.
FKM (Viton®)[a]	Eriks Viton® 75	75 Shore A	-20 to +200	Excellent chemical resistance, low gas permeability. Good for CO_2 applications. A common upgrade from NBR.
FFKM (Kalrez®)[a]	Eriks Kalrez® 4079	75 Shore A	-15 to +315	Superior chemical and thermal resistance. Very low swelling and gas permeability. High-performance, premium option.
PTFE (Teflon®)[b]	**In-house Fabricated**	55 Shore D	-200 to +260	Virtually chemically inert. Non-elastomer, rigid material. Can prevent swelling but may offer poor sealing under thermal cycling.

[a] Viton® and Kalrez® are registered trademarks of The Chemours Company. FKM and FFKM are ASTM designations for fluoroelastomer and perfluoroelastomer materials, respectively. [b] PTFE is a rigid thermoplastic, not an elastomer, so its hardness is measured on the Shore D scale. It has no elastic memory, which can be a disadvantage for sealing dynamic surfaces.

D.3. Overview of experimental hardware settings

Table D.3: Overview of key experimental hardware.

Component	Manufacturer/Model	Function/Purpose in Setup	Key Specifications
High-Precision Pump	Vindum	Injects liquid CO_2 at precise, constant-volume flow rates into the system.	Used for delivering flow rates between 2.5 and 15 mL/min.
Core Holder Assembly	Custom-fabricated	Houses the 40 cm sandstone core. Designed for high-pressure conditions with PEEK insulation to minimize thermal losses.	400 mm length, 48 mm inner diameter, constructed of PEEK and stainless steel.
Differential Pressure Transmitter	Endress+Hauser Deltabar S PMD75	Measures the pressure drop across segments of the sandstone core.	Range: up to 3.3 bar; Max. working pressure: 160 bar.
Pressure Sensor	Keller PA-33X	Measures absolute pressure at various points along the core.	Range: -1 to 100 bar; Output: RS485 digital signal.
Outlet Back Pressure Regulator (Upgraded)	Equilibar EB1ULF1P	Maintains a stable downstream pressure, simulating reservoir conditions and controlling the expansion of CO_2.	Model: EB1ULF1P; Material: SS316/Polyamide.
Outlet Back Pressure Regulator (Original)	In-house Design	Original BPR used in early experiments. Replaced to improve pressure stability.	Constructed from PEEK. Showed reduced rigidity versus the Equilibar variant.
Hotplate	IKA KCH-MAG RCT	Heats the outlet back pressure regulator to prevent freezing of internal components during experiments.	Surface temperature adjustable up to 300°C.
System Control Panel	Custom-fabricated	Contains manual valves and a pressure gauge for routing fluids (gas, air) and visually monitoring system pressure.	Features a Swagelok pressure gauge (up to 210 bar).

D.4. Overview for specific hardware configurations for each experiment

Table D.4: Detailed overview of experimental runs: Bentheimer Sandstone Series (Experiments 1–12).

Experiment	Core Type	Injection Method	Inlet BPC	Outlet BPR	Primary Objective
Bentheimer Sandstone Permeability Tests					
permeability test	Bentheimer	Mass Flow Controller (Gas CO_2)	No	Original (PEEK)	Gas Permeability (Klinkenberg)
Bentheimer Sandstone Joule-Thomson Tests					
ex1	Bentheimer	Vindum Pump (Liquid CO_2)	Yes (30 bar)	Original (PEEK)	Basecase 5ml / System Development
ex2	Bentheimer	Vindum Pump (Liquid CO_2)	Yes (30 bar)	Original (PEEK)	increased flow 10ml
ex3	Bentheimer	Vindum Pump (Liquid CO_2)	Yes (30 bar)	Original (PEEK)	decreased flow 2.5ml
ex4	Bentheimer	Vindum Pump (Liquid CO_2)	Yes (30 bar)	Original (PEEK)	7.5ml flowrate
ex5	Bentheimer	Vindum Pump (Liquid CO_2)	Yes (60 bar)	Original (PEEK)	20 bar outlet BPR
ex6	Bentheimer	Vindum Pump (Liquid CO_2)	Yes (37 bar)	Original (PEEK)	35 bar outlet BPR
ex7	Bentheimer	Vindum Pump (Liquid CO_2)	Yes (30 bar)	Original (PEEK)	47.5 bar outlet BPR
ex8	Bentheimer	Vindum Pump (Liquid CO_2)	Yes (37 bar)	Original (PEEK)	34 bar outlet BPR
ex8.5	Bentheimer	Vindum Pump (Liquid CO_2)	Yes (37 bar)	Upgraded (Equilibar)	new BPR test
ex9	Bentheimer	Vindum Pump (Liquid CO_2)	Yes (37 bar)	Upgraded (Equilibar)	repeat ex6
ex10	Bentheimer	Vindum Pump (Liquid CO_2)	Yes (37 bar)	Upgraded (Equilibar)	8.5ml inj
ex11	Bentheimer	Vindum Pump (Liquid CO_2)	Yes (37 bar)	Upgraded (Equilibar)	12.5ml inj
ex12	Bentheimer	Vindum Pump (Liquid CO_2)	Yes (37 bar)	Upgraded (Equilibar)	stability tests

Table D.5: Detailed overview of experimental runs: Bentheimer Sandstone (Experiments 13–14) and Kentucky Sandstone Series.

Experiment	Core Type	Injection Method	Inlet BPC	Outlet BPR	Primary Objective
ex13	Bentheimer	Vindum Pump (Liquid CO_2)	Yes (Optimized w/ Teflon O-ring 50 bar)	Upgraded (Equilibar)	high flow, low BPR
ex14	Bentheimer	Vindum Pump (Liquid CO_2)	Yes (Optimized w/ Teflon O-ring 50 bar)	Upgraded (Equilibar)	ex13, rotated 135 degrees
			Kentucky Sandstone Permeability Tests		
flowtest	Kentucky	Mass Flow Controller (Gas CO_2)	No	Upgraded (Equilibar)	Gas Permeability (Klinkenberg)
			Kentucky Sandstone Joule-Thomson Tests		
ex15	Kentucky	Mass Flow Controller (Gas-phase CO_2)	No	Upgraded (Equilibar)	gas injection
ex16	Kentucky	Vindum Pump (Liquid CO_2)	No	Upgraded (Equilibar)	High BPR (45 bar)
ex17	Kentucky	Vindum Pump (Liquid CO_2)	No	Upgraded (Equilibar)	reduction in BPR (20 bar)
ex18	Kentucky	Vindum Pump (Liquid CO_2)	No	Upgraded (Equilibar)	Faster injection (7ml)
ex19	Kentucky	Vindum Pump (Liquid CO_2)	No	Upgraded (Equilibar)	slower injection (3ml)

D.5. Experimental settings

Table D.6: Detailed experimental settings overview for all experiments

Experiment	Core Type	Injection Rate	Inlet BPC	Outlet BPR	Duration [s]	Injected Volume [ml]	Min. Temperature [°C]
Bentheimer Sandstone Experiments							
ex1	Bentheimer	5 ml/min	30 bar	38.5 bar	6079	506.6	7.114
ex2	Bentheimer	10 ml/min	30 bar	38.5 bar	1797	299.5	8.697
ex3	Bentheimer	2.5 ml/min	30 bar	38.5 bar	18028	751.2	9.902
ex4	Bentheimer	7.5 ml/min	30 bar	38.5 bar	3684	460.5	6.564
ex5	Bentheimer	5 ml/min	60 bar	20 bar	2782	231.8	0.957
ex6	Bentheimer	10 ml/min	37 bar	35 bar	3682	613.7	4.947
ex7	Bentheimer	10 ml/min	30 bar	47.5 bar	1274	212.3	13.845
ex8	Bentheimer	7.5 ml/min	37 bar	34 bar	3778	472.3	1.893
ex8.5	Bentheimer	9 ml/min	37 bar	34 bar	1351	202.7	2.148
ex9	Bentheimer	10 ml/min	37 bar	35 bar	2873	478.8	3.885
ex10	Bentheimer	8.5 ml/min	37 bar	35 bar	4310	613.0	4.298
ex11	Bentheimer	12.5 ml/min	37 bar	35 bar	3800	791.7	5.687
ex12	Bentheimer	5 ml/min	37 bar	35 bar	14334	1194.5	8.915
ex13	Bentheimer	12.5 ml/min	50 bar	25 bar	4134	860.6	-5.104
ex14	Bentheimer	15 ml/min	50 bar	25 bar	3809	951.3	-4.479
Kentucky Sandstone Experiments							
ex15	Kentucky	88 gr/h	50 bar	0 bar	82000	2100	13
ex16	Kentucky	8 ml/min	0 bar	45 bar	6000	0[a]	13.4
ex17	Kentucky	5 ml/min	0 bar	20 bar	2792	232.7	-6.105
ex18	Kentucky	7 ml/min	0 bar	25 bar	2005	234.2	-1.594
ex19	Kentucky	3 ml/min	0 bar	17 bar	4817	240.9	5.444

[a] Injection stopped when the entire core was filled with liquid CO_2 before logging the test to see depressurizing response.

D.6. Experimental Data Plots

D.6.1. Bentheimer Sandstone Experiments

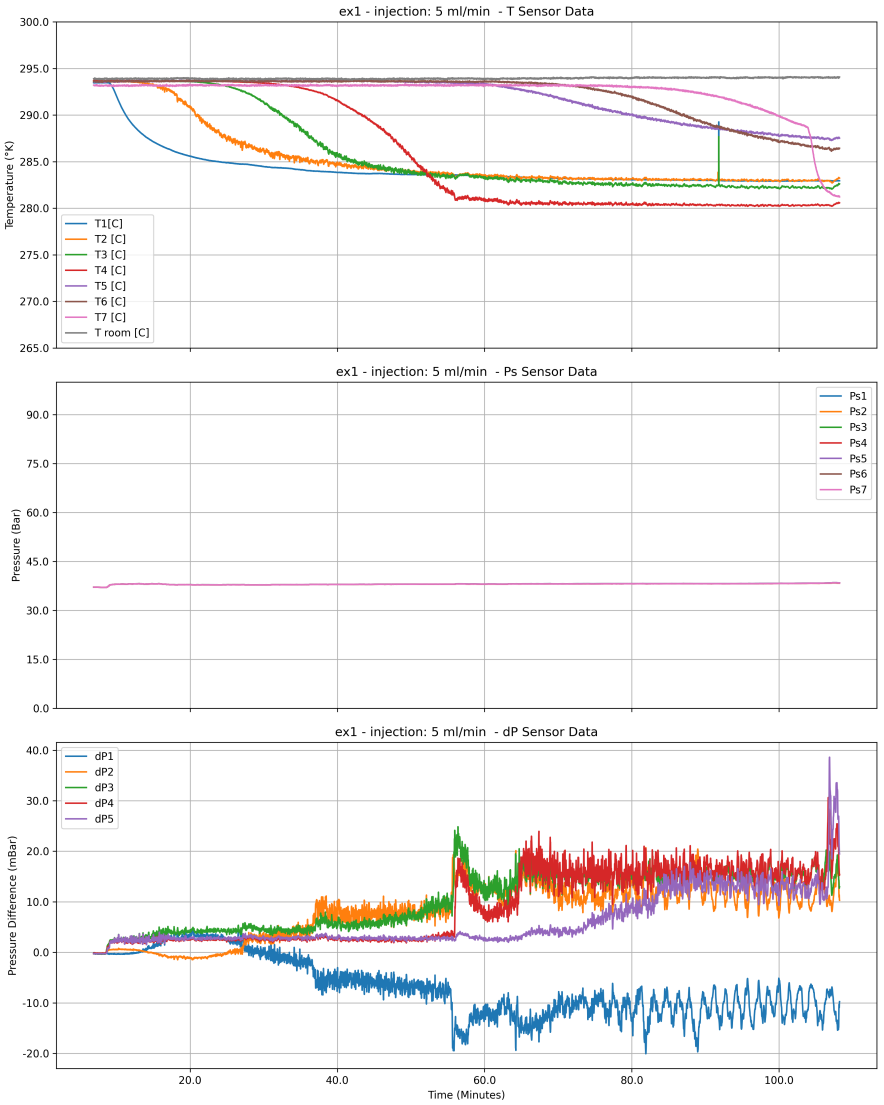

(a) Raw temperature, pressure, and ΔP data.

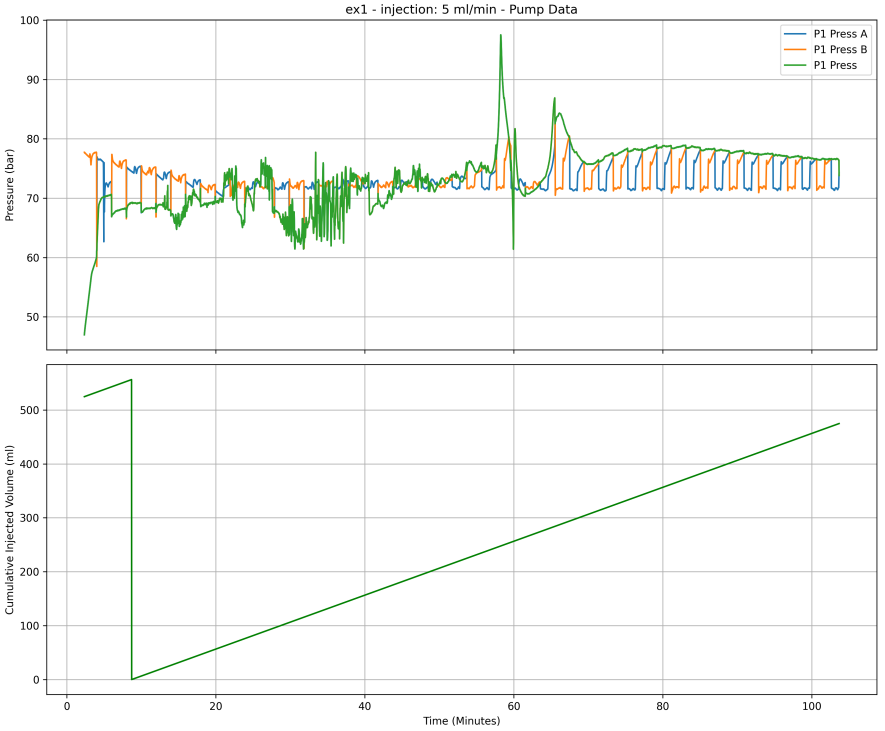

(b) Pump pressure trace.

Figure D.1: Experiment ex1: 5.0 mL/min liquid CO_2 injection, Inlet BPC: 30 bar, Outlet BPR: 38.5 bar. Min temperature: 7.11 Celsius. dP1 is negative due to an internal leak.

(a) Raw temperature, pressure, and ΔP data.

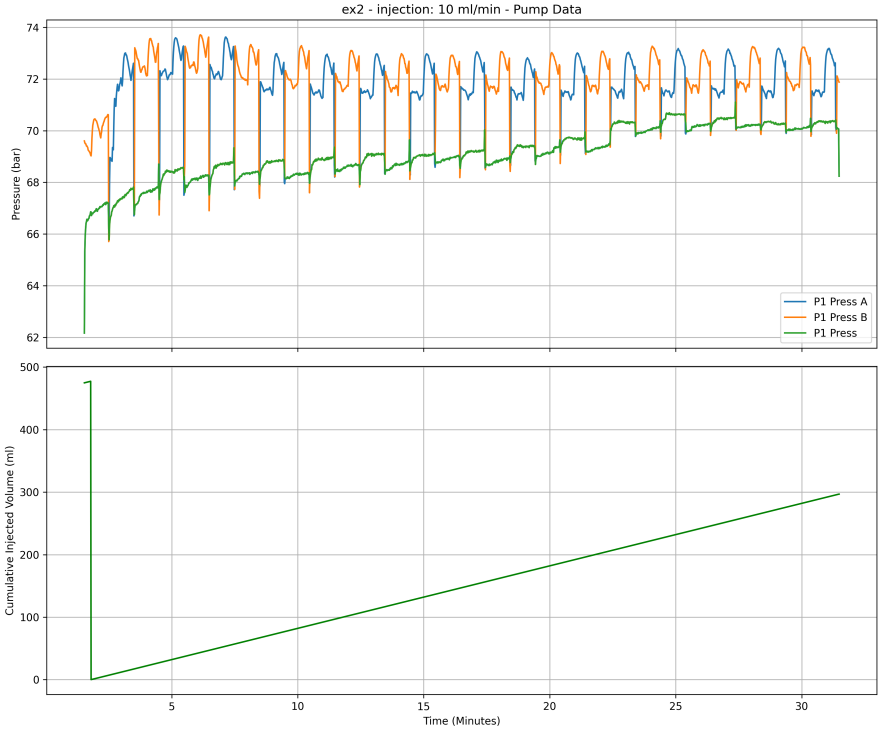

(b) Pump pressure trace.

Figure D.2: Experiment ex2: 10.0 mL/min liquid CO_2 injection, Inlet BPC: 30 bar, Outlet BPR: 38.5 bar. Min temperature: 8.70 Celsius.

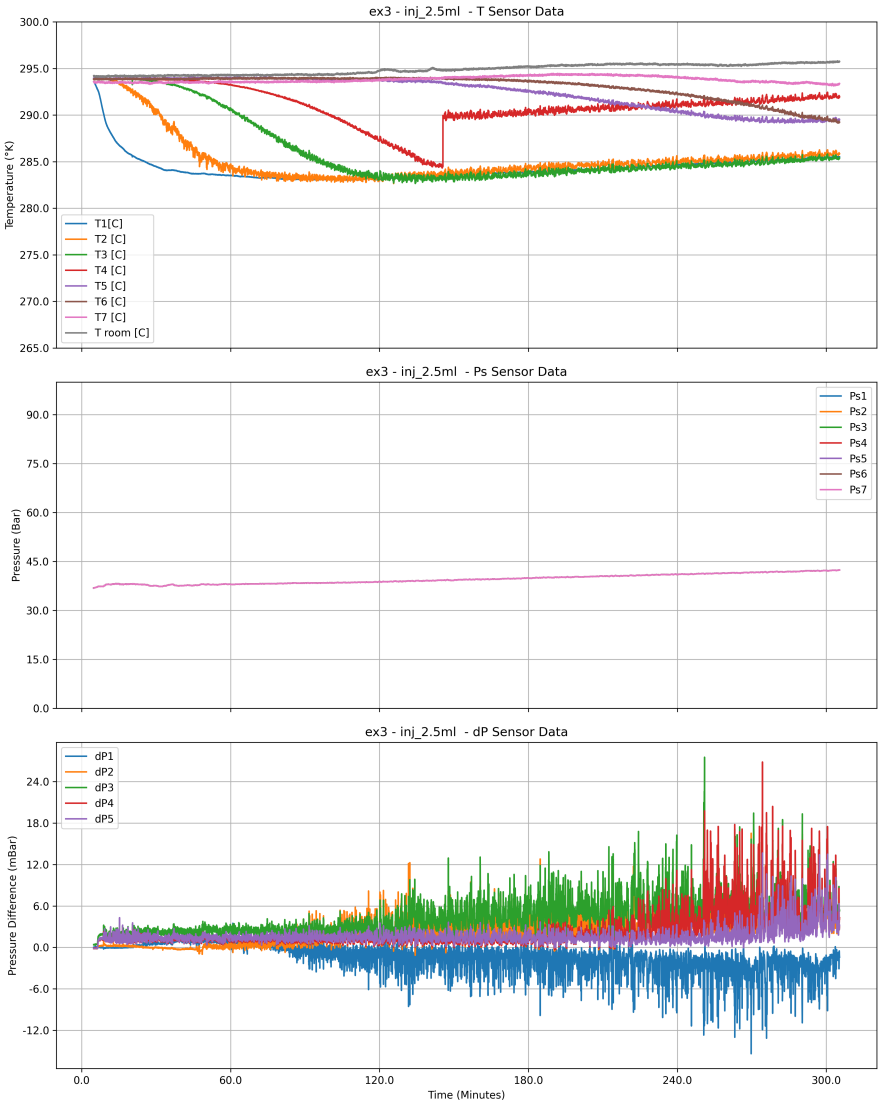

(a) Raw temperature, pressure, and ΔP data.

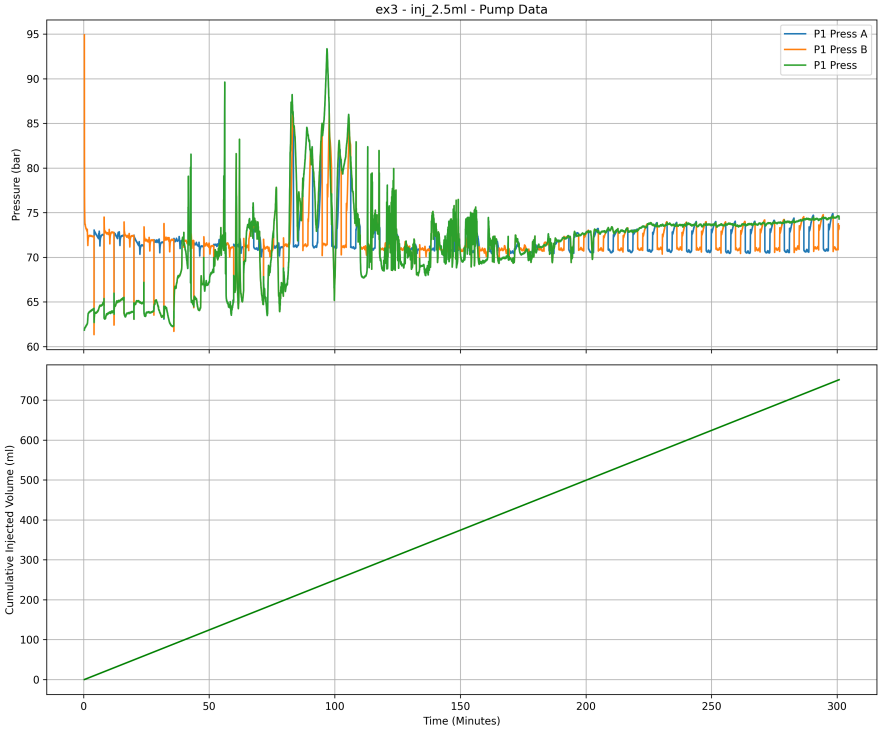

(b) Pump pressure trace.

Figure D.3: Experiment ex3: 2.5 mL/min liquid CO_2 injection, Inlet BPC: 30 bar, Outlet BPR: 38.5 bar. Min temperature: 9.90 Celsius. The sudden spike in T4 is an error caused by software.

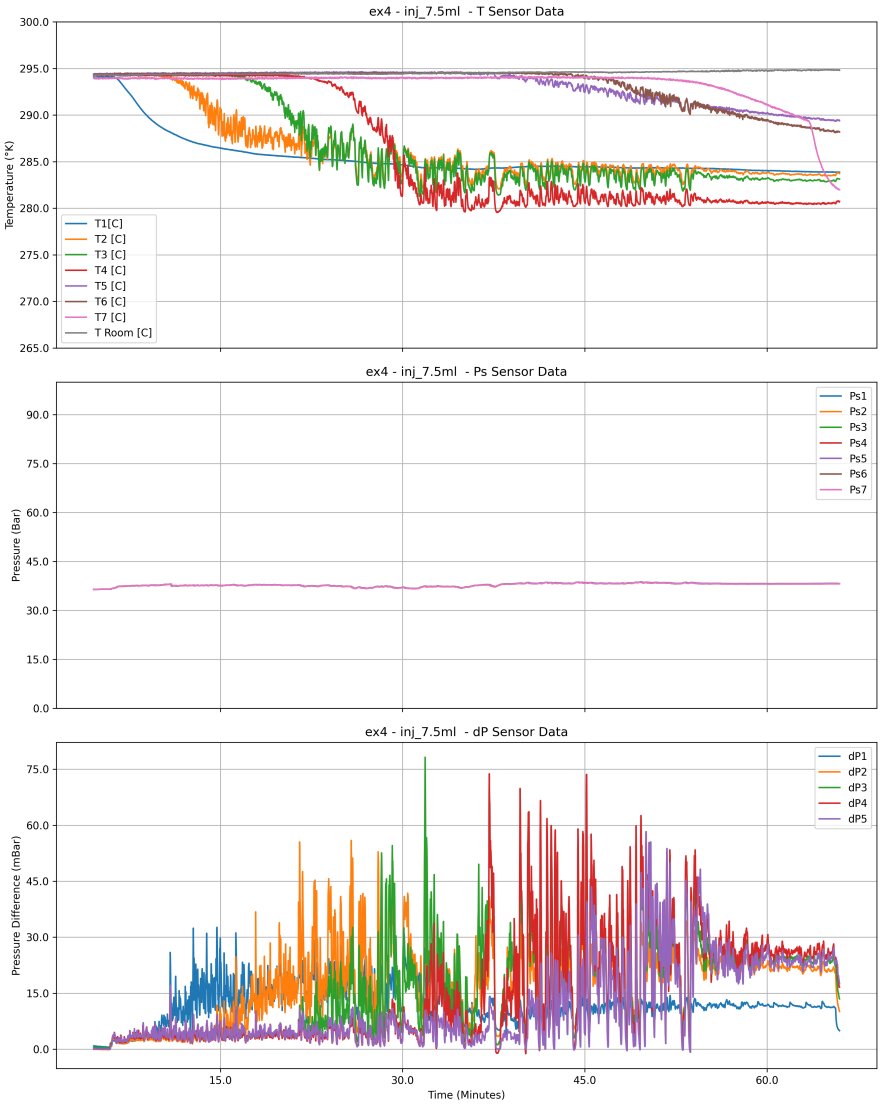

(a) Raw temperature, pressure, and ΔP data.

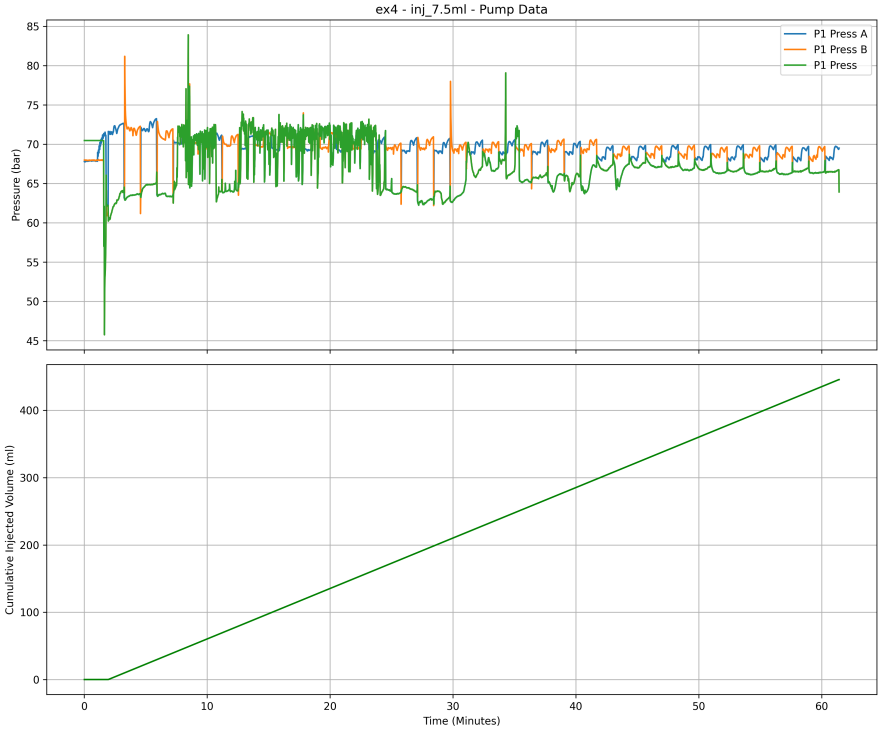

(b) Pump pressure trace.

Figure D.4: Experiment ex4: 7.5 mL/min liquid CO_2 injection, Inlet BPC: 30 bar, Outlet BPR: 38.5 bar. Min temperature: 6.56 Celsius.

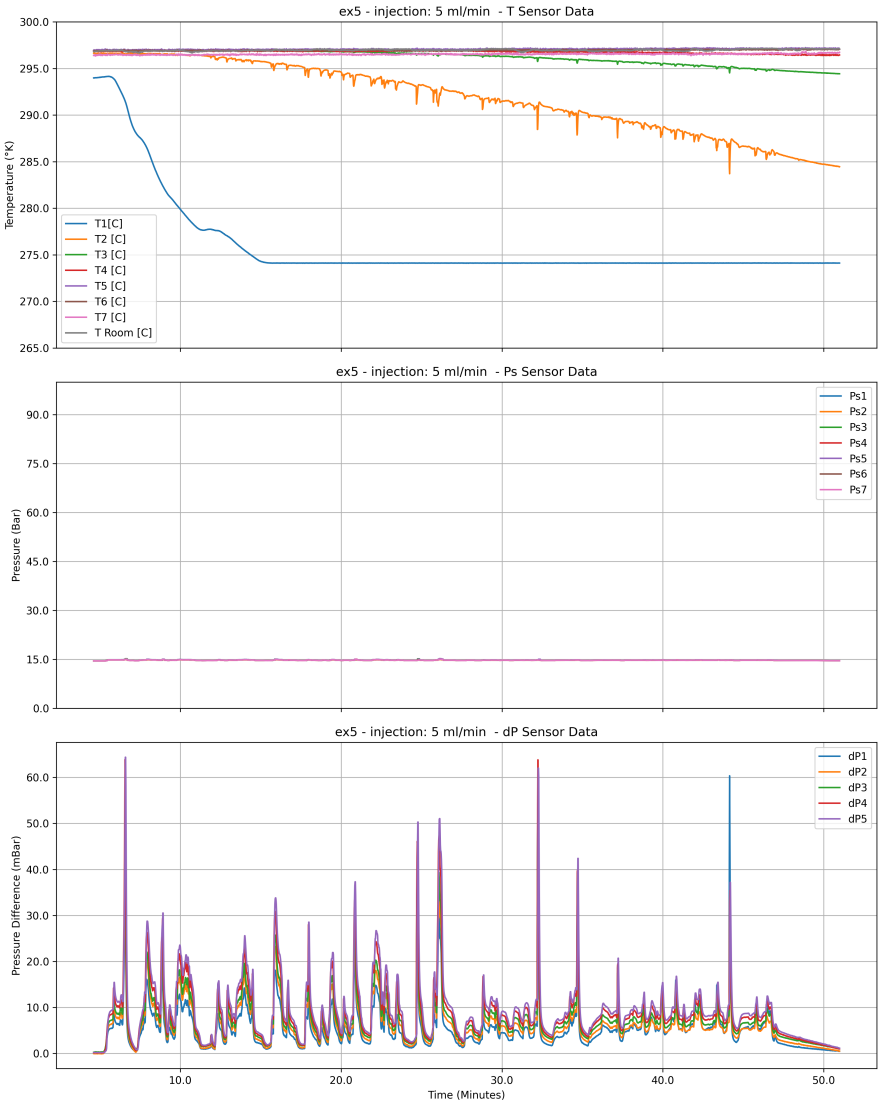

(a) Raw temperature, pressure, and ΔP data.

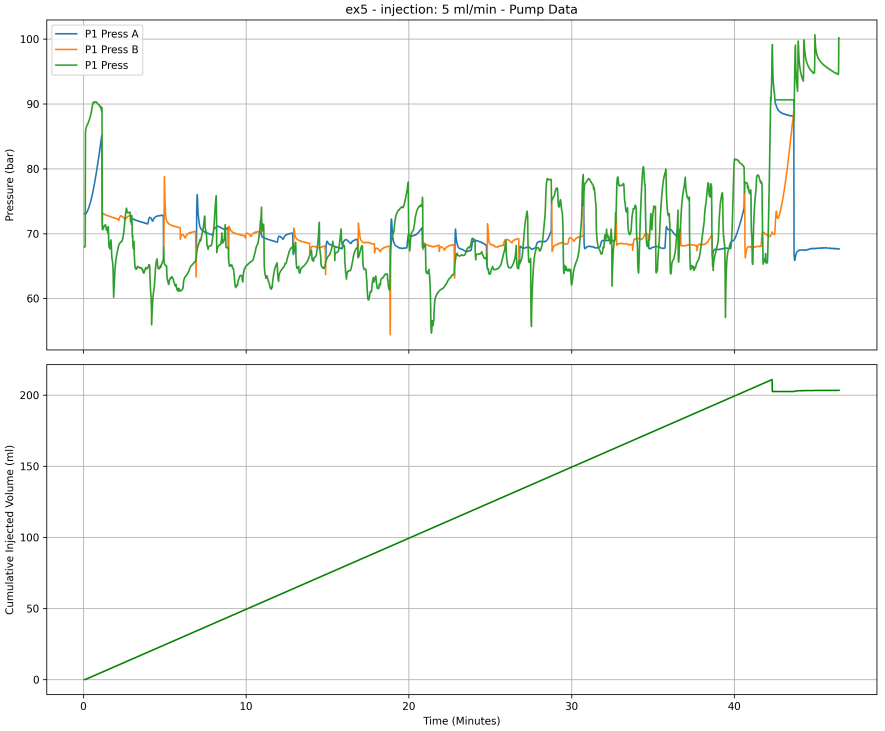

(b) Pump pressure trace.

Figure D.5: Experiment ex5: 5.0 mL/min liquid CO_2 injection, Inlet BPC: 60 bar, Outlet BPR: 20 bar. Min temperature: 0.96 Celsius. Temperature was limited to 274 K in software, sensors were replaced after.

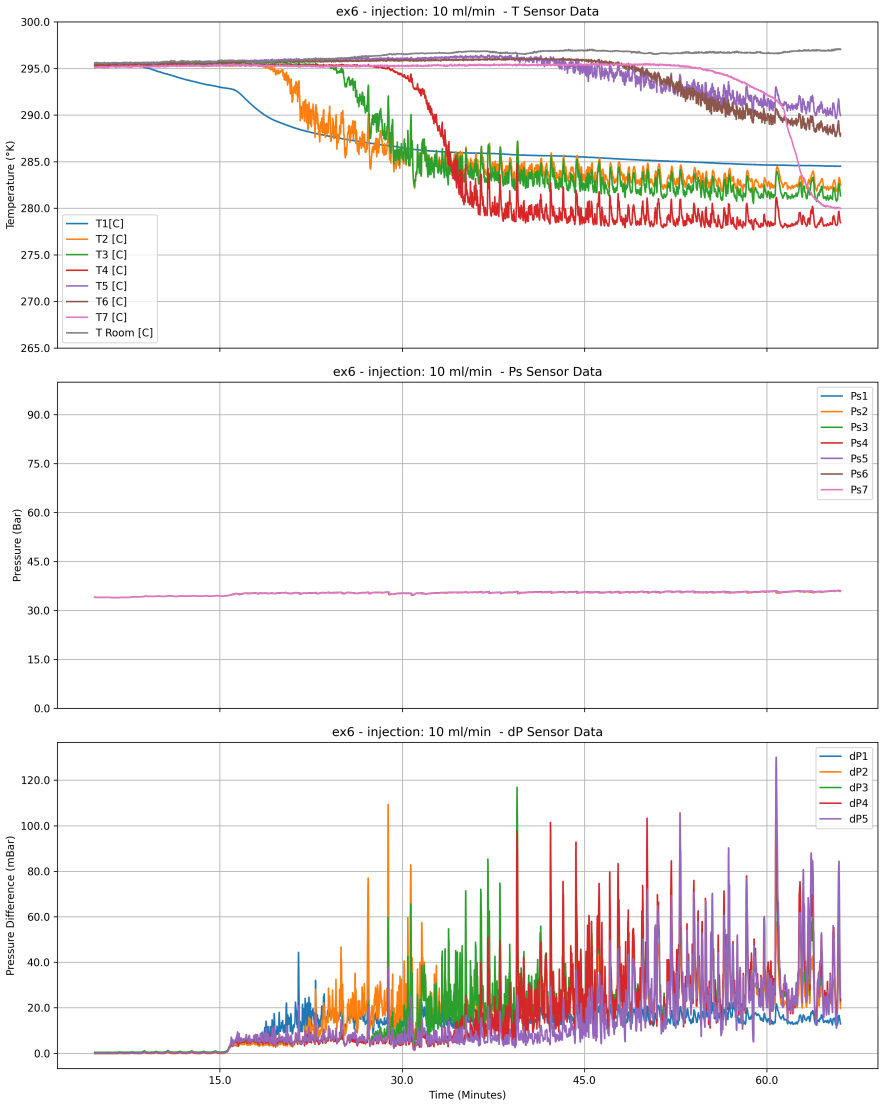

(a) Raw temperature, pressure, and ΔP data.

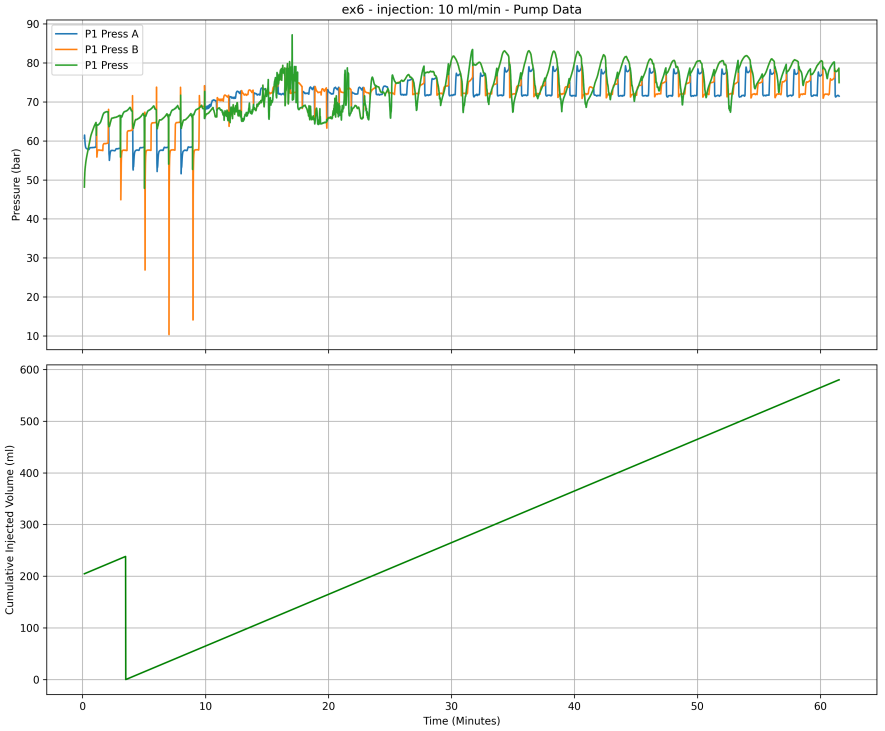

(b) Pump pressure trace.

Figure D.6: Experiment ex6: 10.0 mL/min liquid CO_2 injection, Inlet BPC: 37 bar, Outlet BPR: 35 bar. Min temperature: 4.95 Celsius.

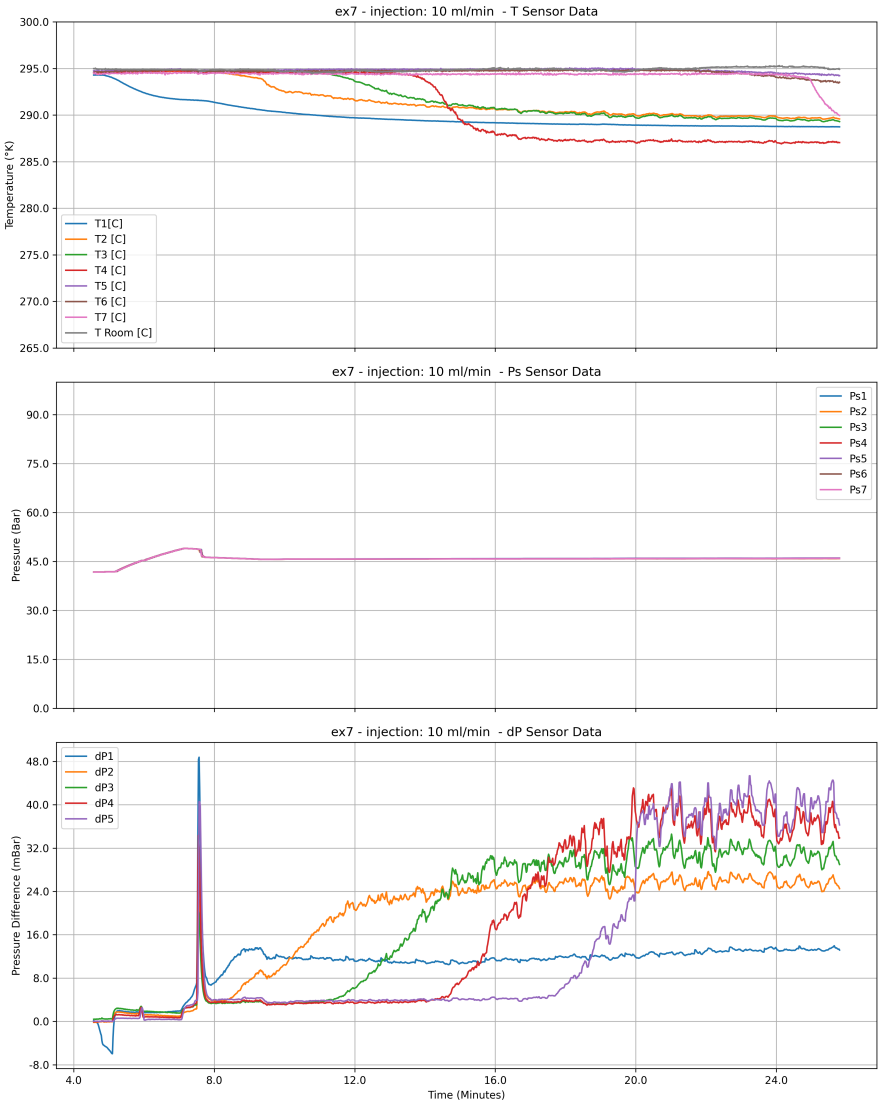

(a) Raw temperature, pressure, and ΔP data.

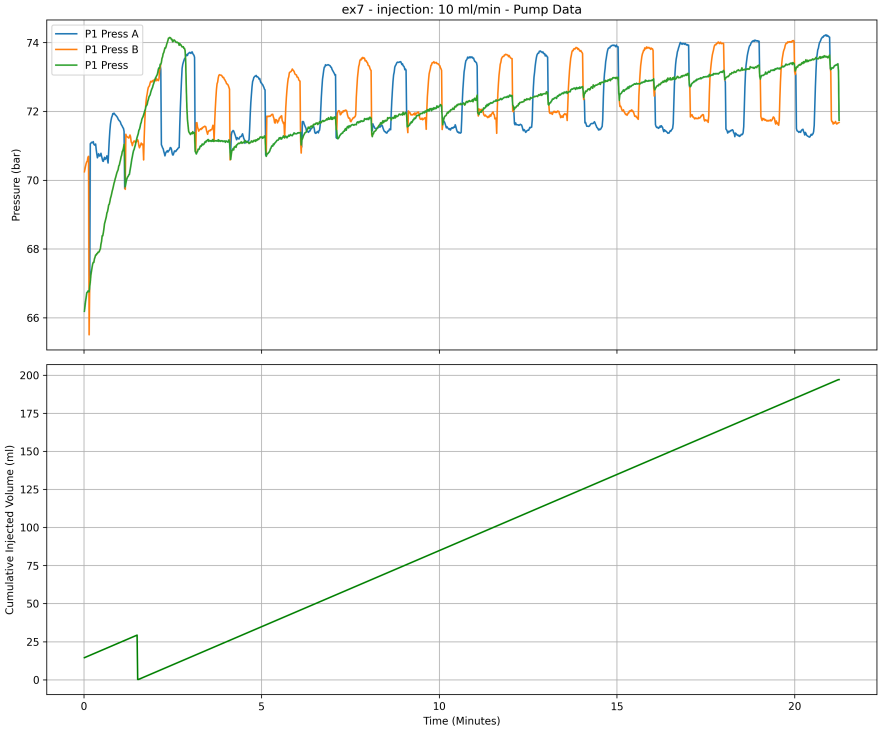

(b) Pump pressure trace.

Figure D.7: Experiment ex7: 10.0 mL/min liquid CO_2 injection, Inlet BPC: 30 bar, Outlet BPR: 47.5 bar. Min temperature: 13.85 Celsius.

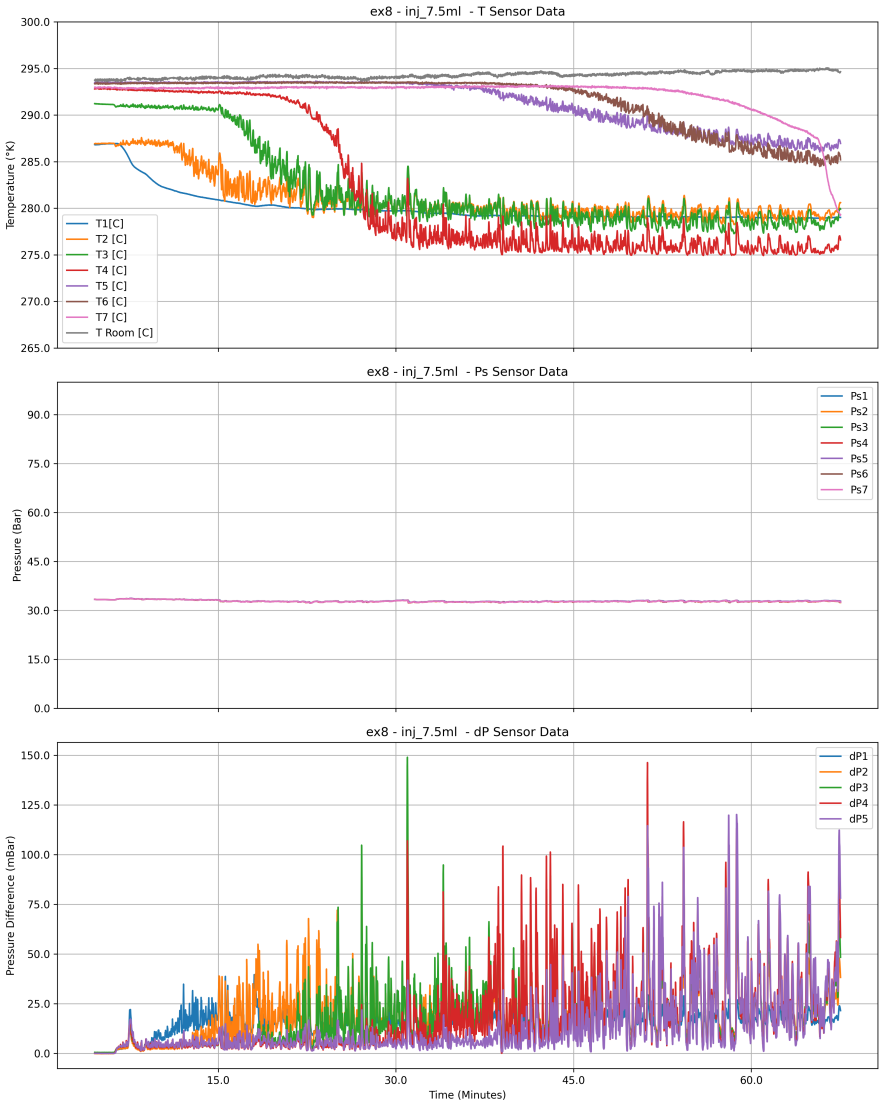

(a) Raw temperature, pressure, and ΔP data.

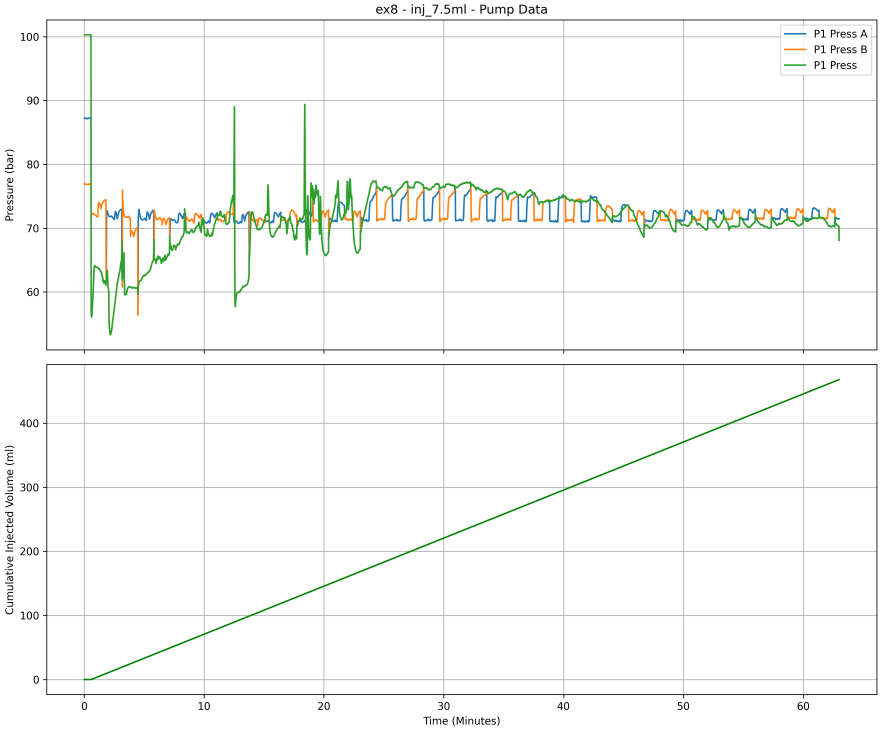

(b) Pump pressure trace.

Figure D.8: Experiment ex8: 7.5 mL/min liquid CO_2 injection, Inlet BPC: 37 bar, Outlet BPR: 34 bar. Min temperature: 1.89 Celsius.

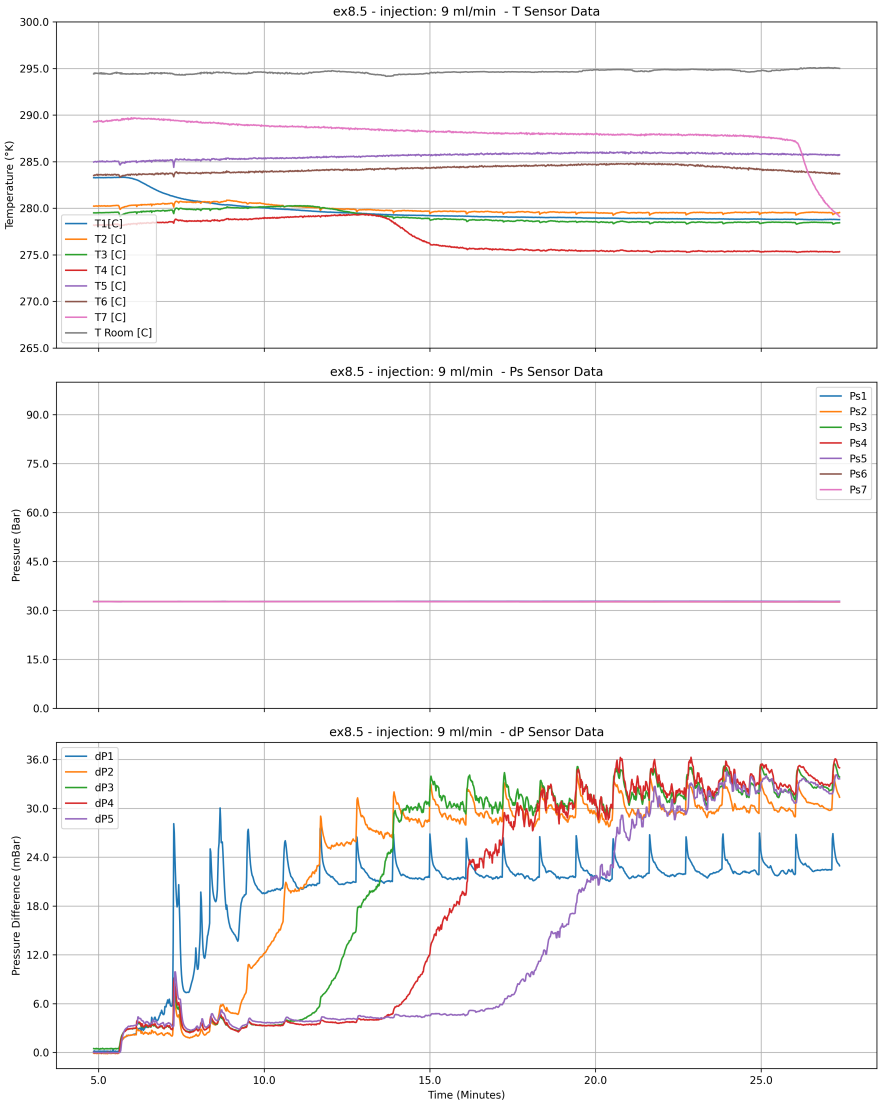

(a) Raw temperature, pressure, and ΔP data.

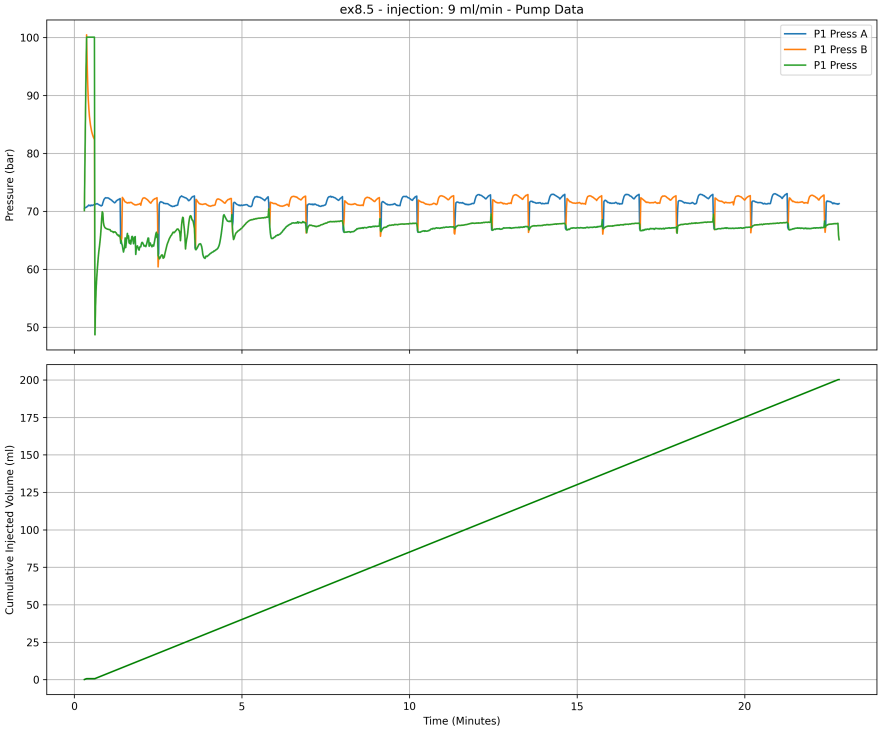

(b) Pump pressure trace.

Figure D.9: Experiment ex8.5: 9.0 mL/min liquid CO_2 injection, Inlet BPC: 37 bar, Outlet BPR: 34 bar. Min temperature: 2.15 Celsius.

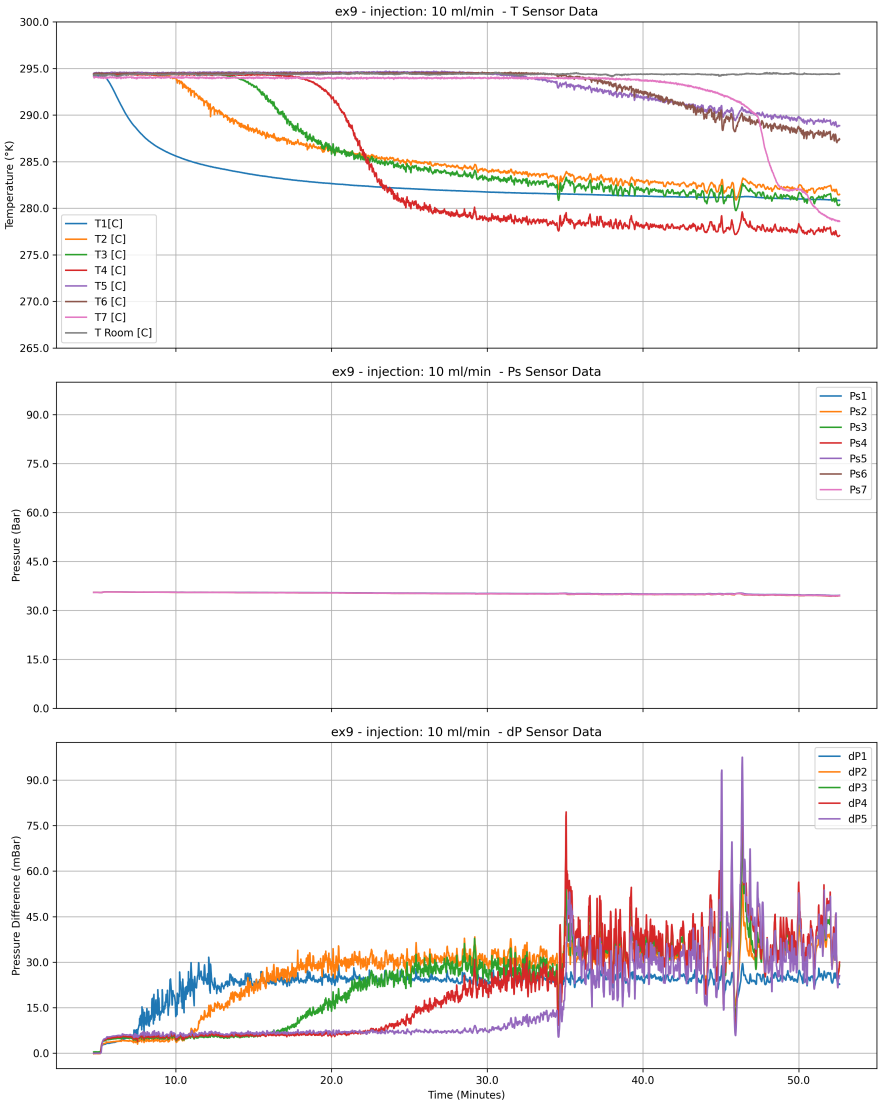

(a) Raw temperature, pressure, and ΔP data.

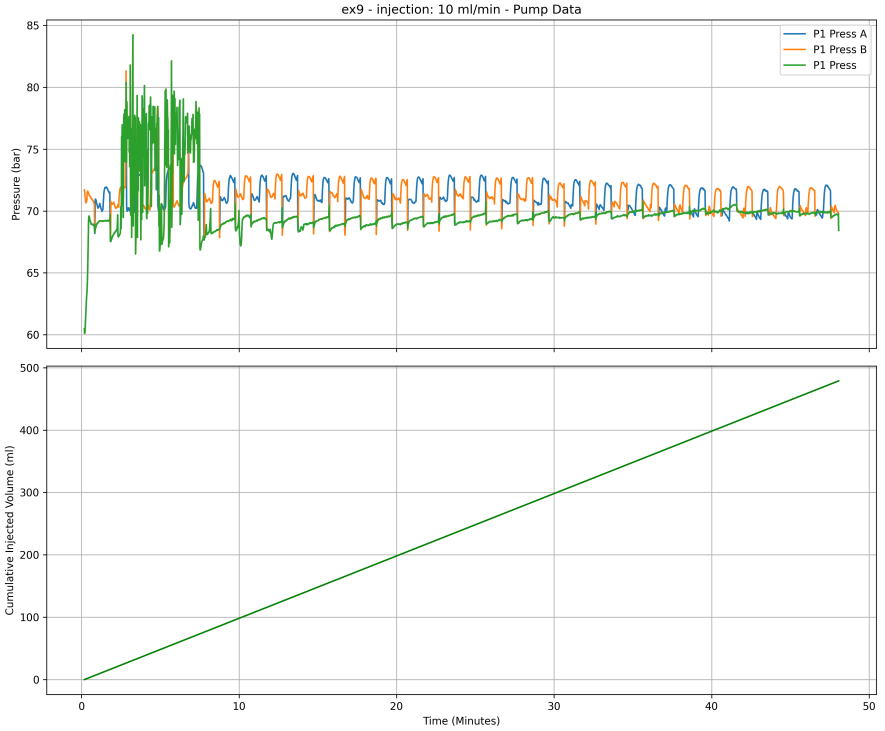

(b) Pump pressure trace.

Figure D.10: Experiment ex9: 10.0 mL/min liquid CO_2 injection, Inlet BPC: 37 bar, Outlet BPR: 35 bar. Min temperature: 3.89 Celsius.

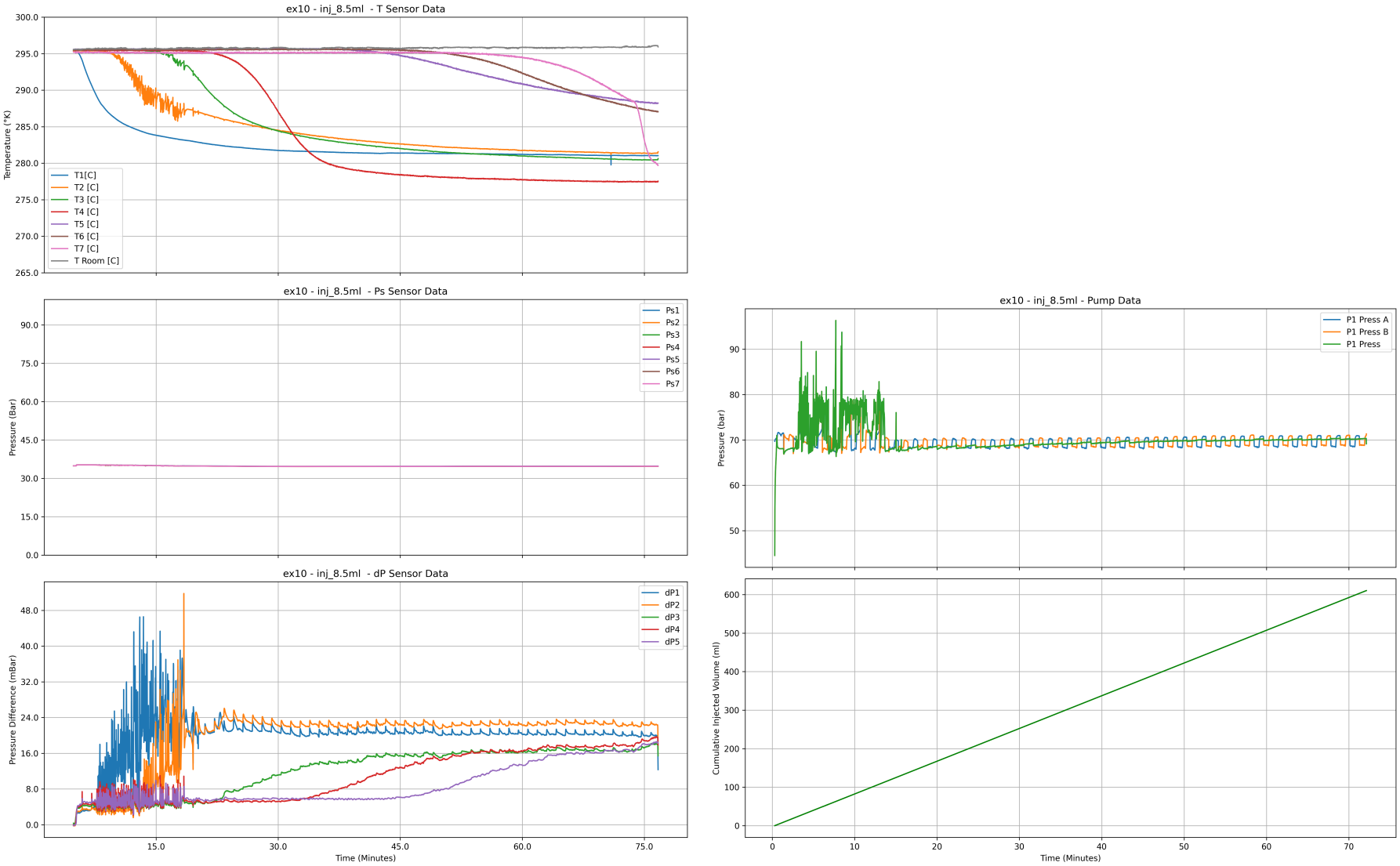

(a) Raw temperature, pressure, and ΔP data.

(b) Pump pressure trace.

Figure D.11: Experiment ex10: 8.5 mL/min liquid CO_2 injection, Inlet BPC: 37 bar, Outlet BPR: 35 bar. Min temperature: 4.30 Celsius.

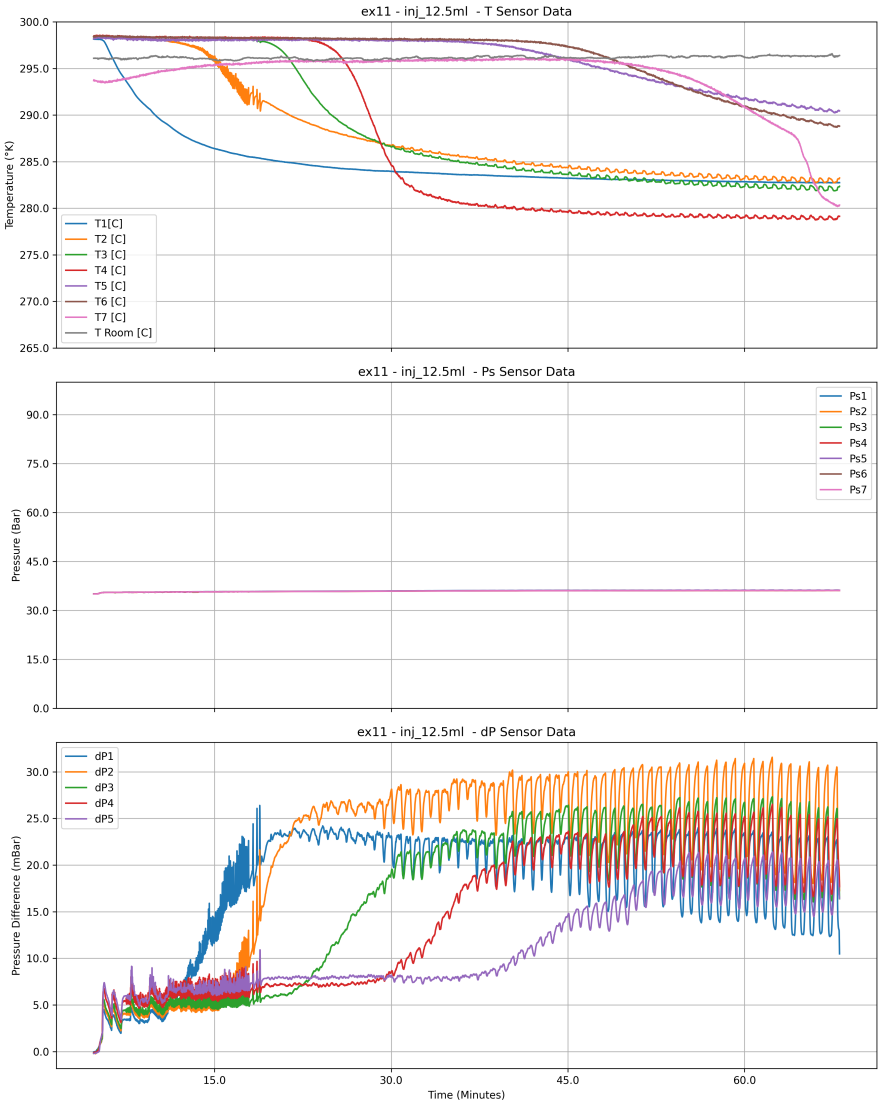

(a) Raw temperature, pressure, and ΔP data.

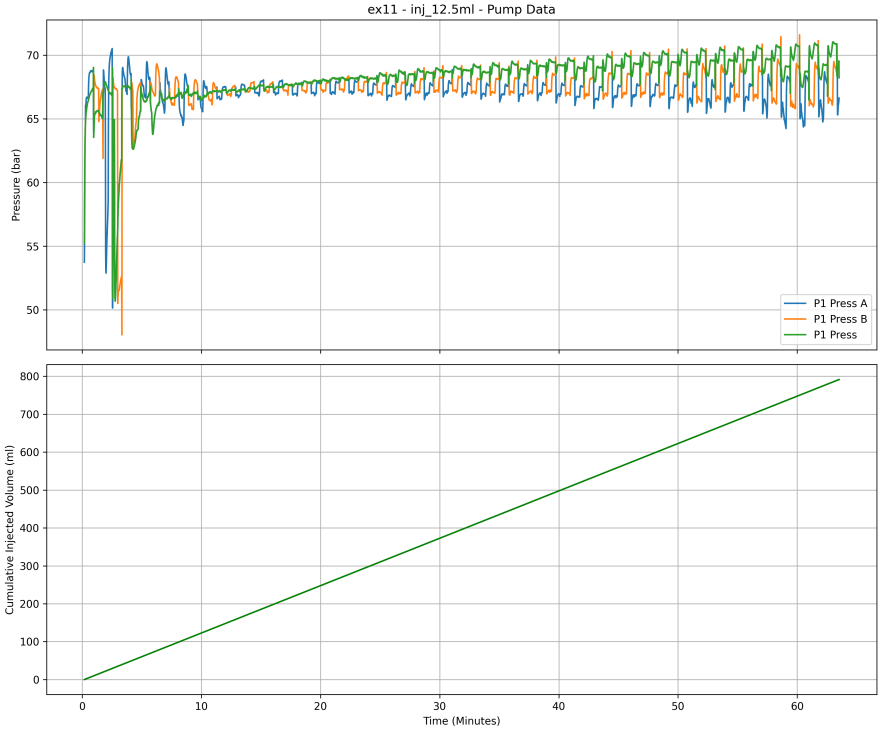

(b) Pump pressure trace.

Figure D.12: Experiment ex11: 12.5 mL/min liquid CO_2 injection, Inlet BPC: 37 bar, Outlet BPR: 35 bar. Min temperature: 5.69 Celsius.

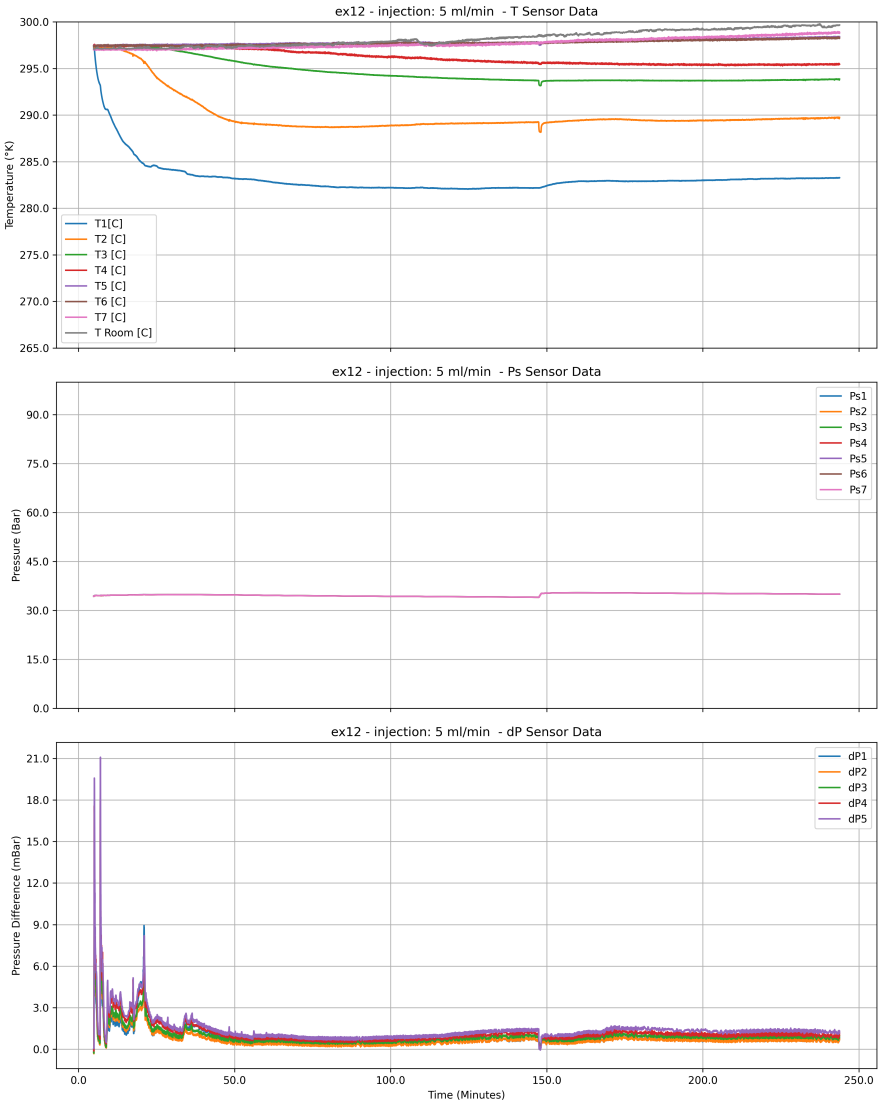

(a) Raw temperature, pressure, and ΔP data.

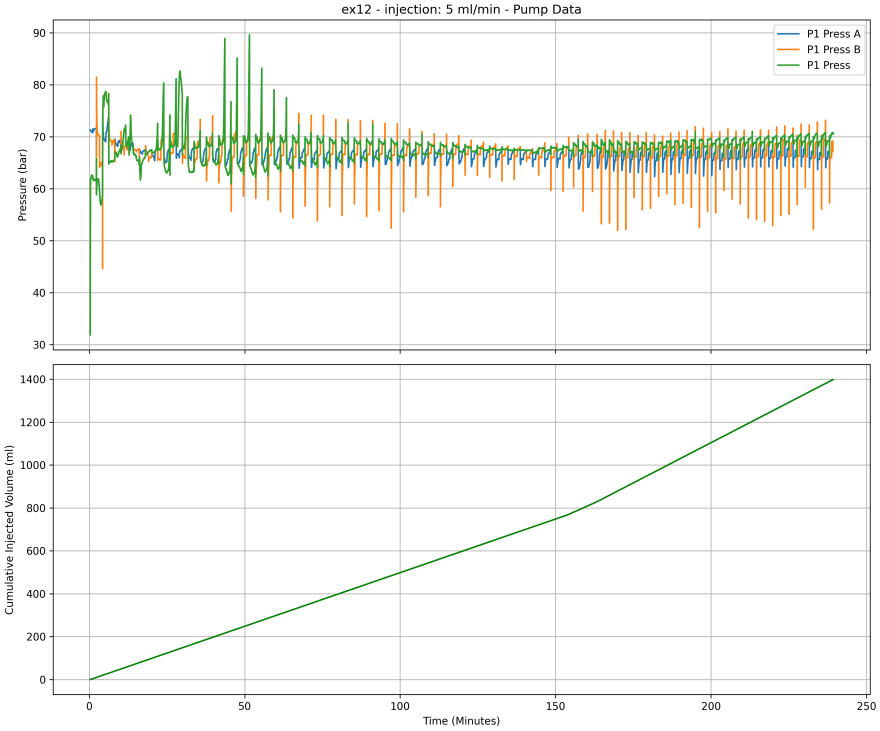

(b) Pump pressure trace.

Figure D.13: Experiment ex12: 5.0 mL/min liquid CO_2 injection, Inlet BPC: 37 bar, Outlet BPR: 35 bar. Min temperature: 8.92 Celsius.

D.6.2. Kentucky Sandstone Experiments

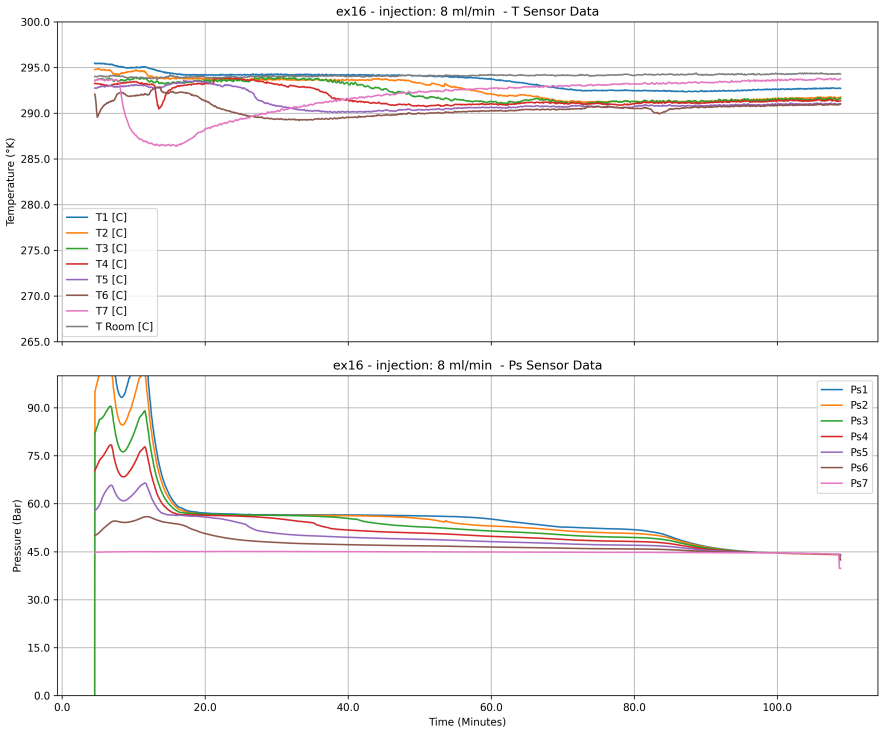

(a) Raw temperature, pressure, and ΔP data.

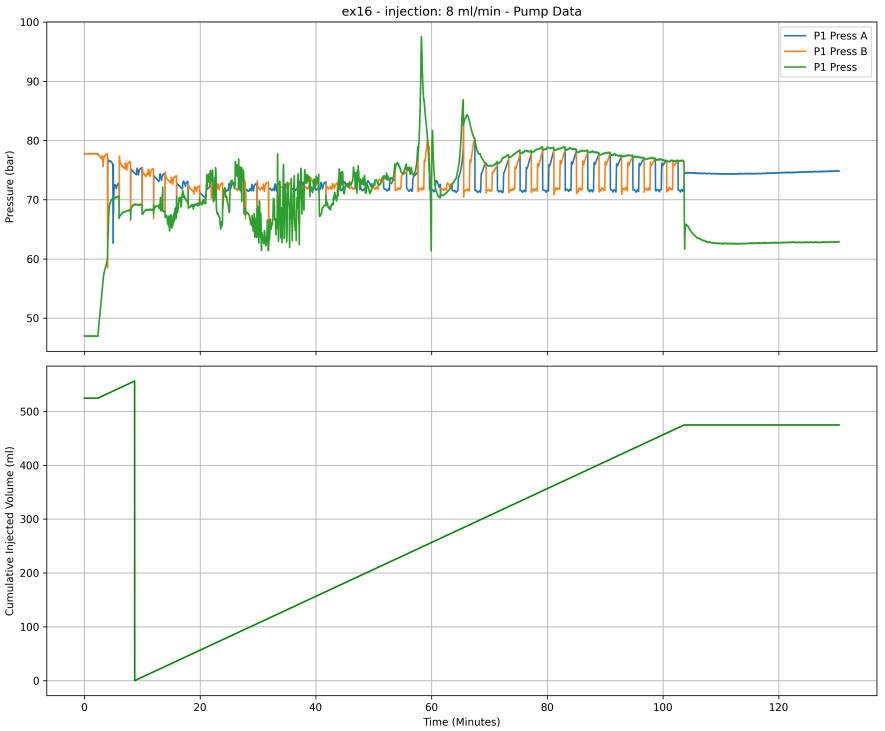

(b) Pump pressure trace.

Figure D.14: Experiment ex16: 8.0 mL/min liquid CO_2 injection, Inlet BPC: 0 bar, Outlet BPR: 45 bar. Min temperature: 13.4 Celsius.

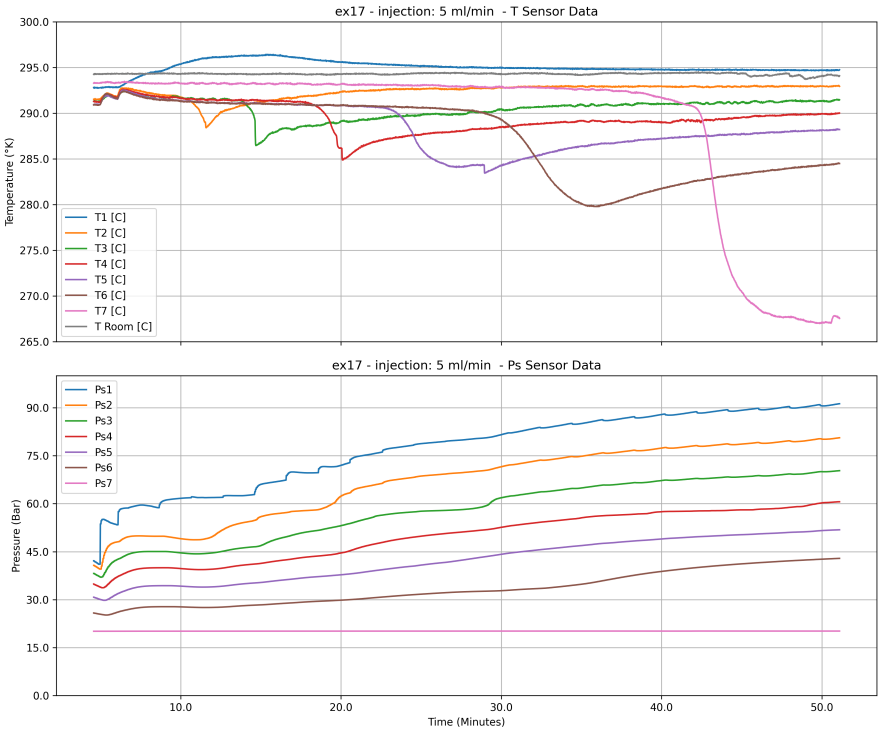

(a) Raw temperature, pressure, and ΔP data.

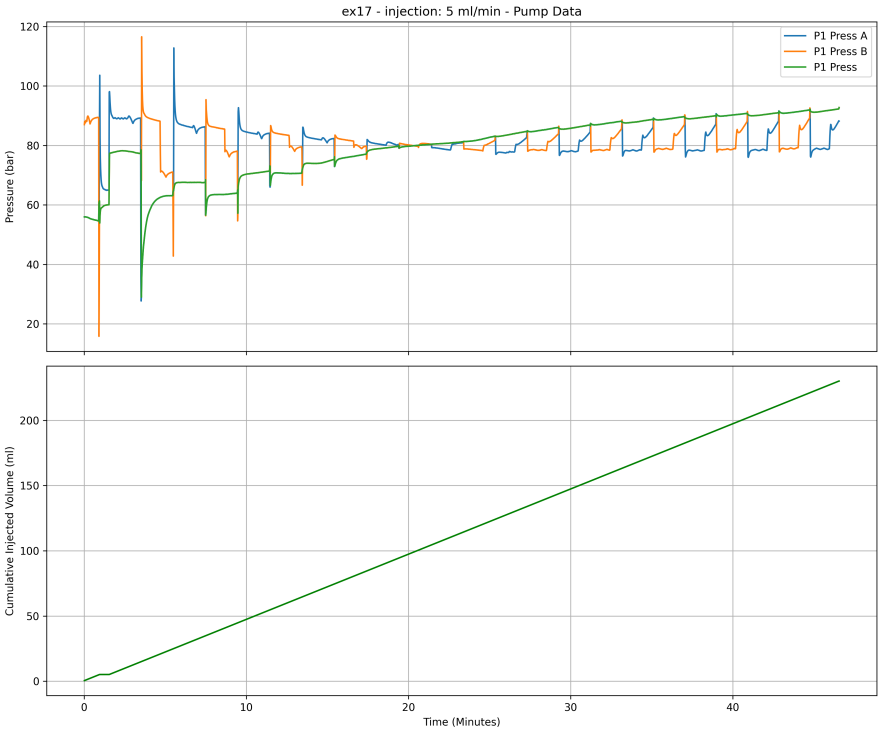

(b) Pump pressure trace.

Figure D.15: Experiment ex17: 5.0 mL/min liquid CO_2 injection, Inlet BPC: 0 bar, Outlet BPR: 20 bar. Min temperature: -6.11 Celsius.

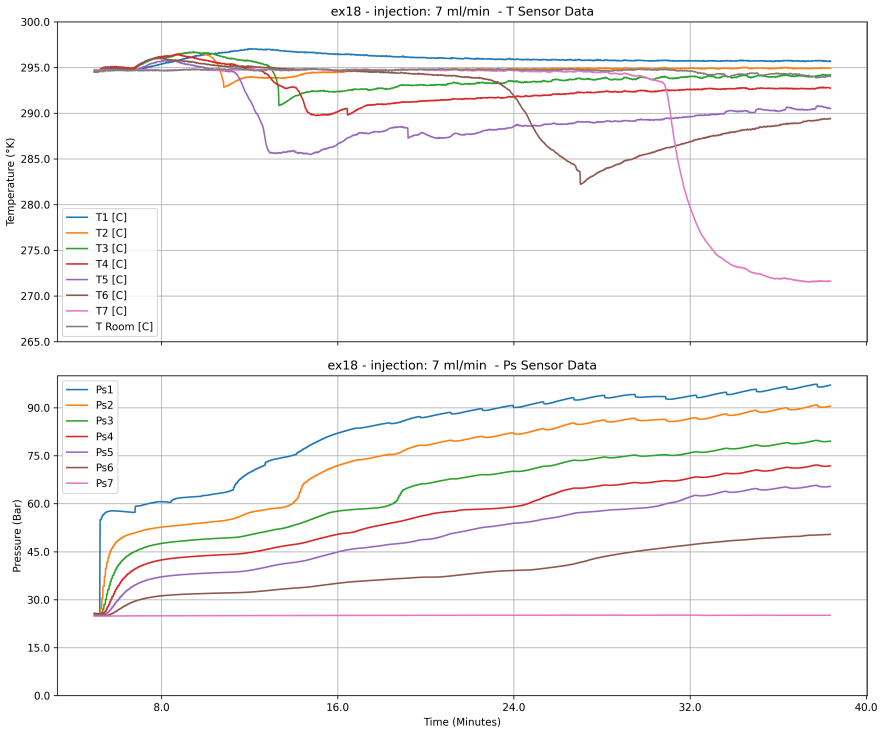

(a) Raw temperature, pressure, and ΔP data.

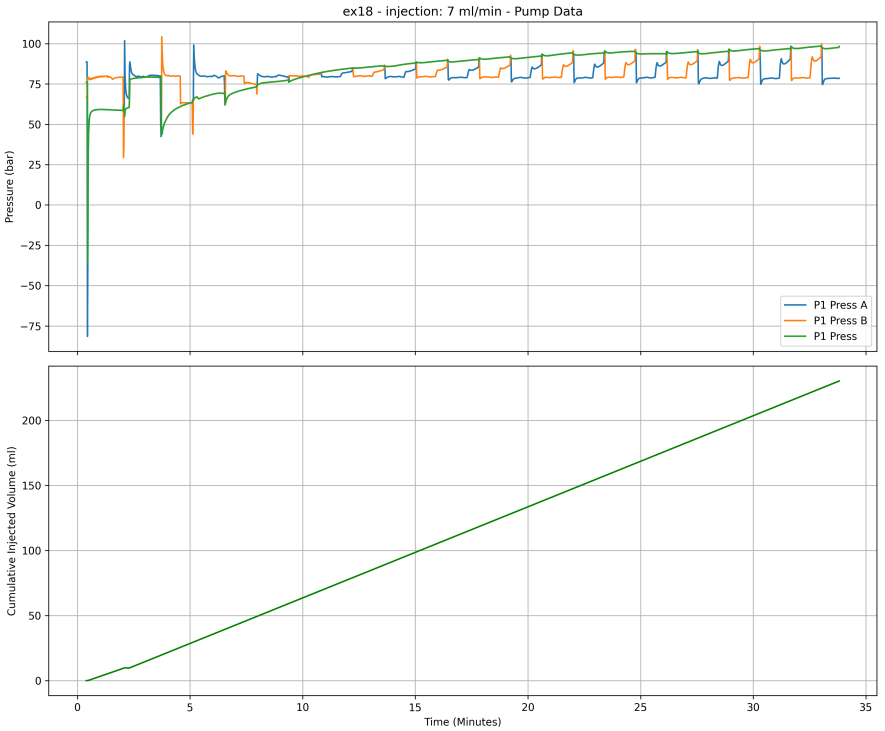

(b) Pump pressure trace.

Figure D.16: Experiment ex18: 7.0 mL/min liquid CO_2 injection, Inlet BPC: 0 bar, Outlet BPR: 25 bar. Min temperature: -1.59 Celsius.

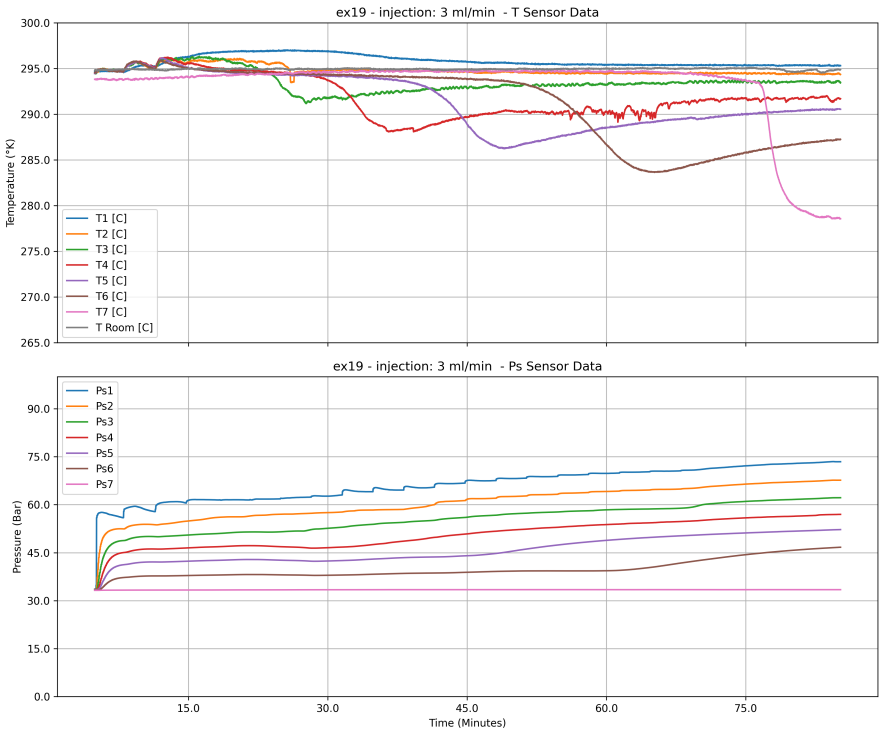

(a) Raw temperature, pressure, and ΔP data.

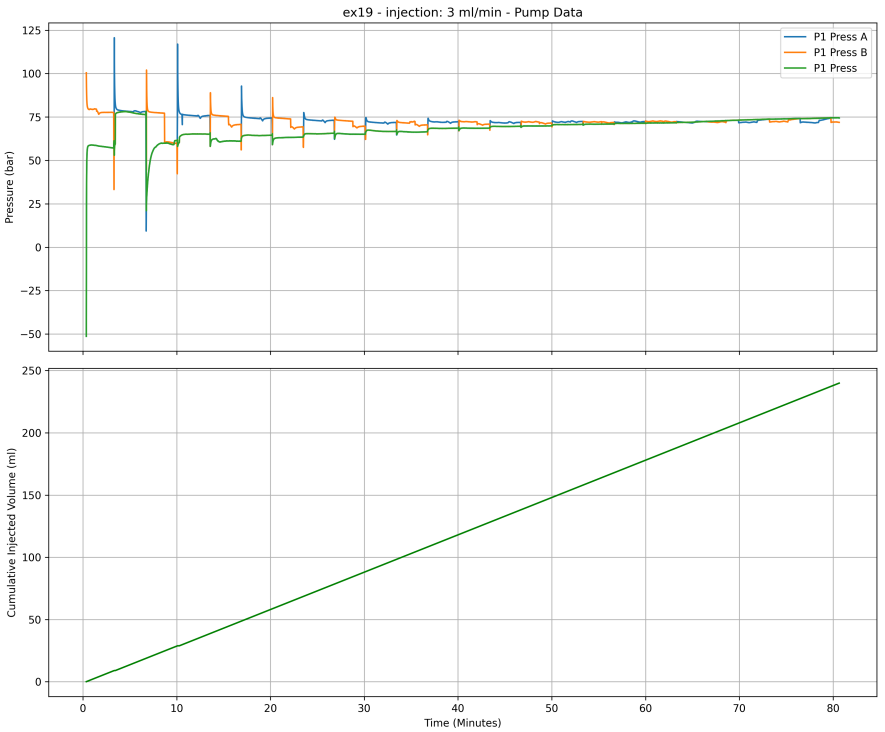

(b) Pump pressure trace.

Figure D.17: Experiment ex19: 3.0 mL/min liquid CO_2 injection, Inlet BPC: 0 bar, Outlet BPR: 17 bar. Min temperature: 5.44 Celsius.

D.6.3. Smoothed Sensor Data Plots

A moving average filter with a window size equivalent to 1 percent of the total experiment duration was applied to the raw signal. This smoothing technique suppresses high-frequency noise and large transient spikes, thereby enhancing the visibility of underlying trends. In particular, it facilitates the identification of abrupt signal transitions—often indicative of advancing liquid fronts within the porous medium.

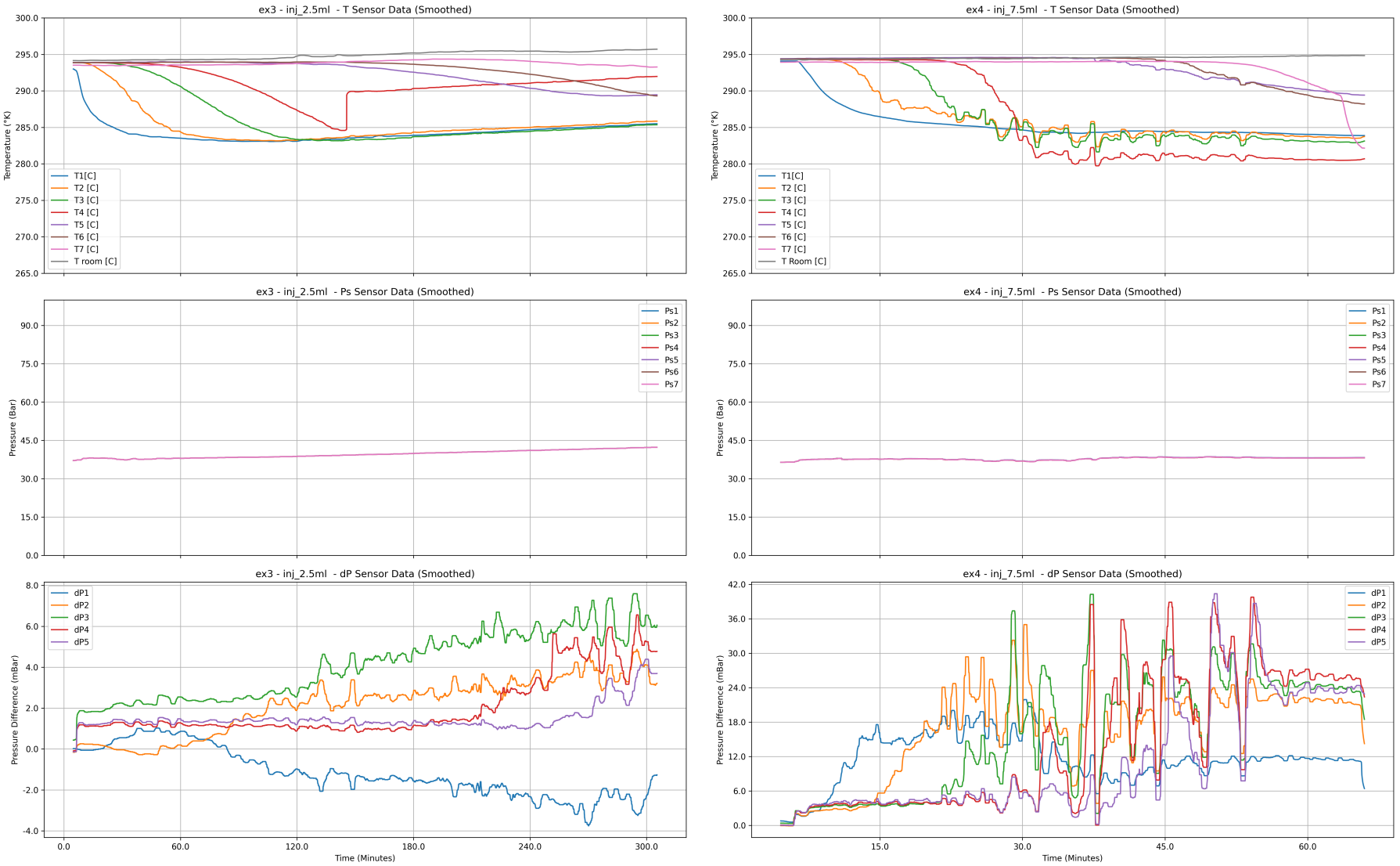

(a) Smoothed sensor data for Experiment ex3: 2.5 mL/min liquid CO_2 injection, Inlet BPC: 30 bar, Outlet BPR: 38.5 bar.

(b) Smoothed sensor data for Experiment ex4: 7.5 mL/min liquid CO_2 injection, Inlet BPC: 30 bar, Outlet BPR: 38.5 bar.

Figure D.18: Comparison of smoothed sensor data for experiments ex3 and ex4.

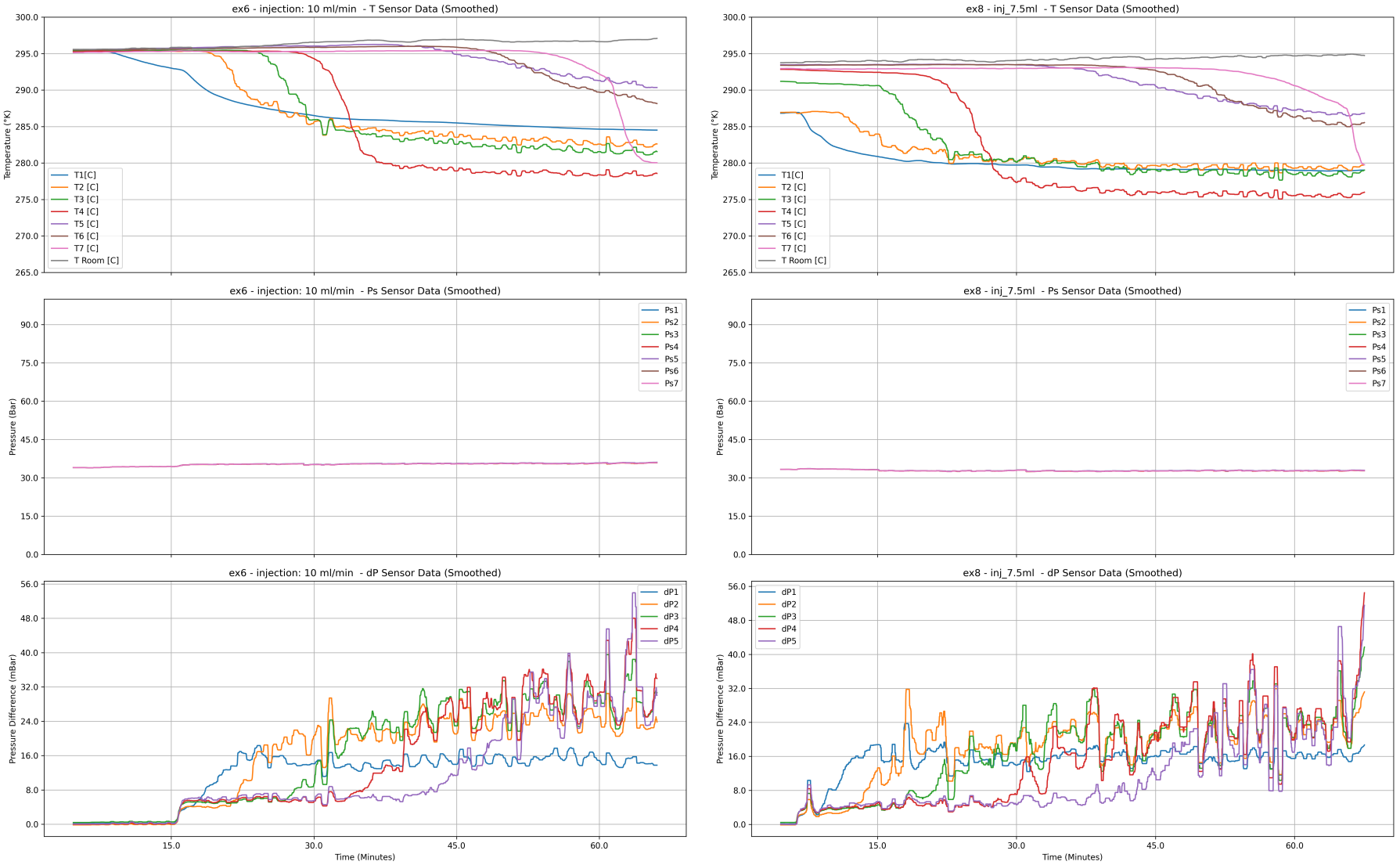

(a) Smoothed sensor data for Experiment ex6: 10.0 mL/min liquid CO_2 injection, Inlet BPC: 37 bar, Outlet BPR: 35 bar.

(b) Smoothed sensor data for Experiment ex8: 7.5 mL/min liquid CO_2 injection, Inlet BPC: 37 bar, Outlet BPR: 34 bar.

Figure D.19: Comparison of smoothed sensor data for experiments ex6 and ex8.

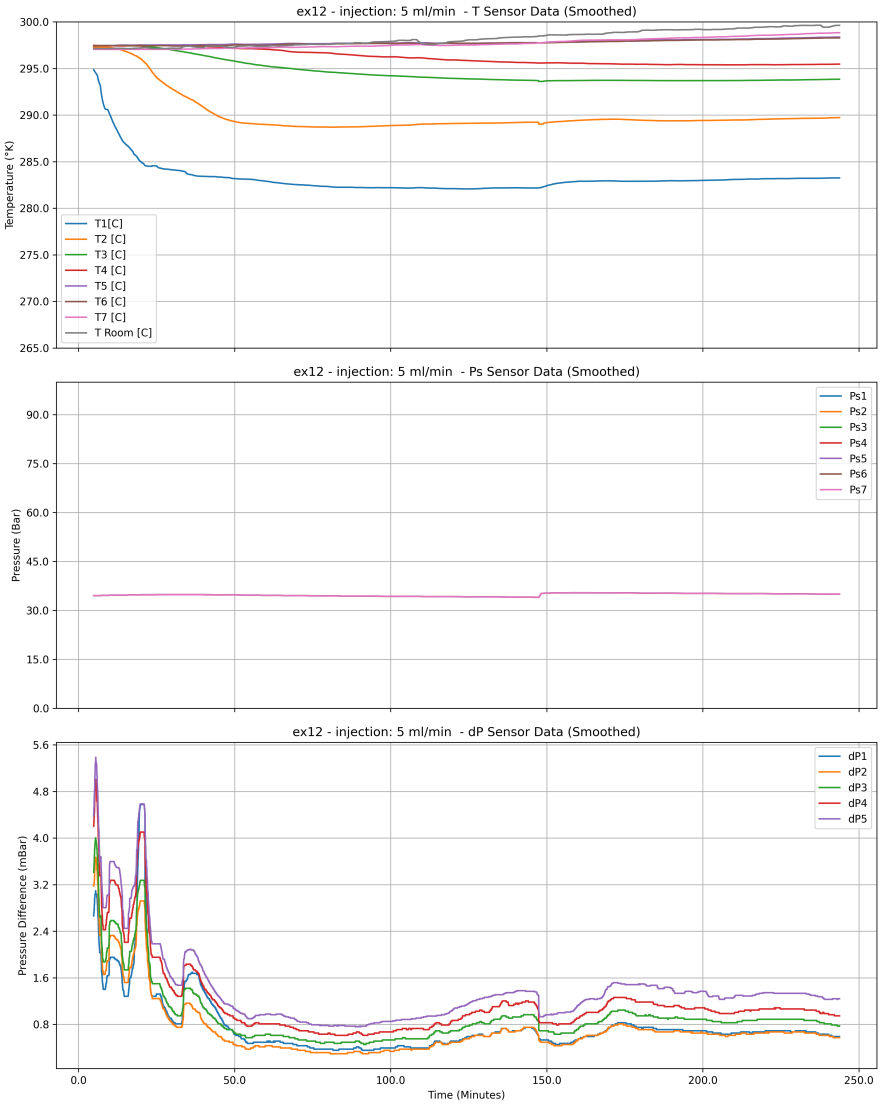

(a) Smoothed sensor data for Experiment ex12: 5.0 mL/min liquid CO_2 injection, Inlet BPC: 37 bar, Outlet BPR: 35 bar.

Figure D.20: Smoothed sensor data for experiment ex12, a long-duration stability test.

D.7. Bentheimer permeability calculations

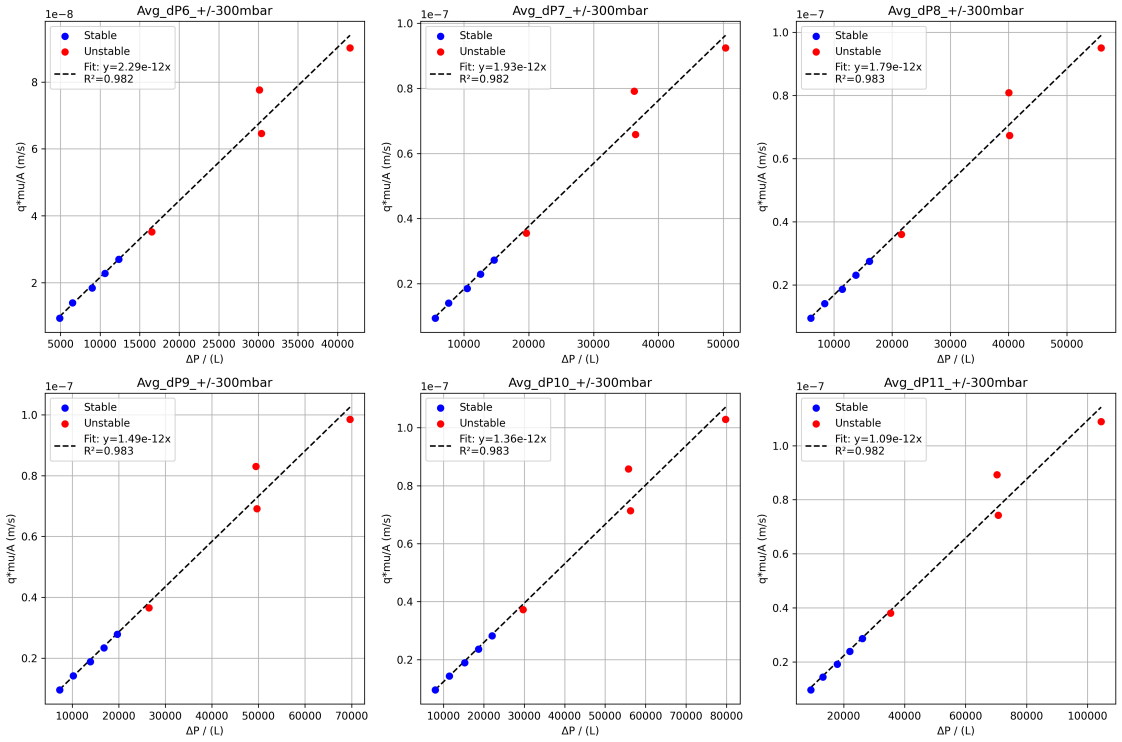

Figure D.21: Segment_fit_bp0.0_bentheimer

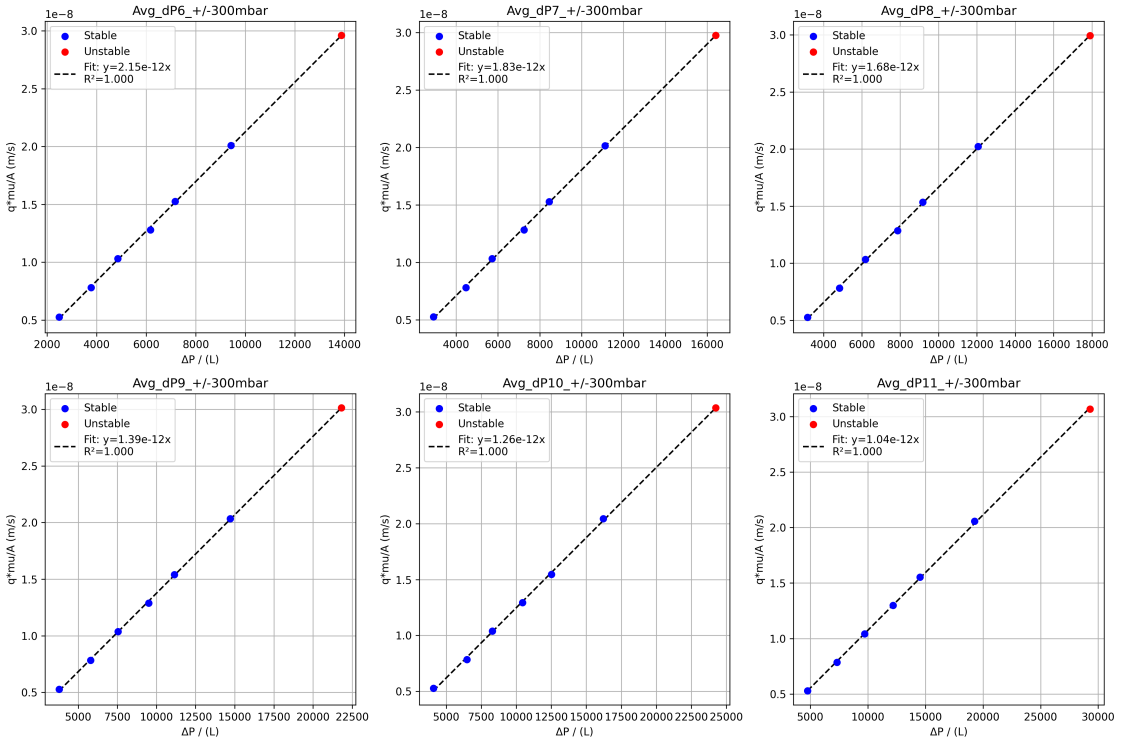

Figure D.22: Segment_fit_bp1.0_bentheimer

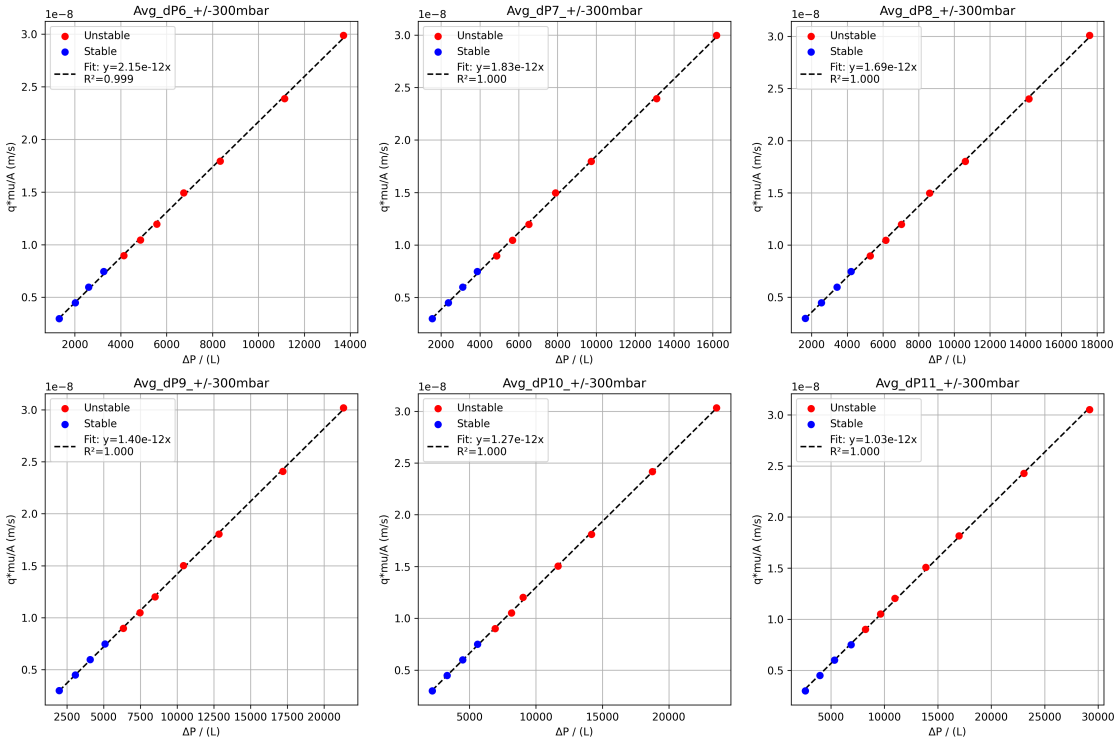

Figure D.23: Segment_fit_bp2.3_bentheimer

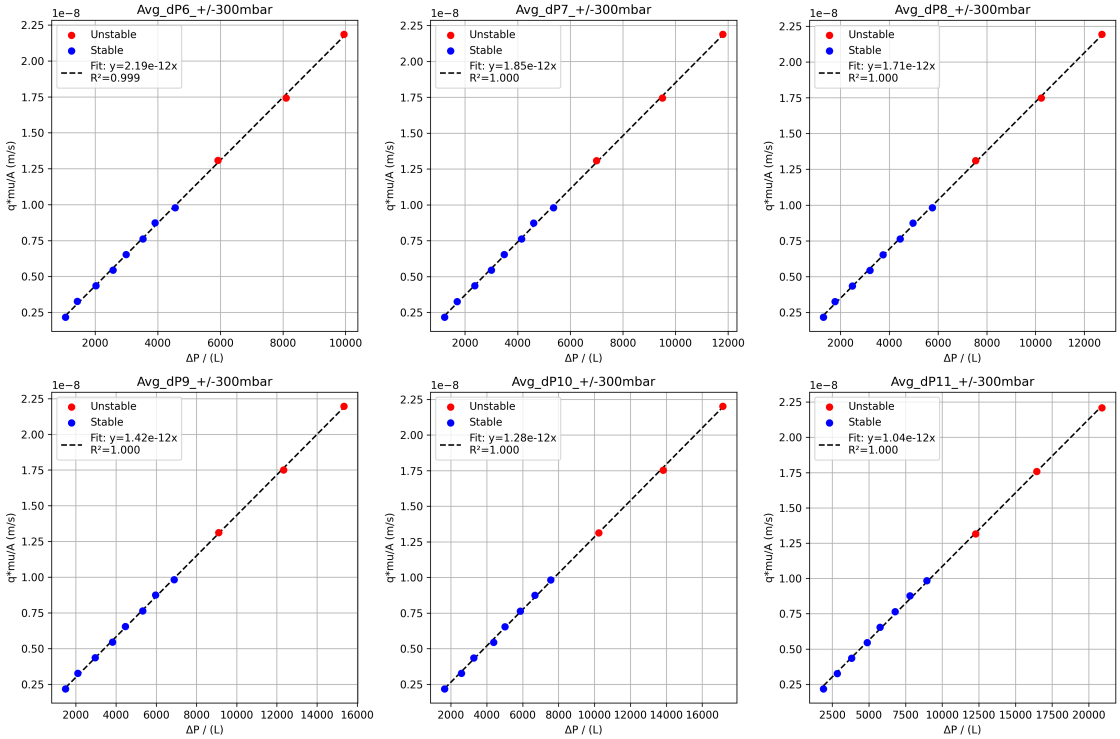

Figure D.24: Segment_fit_bp3.5_bentheimer

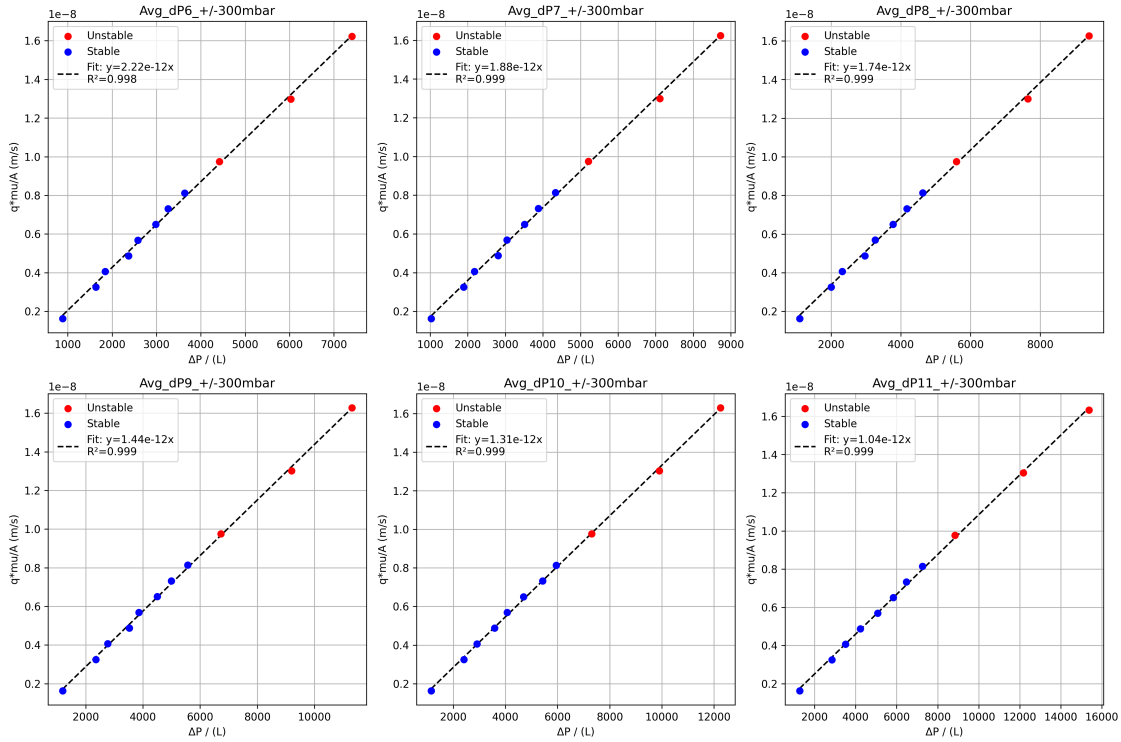

Figure D.25: Segment_fit_bp5.0_bentheimer

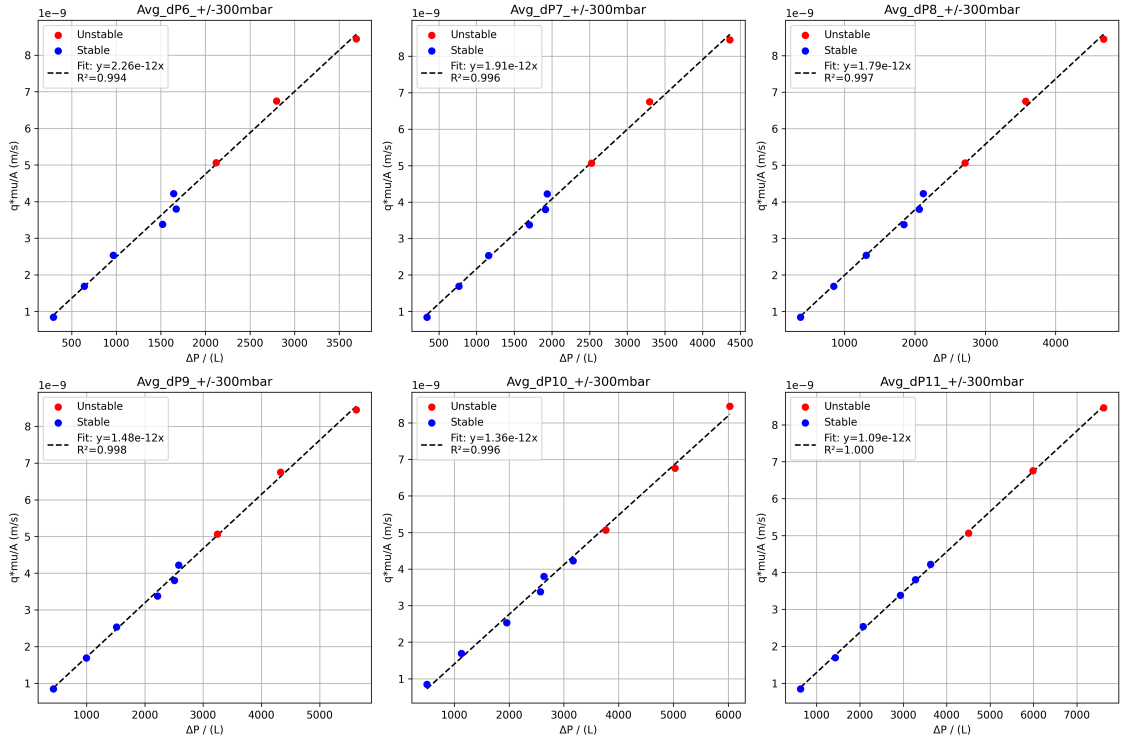

Figure D.26: Segment_fit_bp10.7_bentheimer

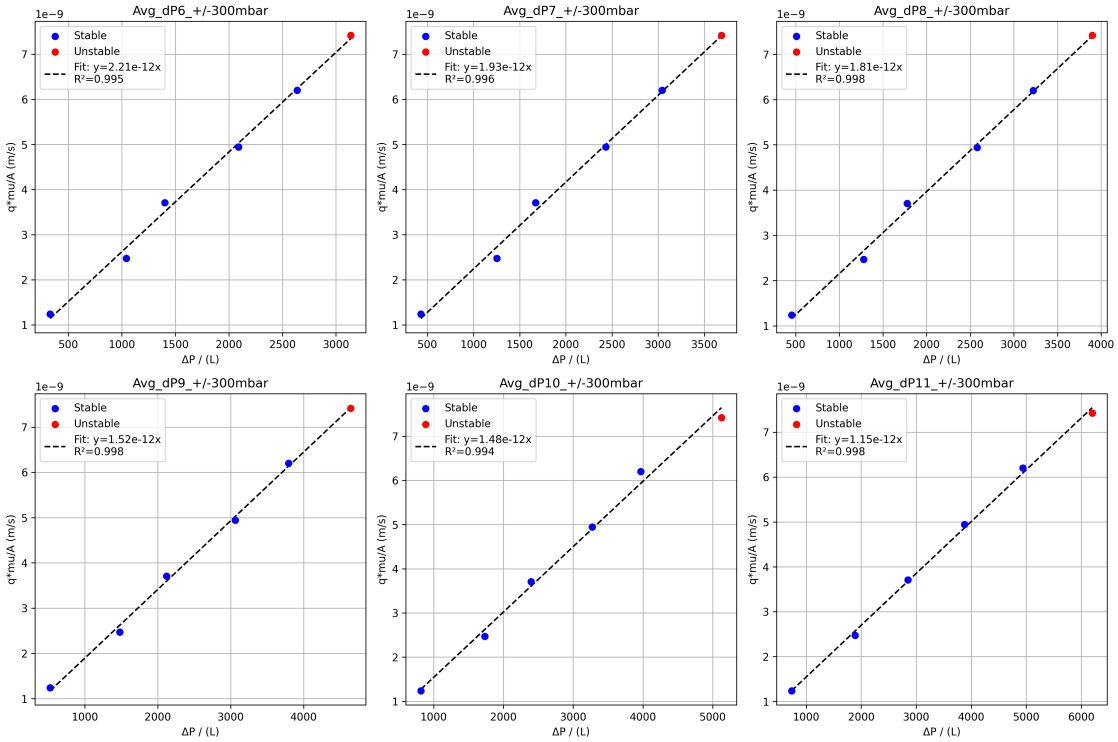

Figure D.27: Segment_fit_bp15.1_bentheimer

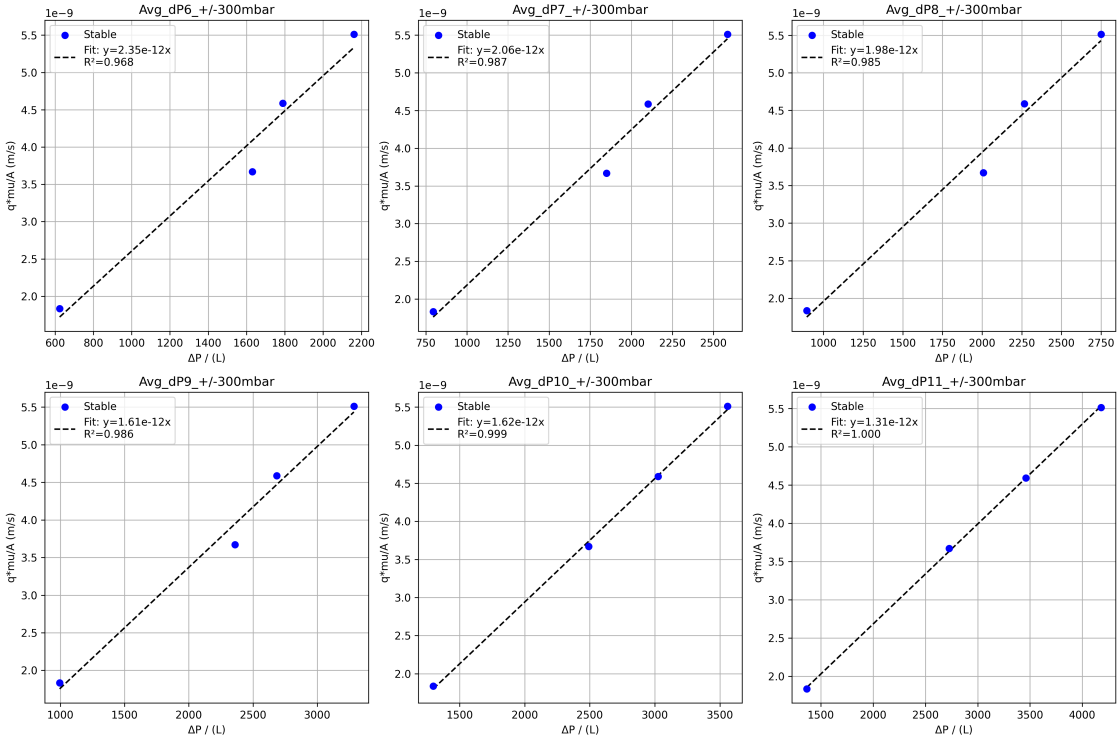

Figure D.28: Segment_fit_bp20.8_bentheimer

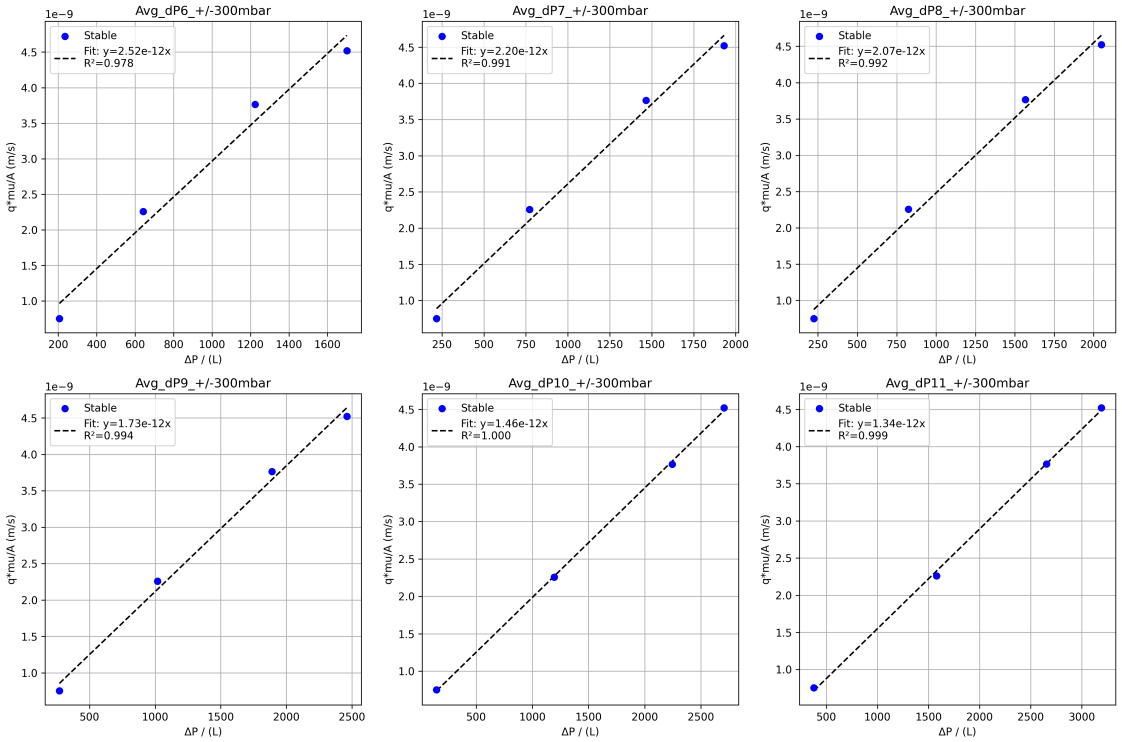

Figure D.29: Segment_fit_bp25.85_bentheimer

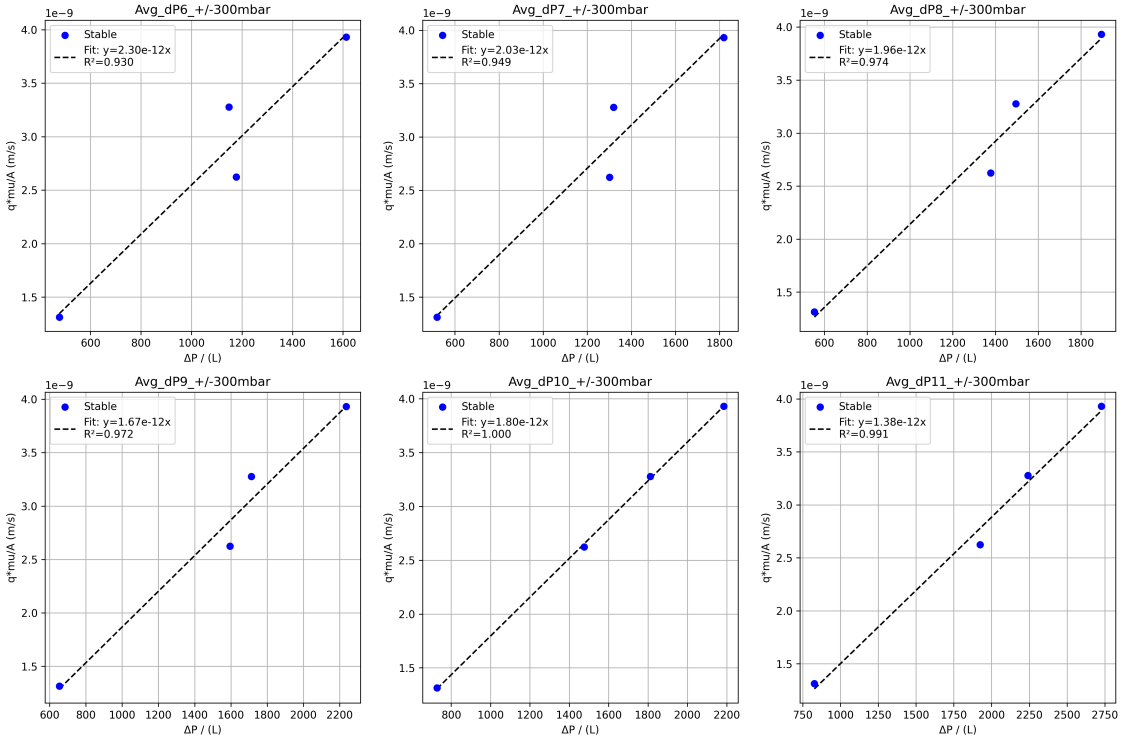

Figure D.30: Segment_fit_bp30.2_bentheimer

D.7.1. Kentucky permeability calculations (pre-experiment)

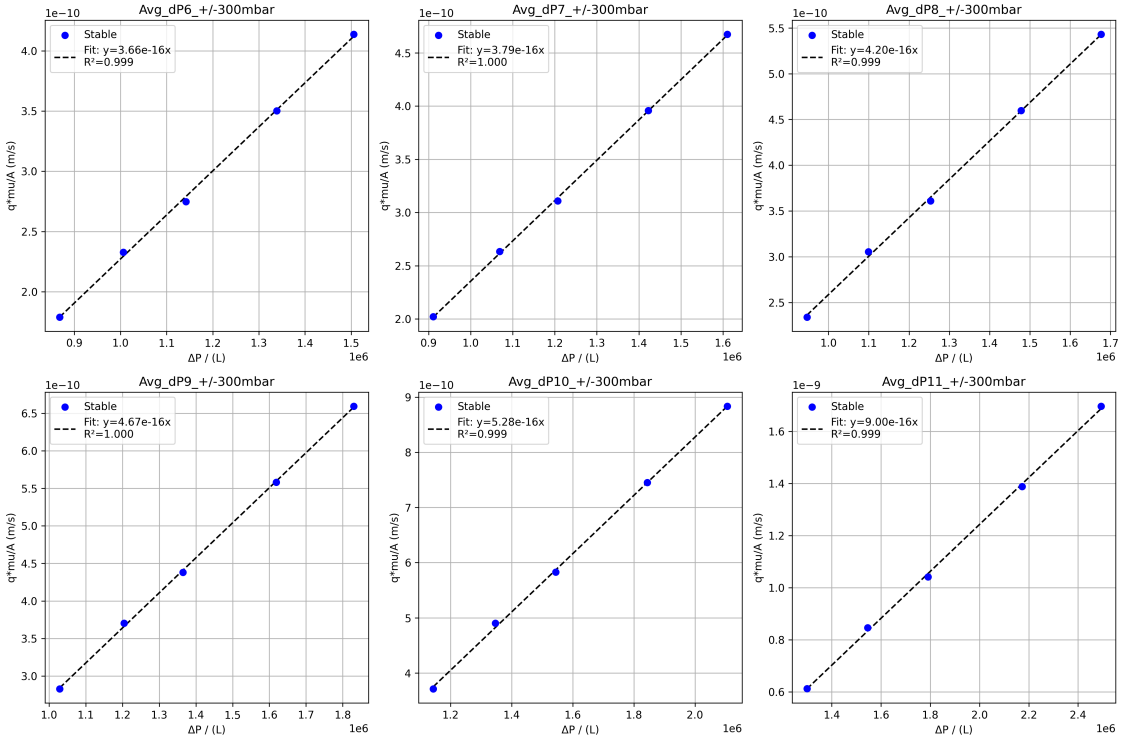

Figure D.31: Segment fit for the pre-experiment permeability test at 0.0 bar backpressure.

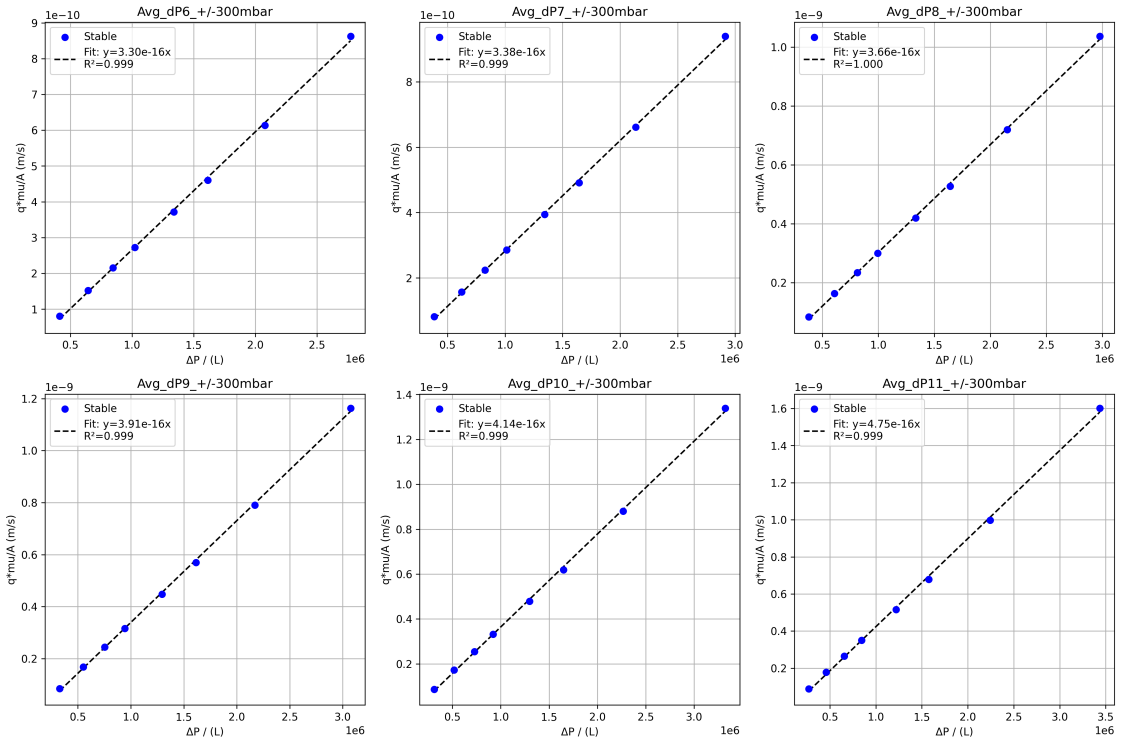

Figure D.32: Segment fit for the pre-experiment permeability test at 10.0 bar backpressure.

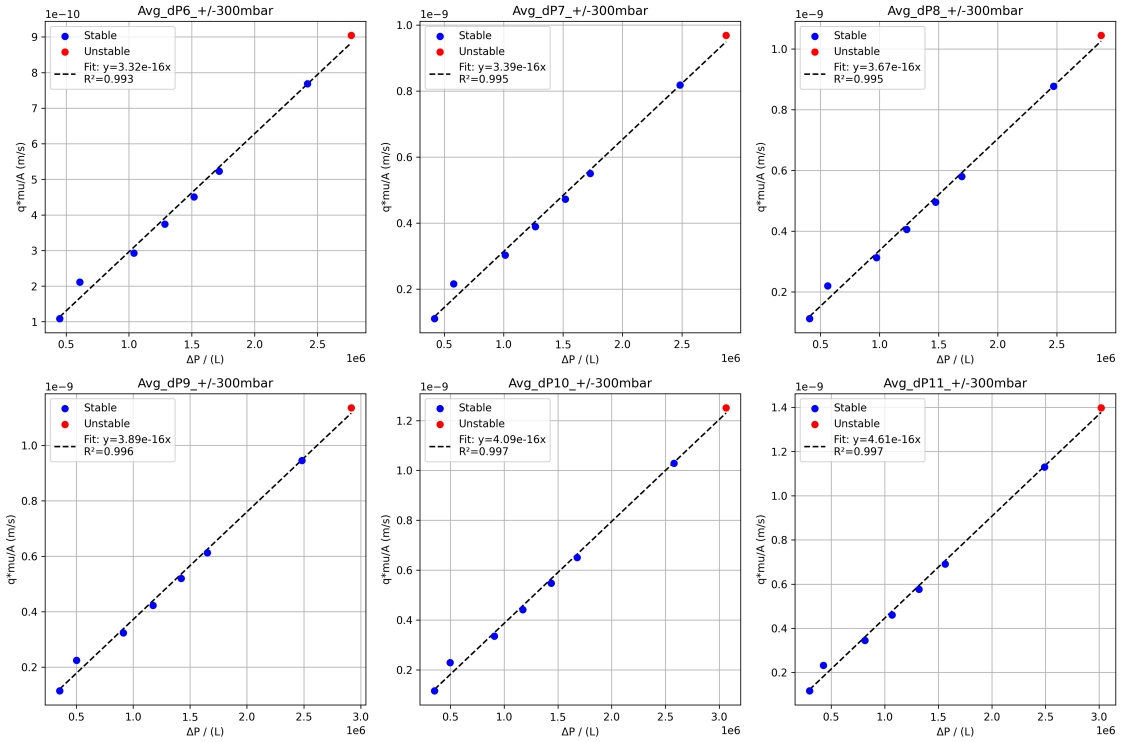

Figure D.33: Segment fit for the pre-experiment permeability test at 15.0 bar backpressure.

D.7.2. Kentucky permeability calculations (post-experiment)

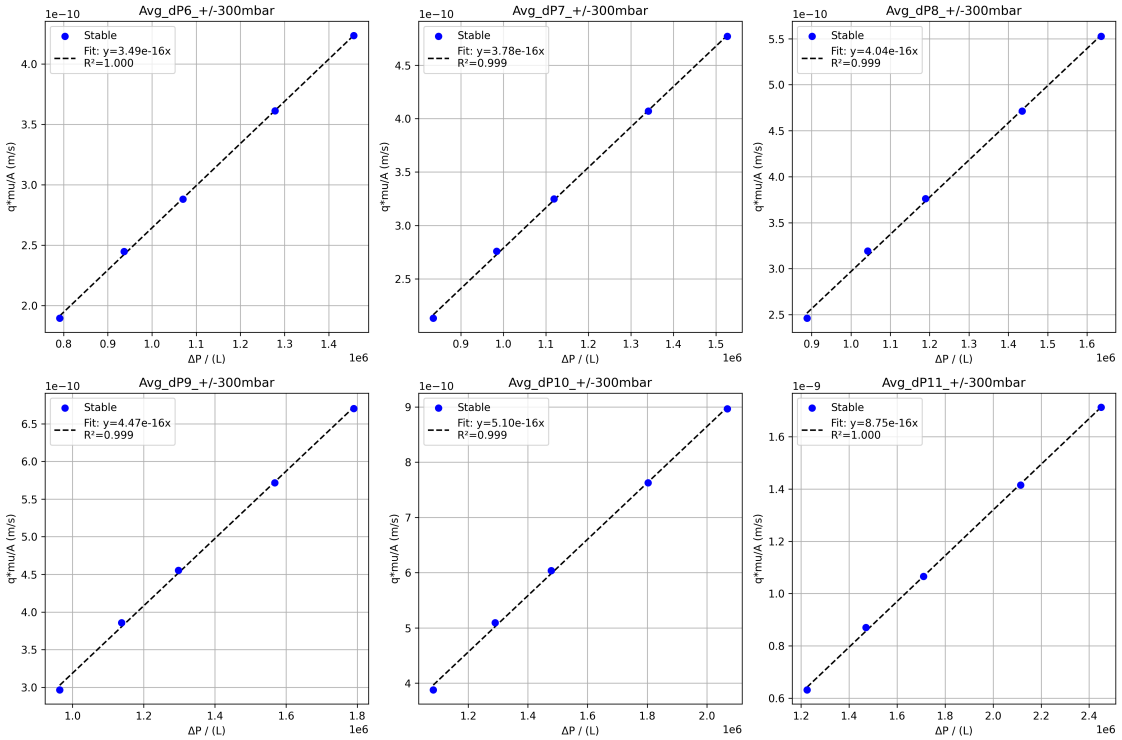

Figure D.34: Segment fit for the post-experiment permeability test at 0.0 bar backpressure.

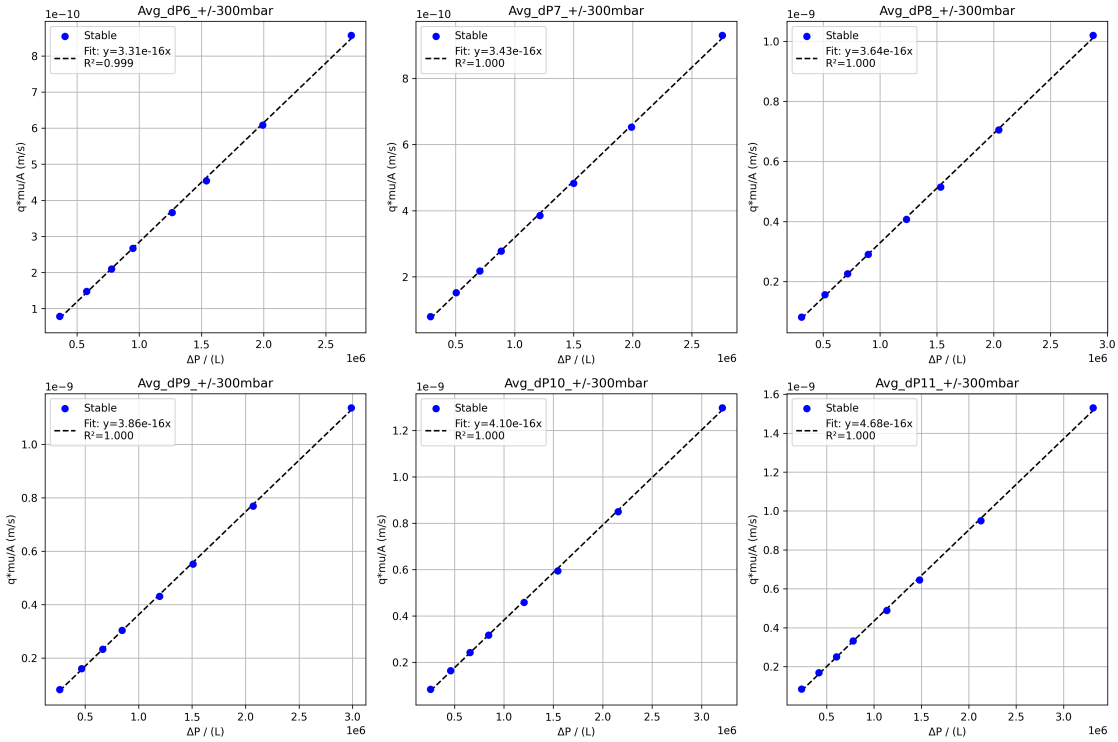

Figure D.35: Segment fit for the post-experiment permeability test at 10.0 bar backpressure.

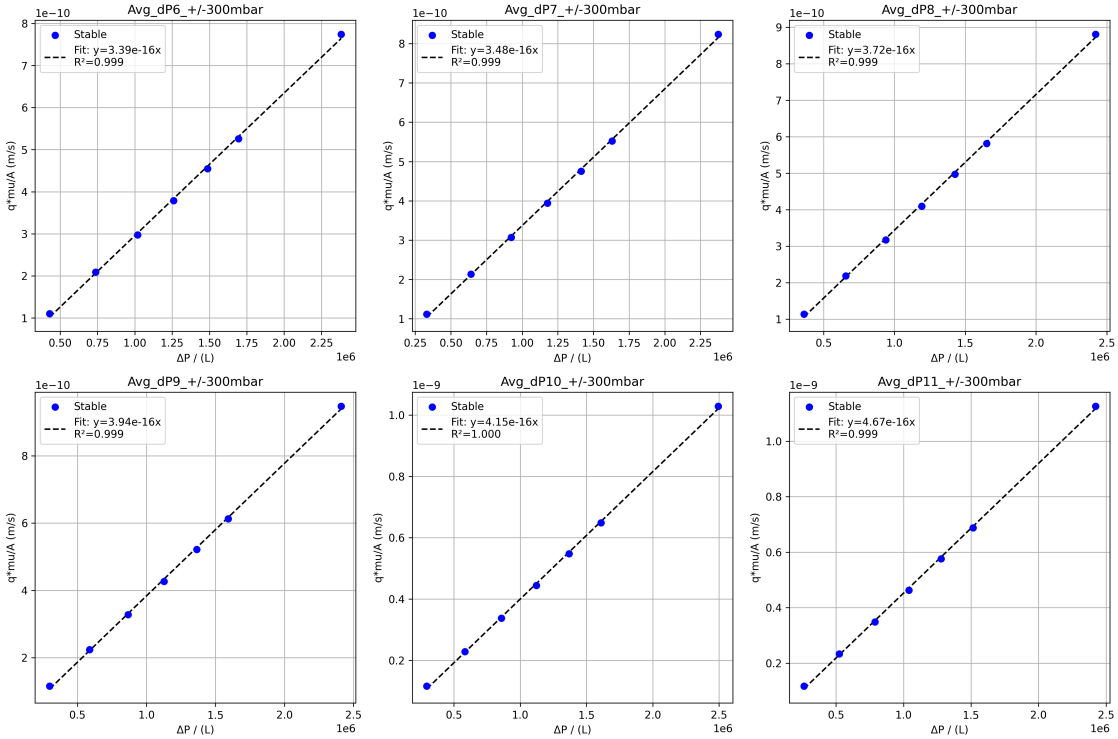

Figure D.36: Segment fit for the post-experiment permeability test at 15.0 bar backpressure.